Geological Quarterly, 2025, 69, 59
DOI: https://doi.org/10.7306/gq.1832

Geochemistry of REE-bearing minerals from the Stara Kamienica schist belt (NE Bohemian Massif, SW Poland)

Rafał MAŁEK[1, *]

[1] Polish Geological Institute – National Research Institute, Rakowiecka 4, 00-975 Warszawa, Poland; ORCID: 0000-0003-3163-2433

Małek, R., 2026. Geochemistry of REE-bearing minerals from the Stara Kamienica schist belt (NE Bohemian Massif, SW Poland). Geological Quarterly, **69**, 59; https://doi.org/10.7306/gq.1832

Associate Editor: Jacek Szczepański

Complementary micro-area mineralogical investigations using electron probe microanalysis (EPMA) allowed for the identification of several REE-bearing mineral phases, including monazite-(Ce) [(Ce,La,Nd,Th)PO_4], xenotime-(Y) [YPO_4], allanite-(Ce) [$(Ce,Ca,Y)_2(Al,Fe)_3(SiO_4)_3(OH)$], plumbogummite [$PbAl_3(PO_4)_2(OH)5 \cdot (H_2O)$], and unidentified fluorocarbonate minerals occurring in close association with cassiterite-sulphide mineralization in the Stara Kamienica schist belt (Sudetes, SW Poland). Based on whole-rock data, as well as EPMA analyses of mineral chemical compositions, the environmental origins of xenotime-(Y) and monazite-(Ce) were determined as detrital, metamorphic, and hydrothermal, reflecting the complex geological history of the study area. REE-bearing fluorocarbonates, allanite-(Ce), and plumbogummite, identified for the first time in the Stara Kamienica schist belt, require further mineralogical and geochemical investigations to clarify their origins and roles within the mineral paragenesis. The results of this study provide new insights into the genesis and evolutionary history of both the Stara Kamienica schist belt and the entire Karkonosze-Izera Massif. Exploration of the Stara Kamienica mining site has been focused so far basically just on tin mineralisation, and this study provides the first comprehensive documentation of REE-bearing phases there.

Key words: monazite, xenotime, allanite, plumbogummite, REE, tin mineralization, Stara Kamienica, Sudetes.

INTRODUCTION

Rare Earth Elements (REE), commonly categorized into light (LREE; La-Eu) and heavy (HREE; Gd-Lu, including Y) subgroups, play a crucial role in modern technological applications owing to their distinctive physicochemical properties. For this reason, they are often referred to as the "vitamins of industry" (Crow, 2011; Zhai et al., 2019; He and Yang, 2022).

The Stara Kamienica schist belt, located in the Western Sudetes of Poland and forming part of the Karkonosze-Izera Metamorphic Unit, is predominantly composed of quartz-chlorite-mica schists. Within this lithological framework, occurrences of cassiterite associated with sulphide mineralization have been identified (Michniewicz et al., 2006). Historical records indicate that tin mining activities in this area date back to the early 16th century. In the mid-20th century, two major tin ore deposits – Krobica and Gierczyn – were documented but also several prospective zones were recognized (Małek et al., 2019 and references therein). Recently, the Stara Kamienica schist belt has become an object of interest again as part of prospection and assessment work aimed at raw materials considered critical by the European Commission (CRM – critical raw material; COM, 2017; e.g., Mikulski et al., 2018; Małek et al., 2019; Foltyn et al., 2020; Zygo et al., 2023).

Whole-rock geochemical investigation of many rock samples from the Stara Kamienica schist belt indicated enrichment in some CRMs (Mikulski et al., 2018) and EPMA led to the identification of a wide range of REE-bearing minerals such as monazite-(Ce) [(Ce,La,Nd,Th)PO_4], xenotime-(Y) [YPO_4], allanite-(Ce) [$(Ce,Ca,Y)_2(Al,Fe)_3(SiO_4)_3(OH)$], plumbogummite [$PbAl_3(PO_4)_2(OH)_5(H_2O)$] and group of unidentified fluorocarbonates occurring in association with ore mineralisation.

This article characterizes the detailed mineralogy and geochemistry of (REE)-bearing minerals occurring in the Stara Kamienica schist belt. It focuses on the identification and description of mineral phases responsible for REE accumulation, their chemical composition (Appendix 1), and potential origin, in the context of the geological evolution of the Karkonosze-Izera Massif and its significance as a potential source of CRMs.

* E-mail: rafal.malek@pgi.gov.pl

Received: Received: July 31, 2025; accepted: December 13, 2025; first published online: Janauary 9, 2026

GEOLOGICAL SETTING

The Western Sudetes represent the northern exposed segment of the Saxothuringian Zone within the Bohemian Massif (Franke and Żelaźniewicz, 2000, Konopásek et al., 2019). Its southern portion comprises the Karkonosze-Izera Massif, whose core consists of a granitoid complex derived from an early Paleozoic protolith (Borkowska et al., 1980; Kröner et al., 2001). This core is encircled by metamorphosed sedimentary and volcanic sequences (Kryza et al., 1995, 2007; Winchester et al., 1995, 2003; Žáčková et al., 2012). The geological evolution of the region commenced with the subduction of the Saxothuringian Ocean, a process marked by the formation of high-pressure mineral assemblages in both mafic and felsic rocks (Kryza et al., 1990; Smulikowski, 1995; Žáčková et al., 2010; Majka et al., 2016). Subsequent stages of development involved the exhumation of these high-pressure rocks, their widespread retrogression under greenschist facies conditions, and post-metamorphic folding affecting the entire complex. Around 320–312 Ma, the regional evolution culminated in the intrusion of the Karkonosze plutonic complex into the Karkonosze-Izera Massif (Machowiak and Armstrong, 2007; Kryza et al., 2014; Mikulski et al., 2020).

The Karkonosze granitoid body, extending ~70 km along an east-west axis, forms the structural core of the Karkonosze-Izera metamorphic complex. This intrusive massif acts as a geological boundary, dividing the surrounding metamorphic sequences into two distinct domains: the Izera Metamorphic Unit to the north (forming the granitoid's northern cover) and the Karkonosze Metamorphic Unit to the east and south (Smulikowski, 1972). Recent studies involving lithostratigraphic, metamorphic and structural data suggest that subduction of distal and proximal parts of the Saxothuringian passive margin took place in high pressure conditions, with their subsequent exhumation during two distinct stages of Variscan age (Jeřábek et al., 2016). The Izera Unit is composed of two principal lithological assemblages. The dominant one, in terms of surface extent, includes pre-Variscan granitoids – chiefly Izera granites, gneisses, and transitional granite-gneisses. The second group encompasses a more heterogeneous suite of schists, primarily composed of quartz, micas and chlorite, occurring in various proportions. These schists are intercalated within the granitoid-gneiss complex as five relatively narrow, east-west trending belts with the largest one named the Stara Kamienica schist belt (Fig. 1; Oberc, 1961; Michniewicz et al., 2006).

The schist belts within the Izera Metamorphic Unit are generally interpreted as products of metamorphosed supracrustal rocks (Oberc, 1961; Oberc-Dziedzic, 1975) while the origin of the associated gneiss-granitoid complex has been the subject of three primary hypotheses. The first attributes its formation to the metamorphism and subsequent transformation of infracrustal material (Borkowska et al., 1980). The second posits a progressive granitization of supracrustal rocks, resulting in a transitional lithological spectrum from schists, through gneisses and granite-gneisses, to granitoid rocks (Oberc, 1961, 1972; Oberc-Dziedzic, 1975). A third, more integrative model suggests that both processes occurred concurrently, and that subsequent homogenization blurred the distinctions between originally different crustal levels (Kozłowska-Koch, 1965; Smulikowski, 1972; Kozłowski, 1974; Żaba, 1985; Oberc-Dziedzic, 1988; Mazur and Aleksandrowski, 2001).

Based on various geological observations and structural relationships, the schist units of the Karkonosze-Izera Massif are inferred to be of Precambrian age (Michniewicz et al., 2006). Radiometric dating of the gneiss-granitoid complex using Rb-Sr, U-Pb, and Pb-Pb methods on zircons has yielded ages between 452 and 501 Myr, placing their formation within the Late Cambrian to Late Ordovician (Borkowska et al., 1980; Oliver et al., 1993; Korytowski et al., 1993; Kröner et al., 1994).

The Stara Kamienica schists are fine-grained rocks characterized by a granolepidoblastic texture and foliation. They are typically light grey to silvery grey in colour, commonly with a subtle greenish hue, and show prominent foliation and compositional lamination. Their mineralogical composition is dominated by muscovite and quartz, which are present across all lithological variants. Chlorite and biotite occur less commonly and may either co-exist or appear separately. Locally, the presence of chloritoid- and garnet-rich zones contributes significantly to the mineralogical diversity of these rocks. In addition to the main rock-forming minerals, a range of accessory phases has been identified, including albite, staurolite, gahnite, margarite, apatite, tourmaline, zircon, monazite, xenotime, ilmenite and others (Michniewicz et al., 2006 and references therein).

The Stara Kamienica schist belt is host to well-known cassiterite-sulphide mineralisation (i.e. Harańczyk and Skiba, 1961; Kowalski et al., 1978; Wiszniewska, 1984; Bobiński, 1991; Michniewicz at al., 2006; Mikulski et al., 2018; Małek et al., 2019; Małek and Mikulski, 2024). Its origin remains a subject of ongoing debate and is possibly connected with the occurrence of REE-bearing minerals. Nowadays, there are four distinct genetic models, each supported by a separate body of evidence. The first model advocates a syngenetic, sedimentary origin for the cassiterite-sulphide mineralization, which was subsequently modified by metamorphic processes (e.g., Jaskólski, 1960, 1963; Szałamacha, 1967, 1976). A second hypothesis attributes the mineralization to pre-metamorphic, hydrothermal activity associated with the early igneous evolution of the Izera gneiss complex, thus predating the Variscan orogeny (e.g., Harańczyk and Skiba, 1961; Siemiątkowski, 1986, 1988, 1989; Michniewicz, 1988; Bobiński, 1991; Cook and Dudek, 1994; Michniewicz et al., 2006). A third view supports a post-metamorphic, hydrothermal genesis, temporally and spatially linked to the emplacement of the Variscan Karkonosze granitoid intrusion (e.g., Jaskólski and Mochnacka, 1959; Kozłowski, 1974; Kowalski et al., 1978; Karwowski and Włodyka, 1981; Wiszniewska, 1983, 1984; Speczik and Wiszniewska, 1984; Berendsen et al., 1987; Piestrzyński et al., 1992; Kucha and Mochnacka, 1998). Finally, a fourth, more integrative model has been proposed by Mikulski et al. (2007), based on studies of arsenic mineralization in Czarnów, located in the eastern margin of the Karkonosze granite and composed of lithologically comparable schists hosting cassiterite-sulphide assemblages. This interpretation suggests a complex metasomatic-hydrothermal genesis, involving multiple intrusive and metamorphic stages of both pre-Variscan and Variscan age.

SAMPLES AND METHODS

The material came from a range of sources within the Stara Kamienica schist belt, including archival borehole cores, the historical St. Johannes and St. Leopold mine workings in Krobica, a mica schist quarry in Orłowice, and post-mining dumps in Gierczyn (Fig. 1; Mikulski et al., 2018). The sample selection was dictated by the presence of Sn enrichment, as the aim of the research was focused on ore mineralization. Back-scattered electron imaging (BSEI) and compositional analyses were conducted on carbon-coated thin-sections via electron probe

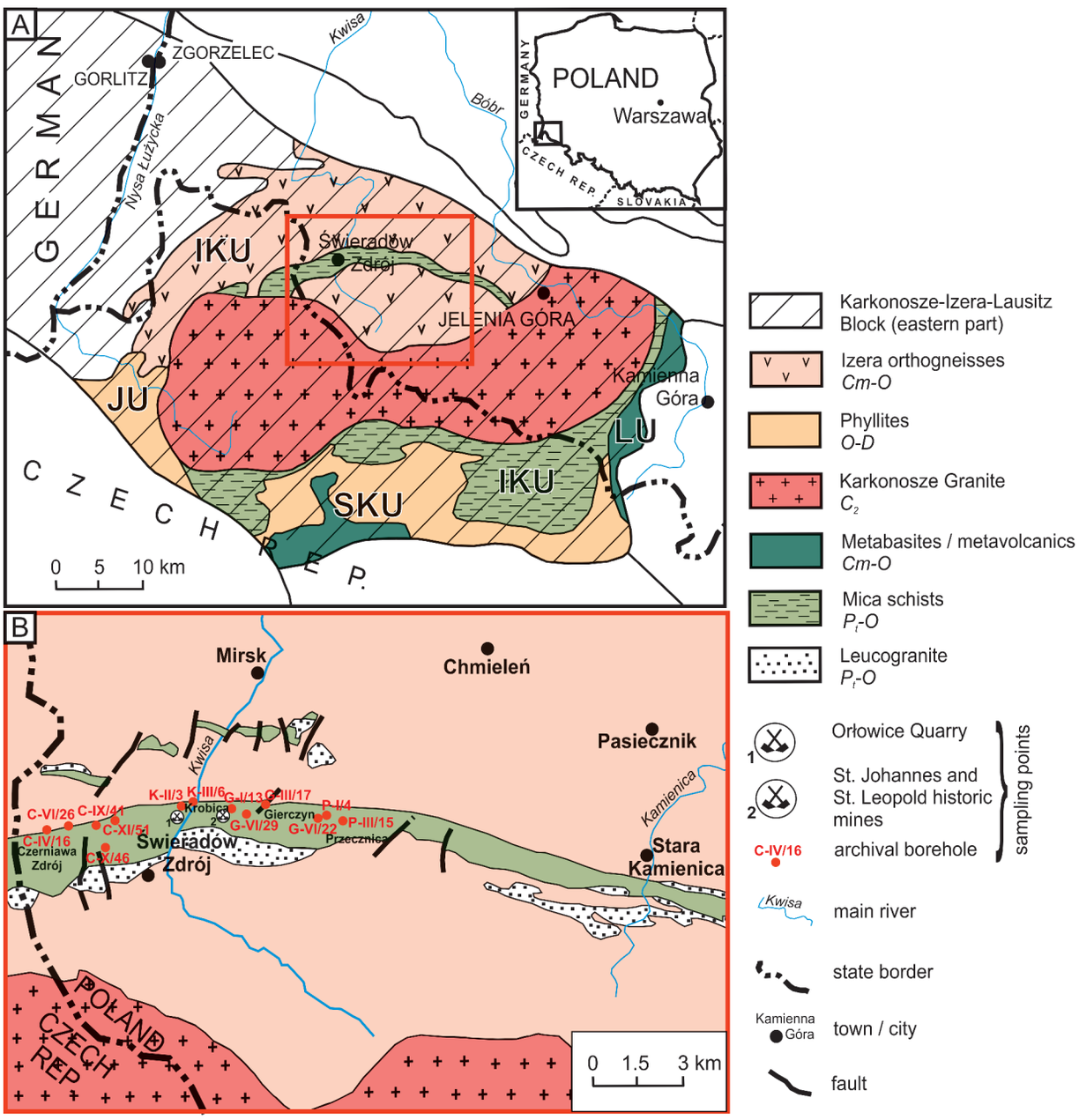

Fig. 1A – location of the Stara Kamienica schist belt hosting stratiform cassiterite-sulphide mineralisation (NE Bohemian Massif, SW Poland) with sampling points marked (B)

IKU – Izera-Kowary Unit, SKU – South Karkonosze Unit, LU – Leszczyniec Unit, JU – Ještěd Unit (modified after Michniewicz et al., 2006 and Ilnicki, 2010)

microanalysis using a *Cameca SX-100* housed in the Micro-area Analyses Laboratory at the Polish Geological Institute – National Research Institute in Warsaw, Poland. Analytical conditions included an accelerating voltage of 15 kV, beam currents of 40 nA, a focused electron beam with a diameter of <1 mm, a peak counting time of 20 seconds, and a background counting time of 10 seconds. Additional analytical conditions are given in Appendix 2.

Whole-rock chemical analyses were conducted at the Chemical Laboratory of the Polish Geological Institute – National Research Institute in Warsaw. The concentrations of REEs (Sc, Y, La, Ce, Pr, Nd, Eu, Sm, Gd, Tb, Dy, Ho, Er, Tm,

Yb, and Lu) were determined following sample decomposition using a comprehensive acid mixture of HCl, HNO_3, HF, and $HClO_4$. Measurements were carried out using a Perkin Elmer ICP-MS Elan DRC II mass spectrometer (Perkin Elmer SCIEX Instruments, Waltham, MA, USA) employing inductively coupled plasma mass spectrometry (ICP-MS).

RESULTS

ALLANITE-(Ce)

Allanite-(Ce) has been analysed in samples from archival cores drilled in different parts of the Stara Kamienica schist belt: the westernmost part (the Czerniawa-Zdrój area – C-X/46 borehole); the middle part (the Krobica area – K-II/3 borehole) and the middle to eastern part (Gierczyn – the G-I/13 and G-III/17 boreholes; Fig. 1). The samples analysed were lithologically muscovite-biotite-chlorite-quartz schist with variable proportions of the component minerals. Some contained accessory garnets (almandine). Allanite-(Ce) occurs sporadically in the samples investigated, being typically found as hypautomorphic to xenomorphic, strongly fractured grains with rounded edges, up to 100 μm across, most frequently enclosed within chlorite aggregates. Occasionally, larger grains reaching 200 μm were observed (Fig. 2). Allanite-(Ce) also tends to form disseminated impregnations within mica-rich laminae of the schists and, in rare cases, intergrowths with ore minerals, most notably pyrrhotite, cassiterite and ilmenite. Basic statistical parameters of REE concentrations in allanite-(Ce) are provided in Table 1, while the complete analytical dataset is available in Appendix 1A. The highest mean content of total REE+Y (oxides) are shown by allanite-(Ce) from the middle and middle-to-eastern parts of the Stara Kamienica schist belt – 21.47 wt.% (Gierczyn) and 20.15 wt.% (Krobica), being slightly lower in the westernmost part (Czerniawa-Zdrój) with 14.78 wt.% (Table 2).

Plotting the data obtained on an epidote group mineral classification diagram (Fig. 3; after Petrik et al., 1995) shows variable compositions of the minerals studied from the Stara Kamienica schist belt. Allanite is a member of REE-rich epidote-group minerals and is a common accessory phase in igneous, metamorphic, metasomatic and sedimentary rocks. The epidote-group structural formula is $A_2M_3Si_3O_{12}(OH)$, in which A = Ca, Sr, Pb^{2+}, Mn^{2+}, Th, REE^{3+}, and U, and M = Al, Fe^{3+}, Fe^{2+}, Mn^{3+}, Mn^{2+}, Mg, Cr^{3+}, and V^{3+} (Deer et al., 1986). REE are present in most epidote group minerals, but in allanite the REE are essential structural constituents. In the minerals analysed from the Stara Kamienica schists most of the Wavelenght-dispersive X-ray spectroscopy (WDS) spots (27 out of 40) are characterized by REE+Th >0.5 atoms per formula unit which can be considered as allanites (Table 2 and Appendix 1B; Gieré and Sorensen,

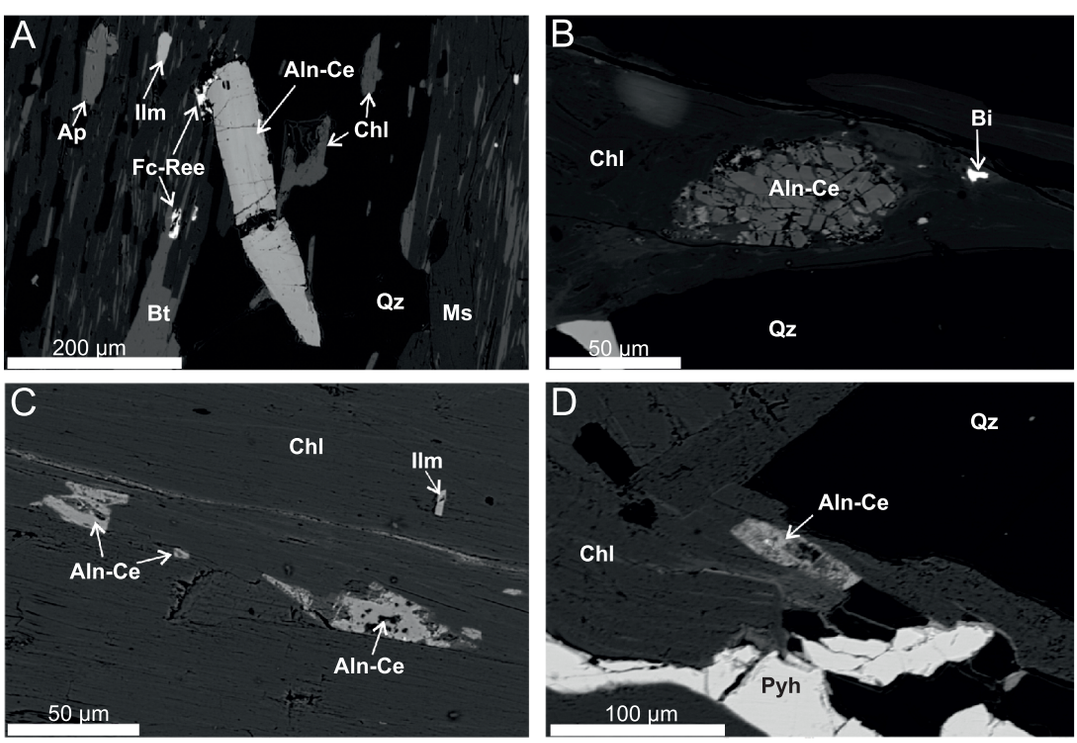

Fig. 2A – hypautomorphic allanite-(Ce) (Aln-Ce) grains with overgrown REE-bearing fluorocarbonates (Fc-Ree) within a muscovite (Ms)-chlorite (Chl)-biotite (Bt)-quartz (Qz) schist, with accessory apatite (Ap) and ilmenite (Ilm); Krobica K-II/3 borehole, BSEI; B – isolated, fractured allanite-(Ce) grain hosted within a chlorite lamina, containing inclusions of native bismuth (Bi); Czerniawa C-X/46 borehole, BSEI; C and D – xenomorphic allanite-(Ce) grains occurring within a chlorite lamina, in close association with pyrrhotite (Pyh) and ilmenite (Ilm); Gierczyn G-I/13 borehole, BSEI

Mineral abbreviations after Warr (2021)

Table 1

Statistics of REE contents in allanite-(Ce) from the Stara Kamienica schists (wt.%, n – statistical group)

Allanite-(Ce) (n = 40)	La_2O_3	Ce_2O_3	Pr_2O_3	Nd_2O_3	Sm_2O_3	Gd_2O_3	Dy_2O_3	SrO	Y_2O_3
Minimum	2.50	4.46	0.42	1.41	0.17	<0.16	<0.9	0.04	<0.09
Maximum	6.34	12.46	1.28	5.03	1.00	1.60	0.23	0.42	1.25
Arithmetic mean	4.23	8.60	0.93	3.44	0.52	0.95	0.06	0.19	0.53
Median	4.49	9.16	0.94	3.50	0.53	1.02	0.04	0.18	0.45
Standard deviation	0.90	1.75	0.19	0.81	0.17	0.43	0.07	0.09	0.29

2004). Some of the REE-rich epidote group minerals studied have total REE+Th 0.5 apfu because of an elevated content of substitutions such as Ca^{2+}, Mn^{2+}, Fe^{3+}, Fe^{2+} or Al (Table 2 and Appendix 1B).

MONAZITE-(Ce)

Monazite-(Ce) has been analysed in only two samples, one from archival borehole core in the Gierczyn area (G-VI/22) and one from the St. Leopold abandoned mine, both situated in the middle part of the Stara Kamienica schist belt. The samples analysed were lithologically muscovite-biotite-chlorite-quartz schist with different proportions of these minerals. Monazite--(Ce) is notably less abundant in the samples analysed samples compared to allanite-(Ce) and REE-bearing fluorocarbonates. It typically occurs as automorphic or hypautomorphic grains up to 100 m in diameter, commonly hosted within mica-rich laminae. In some cases, larger xenomorphic grains exceeding 100 m were observed (Fig. 4). Occasionally, monazite-(Ce) appears as inclusions within garnet or intergrown with ilmenite. Backscattered electron imaging reveals a generally homogeneous internal structure of the monazite-(Ce) grains (Fig. 5D). Basic statistical parameters of REE concentrations in the analysed monazite-(Ce) compositions are summarized in Table 3, while detailed analytical results are provided in Appendix 1C. A notable compositional difference is observed between automorphic/hypautomorphic and xenomorphic grains, primarily in their thorium contents: automorphic and hypautomorphic grains contain ~7–16 wt.% ThO_2, whereas xenomorphic grains typically contain <5 wt.% ThO_2. Monazite-(Ce) chemistry, depicting in Table 4 (Appendix 1D) and plots on Figure 5, shows significant differences in its chemical composition when comparing both areas sampled. The ones from the St. Leopold abandoned mine contain slightly higher REE+Y with simultaneous lower amounts of Th and U compared to the G-VI/22 borehole samples. In addition, higher amounts of REE+Y correlates with higher amounts of Si+Ca in monazite-(Ce) from the St. Leopold mine. Figure 5D shows cheralite $[Ca(Th,U)(Y,REE)_{-2}]$ and huttonite $[Si(Th,U)REE_{-1}P_{-1}]$ substitution in monazite-(Ce) indicating that most of the monazite-(Ce) grains studied from the St. Leopold mine have strong cheralite replacement involving $Th^{4+} + Ca^{2+}$ for $2REE^{3+}$ (Harlov et al., 2008). All results from the Gierczyn area borehole and three monazite-(Ce) grains from the St. Leopold mine in Krobica are situated within the monazite chemical composition range.

XENOTIME-(Y)

Xenotime-(Y) was identified in samples from the central part of the Stara Kamienica schist belt, in the Krobica area (K-II/3 borehole). The samples analysed were lithologically muscovite-chlorite-biotite schists with cassiterite – sulphide mineralization. Xenotime-(Y) occurs sporadically as xenomorphic grains, commonly intergrown with other REE-bearing minerals and native bismuth. Backscattered electron imaging frequently reveals zoned and irregular patches of internal structures within the xenotime-(Y) grains (Fig. 6). The full composition of the xenotime-(Y) is provided in Appendix 1E. Among the trace elements, notable enrichments were observed in middle (MREE: Sm, Eu, Gd) and heavy rare earth elements (HREE: Tb - Lu; Table 5). Elevated contents of Fe (FeO average: 1.23 wt.%; Fe_2O_3 average: 1.37 wt.%) and UO_2 (1.00 wt.%) were also detected as common trace elements in the xenotime-(Y). In grains showing zoned internal structure, compositional variations were recorded between the cores and rims: cores are characterized by higher yttrium and lower REE contents, whereas the outer rims show reduced Y concentrations accompanied by enrichments in certain REEs, particularly Gd, Tb and Dy (Figs. 6A, 7; Tables 6, 7 and Appendix 1F). Mineral chemistry plots of xenotime-(Y) grains analysed (Fig. 8) shows variety in their composition. Some grains are characterized by a higher Y content at the expense of REE, and total U+Th is relatively low. The chemical composition of the xenotime-(Y) is generally constant, but there are some substitutions of coffinite $[U(SiO_4)(OH)_4]$ because of higher Si content in most grains studied (Fig. 8C) and there is no clear cheralite $[CaTh(PO_4)_2]$ substitution in the xenotime-(Y) studied due to low Ca content (Fig. 8D).

REE FLUOROCARBONATES

REE fluorocarbonates are relatively common in the samples analysed from the Stara Kamienica schist belt. They have been identified in several samples from archival boreholes in the Gierczyn area (G-III/17, G-I/13), Krobica (K-II/3) and the westernmost location, in the Czerniawa-Zdrój area (C-X/46).

Table 2

Mean EPMA analyses of allanite-(Ce) from the Stara Kamienica schist belt archival boreholes

Sample point	C-X/46	G-I/13	K-II/3	G-III/17
	12	12	8	8
SiO_2	33.32	31.97	32.33	29.92
TiO_2	0.29	0.20	0.25	0.16
Al_2O_3	21.25	19.80	20.65	18.49
Fe_2O_3	12.05	12.09	11.08	15.74
FeO	10.85	10.88	9.97	14.16
MgO	0.12	0.25	0.04	0.07
CaO	15.75	11.57	12.87	10.92
La_2O_3	3.16	4.66	4.66	4.76
Ce_2O_3	6.62	9.68	9.14	9.42
Pr_2O_3	0.73	1.04	0.99	1.00
Nd_2O_3	2.52	3.94	3.62	3.87
Sm_2O_3	0.37	0.60	0.52	0.64
Gd_2O_3	0.90	1.14	0.34	1.35
ThO_2	0.02	0.15	0.06	0.34
Y_2O_3	0.48	0.40	0.89	0.47
MnO	0.12	0.39	0.25	0.20
SrO	0.21	0.24	0.11	0.17
Total	97.93	98.12	97.79	97.51
Σ REE	14.78	21.45	20.15	21.51
Si	3.490	3.479	3.501	3.274
Ti	0.023	0.016	0.021	0.013
Al	1.967	1.904	1.977	1.789
Fe^{2+}	0.712	0.742	0.677	0.964
Fe^{3+}	0.472	0.473	0.434	0.616
Mg	0.009	0.020	0.003	0.006
Ca	0.883	0.674	0.746	0.641
La	0.092	0.140	0.139	0.144
Ce	0.191	0.289	0.272	0.284
Pr	0.021	0.031	0.029	0.030
Nd	0.071	0.115	0.105	0.114
Sm	0.010	0.017	0.014	0.018
Gd	0.023	0.031	0.009	0.037
Th	0.000	0.004	0.001	0.008
Y	0.020	0.017	0.038	0.020
Mn	0.005	0.018	0.011	0.009
Sr	0.006	0.007	0.003	0.005
Total	8.0	7.98	7.99	7.97
REE+Th	0.408	0.627	0.571	0.635

Atoms per formula unit (apfu) calculated to 12.5 oxygen and 8 cations

The samples analysed were lithologically muscovite-biotite-chlorite-quartz schist with different proportions of these minerals. REE-bearing fluorocarbonates typically occur as xenomorphic grains, most frequently intergrown with apatite and allanite-(Ce), ilmenite and rutile. Additionally, small isolated grains, up to ~50 μm in diameter, are dispersed within the schist matrix (Fig. 9). A total of 32 spot WDS analyses were conducted to determine their chemical composition. The mineral names of the REE-fluorocarbonate group are defined by their most common REE and by the relation of calcium to the REE with bastnäsite and synchisite as endmembers (Meng et al., 2002). The absence of carbon detection in the analytical setup (due to carbon coating of the thin sections) prevented precise identification of specific mineral phases, but plotting Ca and REE data on classification diagrams point to bastnäsite-(Ce) [$Ce(CO_3)F$] (Figs. 10 and 11). Based on chemical data published by Meng et al. (2002) the ratio of Ca and most common REE <0.5 corresponds to bastnäsite. The highest content among REE in the fluorocarbonates studied from the Stara Kamienica schists is Ce (Ce_2O_3 in a range between 21.29–30.83 wt.%). Elevated Ca contents in several fluorocarbonates (CaO up to 10.97 wt.%) suggest comparison with parisite-(Ce) [$Ca(Ce,La)_2(CO_3)_3F_2$] (e.g., Manfredi et al., 2013; Fig. 12) but this is still unconfirmed. Basic statistical parameters of REE concentrations measured in these minerals are summarized in Table 8, with the complete analytical dataset provided in Appendix 1G. Average total REE+Y oxide contents in the fluorocarbonate grains studied range from 46.98 to 72.54 wt.%. The graphs on Figure 12 shows the variation of the main REE elements (Ce and La) in relation to Ca and F from the samples of different Stara Kamienica schist belt regions. The data plotted does not indicate clear dependencies; only the highest content in fluorocarbonates from the Krobica area can be noted.

PLUMBOGUMMITE

Plumbogummite containing REE admixtures was identified in a sample collected from the historic St. Leopold adit that was a chlorite-quartz schist with accessory garnet. The mineral occurs as small grains partially filling a fracture within garnet-almandine (Fig. 13). Two spot analyses of the plumbogummite were made, and the results are given in Appendix 1H. The measured concentrations of major elements were as follows: PbO – 32.36 and 29.39 wt.%, Al_2O_3 – 26.00 and 25.83 wt.%, and P_2O_5 – 22.02 and 19.99 wt.%. Among trace elements, notable concentrations of REEs were recorded, including La_2O_3 (1.02–1.67 wt.%), Ce_2O_3 (1.85–3.01 wt.%), Pr_2O_3 (<0.22–0.26 wt.%), Nd_2O_3 (0.72–1.16 wt.%), Dy_2O_3 (<0.11–0.12 wt.%), as well as Y_2O_3 (0.13–0.14 wt.%). The results obtained were plotted on a ternary classification plot (Fig. 14) for the most common members of the plumbogummite group and compared to minerals identified by Kruszewski and Dec (2018) from Podłazie Hill (Holy Cross Mountains, Poland). Because of the high PbO content, the results clearly point to plumbogummite.

WHOLE-ROCK ANALYSIS

Among the rare earth elements analysed using the ICP-MS method, the highest concentrations were recorded for Ce (1.90–114.2 ppm, n = 64, Appendix 1I), Y (1.40–95.60 ppm, n = 64), La (1.20–56.80 ppm, n = 64), Sc (3.80–50.0 ppm, n = 64),

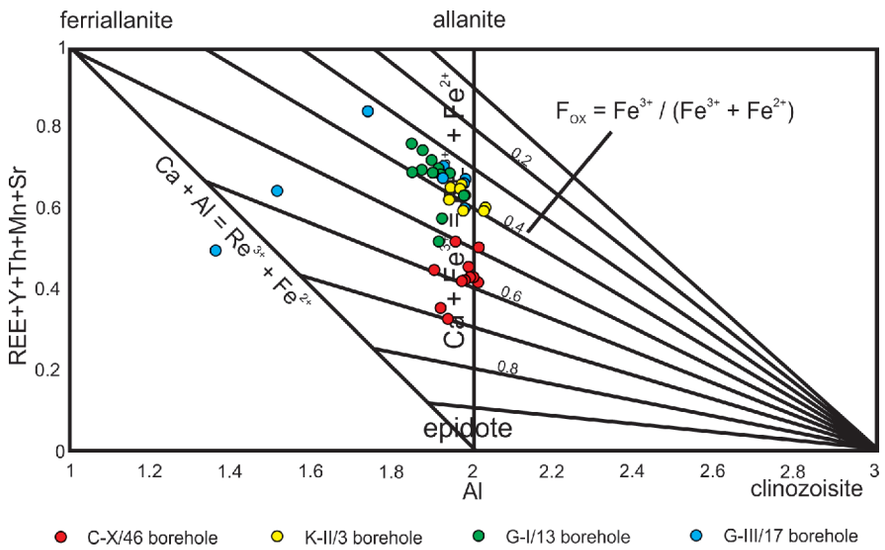

Fig. 3. Compositional plot of total REE+Y+Th+Mn+Sr *versus* Al contoured with isolines of the ratio $F_{OX} = Fe^{3+} / (Fe^{3+} + Fe^{2+})$ illustrating substitution: allanite-epidote, ferriallanite-epidote and ferriallanite-allanite (after Petrik et al., 1995)

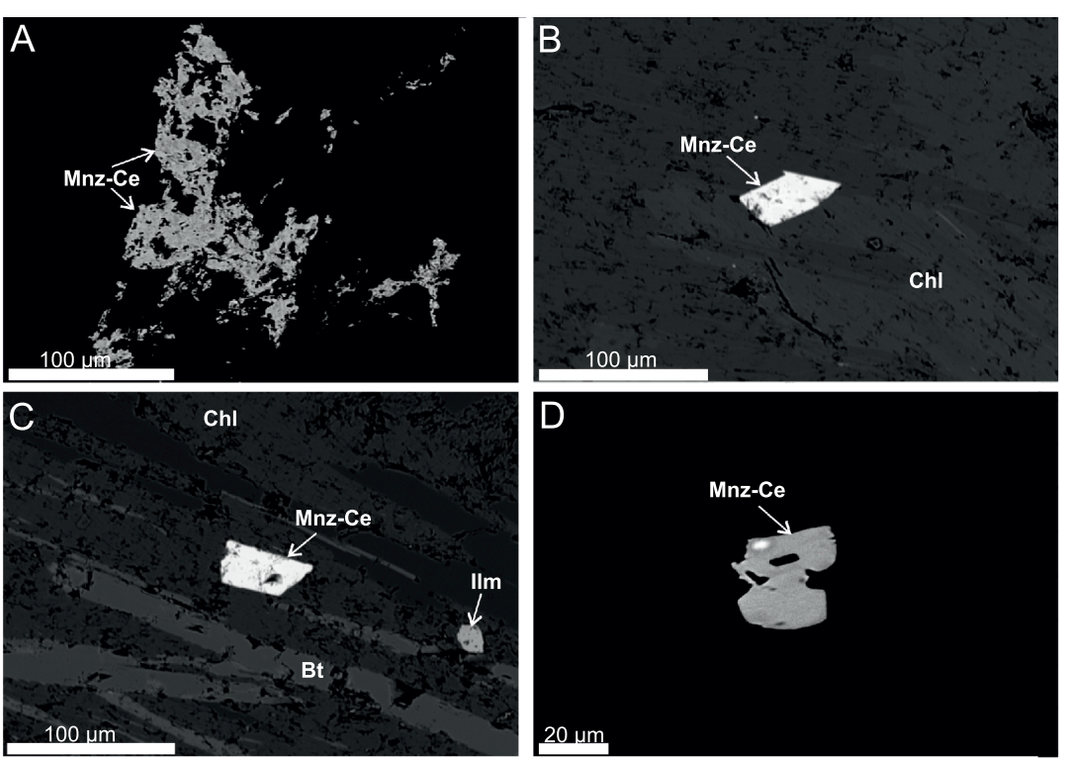

Fig. 4A – xenomorphic monazite-(Ce) (Mnz-Ce) grain; St. Leopold adit in Krobica BSEI; B and C – isolated, automorphic / hypautomorphic monazite-(Ce) grains hosted within a chlorite (Chl) – biotite (Bt) lamina, containing accessory ilmenite (Ilm); Gierczyn G-VI/22 borehole, BSEI; D – xenomorphic monazite-(Ce); Krobica K-II/3 borehole, BSEI

Nd (0.80–49.70 ppm, n = 64), Dy (0.15–19.76 ppm, n = 64), Pr (0.70–13.20, n = 64) and Er (0.09–10.11 ppm, n = 64), The maximum contents of other REEs are all below 10 ppm (n = 64).

The REE results were normalized to chondrite (McDonough and Sun, 1995), European shales (Bau et al., 2018) and PAAS (Post-Archean average Australian sedimentary rock; McLennan, 1989; Fig. 15). The diagrams clearly indicate an enrichment in

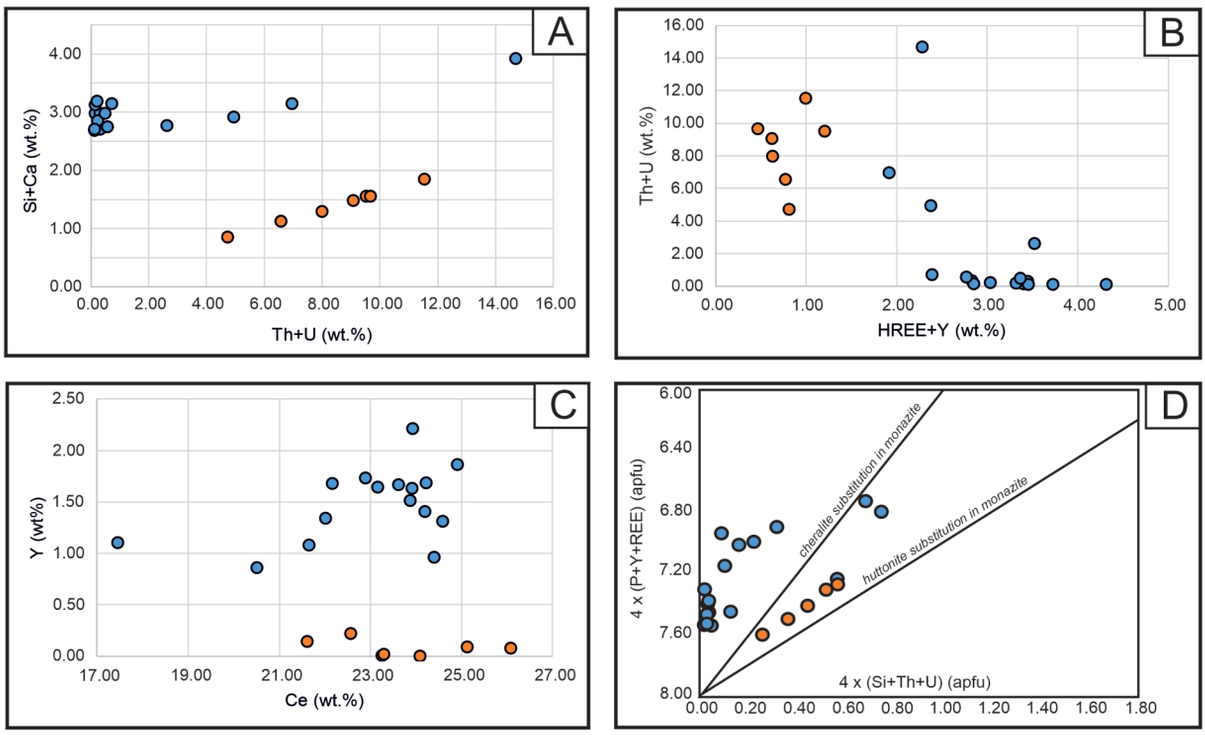

Fig. 5. Monazite-(Ce) mineral chemistry plots

A – Th+U *versus* Si+Ca; **B** – HREE+Y *versus* Th+U; **C** – Ce *versus* Y depicting the total pure xenotime-(Y) component in the monazites; **D** – (Si+Th+U) vs. (P+Y+LREE) in atoms per formula unit (apfu) for monazite-(Ce) depicting cheralite [$Ca(Th,U)(Y,REE)_{-2}$] and huttonite [$Si(Th,U)REE_{-1}P_{-1}$] substitution in monazite-(Ce) (after Harlov et al., 2008; Burda et al., 2020); Blue dots – monazite-(Ce) results from St. Leopold mine samples; orange dots – samples from the G-VI/22 borehole (Gierczyn area)

Table 3

Statistics of REE contents in monazite-(Ce) from the Stara Kamienica schists (wt.%, n – statistical group)

Monazite-(Ce) (n = 23)	La_2O_3	Ce_2O_3	Pr_2O_3	Nd_2O_3	Sm_2O_3	Gd_2O_3	Dy_2O_3	SrO	Y_2O_3
Minimum	8.59	20.44	2.10	8.26	1.42	0.53	<0.11	<0.05	<0.05
Maximum	16.31	30.56	3.13	11.76	2.35	1.62	0.80	0.17	2.81
Arithmetic mean	12.89	27.17	2.74	10.50	1.78	1.10	0.41	0.09	1.34
Median	13.09	27.67	2.77	10.57	1.74	1.14	0.50	0.10	1.66
Standard deviation	1.79	2.06	0.24	0.88	0.22	0.29	0.26	0.04	0.90

LREE (La-Sm) relative to HREE (Eu-Lu), as well as a general enrichment in REE concentrations in samples from the Stara Kamienica schist belt compared to chondrite (ranging from several times up to several hundred times). A few samples deviate from the general REE trend, likely because these samples represent boudins or quartz veins with sulphides, in which REE-bearing minerals are scarce: the samples with the lowest total REE content (Appendix 1I). The results have been divided into two graphs: that on Figure 15A includes samples that show a negative europium anomaly when normalized to chondrite, while the graph on Figure 15B includes those with a positive Eu anomaly. Additionally, most samples exhibit a slight enrichment in Y.

The vast majority of the results show depleted concentrations of rare earth elements relative to the European Shale Standard, with only a few samples showing slight enrichment. A somewhat more pronounced enrichment in REE is observed in relation to PAAS; however, most values still remain lower. In both diagrams (Fig. 15C, D), most samples display a positive europium anomaly. As with chondrite normalization, a few samples deviate from the general REE concentration trend.

INTERPRETATION AND DISCUSSION

REE-BEARING MINERALS

Detailed micro-area studies of the mineral occurrences and chemical compositions enabled the identification of REE-bearing mineral phases from the Stara Kamienica schist belt. These include allanite-(Ce) (a carrier primarily of LREE), monazite-(Ce) (mainly LREE), REE fluorocarbonates (LREE), plumbo-

Table 4

Mean EPMA analyses of monazite-(Ce) from the Stara Kamienica schists

Sample point	St. Leopold mine	G-VI/22 borehole
n =	16	7
Ce_2O_3	26.91	27.79
P_2O_5	29.83	28.43
La_2O_3	12.20	14.46
Nd_2O_3	10.56	10.37
ThO_2	2.02	9.32
Pr_2O_3	2.71	2.80
CaO	3.98	1.35
PbO_2	2.59	0.15
Sm_2O_3	1.80	1.74
Y_2O_3	1.88	0.10
Gd_2O_3	1.25	0.76
Fe_2O_3	0.83	0.51
Dy_2O_3	0.57	0.05
Eu_2O_3	0.39	0.21
UO_2	0.31	0.29
SrO	0.12	0.04
SiO_2	0.27	0.90
Al_2O_3	0.20	0.03
SO_3	0.43	0.16
K_2O	0.09	0.03
As_2O_3	0.07	0.00
Total	99.02	99.48
Ce	0.283	0.304
P	1.209	1.201
La	0.129	0.159
Nd	0.108	0.111
Th	0.018	0.085
Pr	0.019	0.020
Ca	0.082	0.029
Pb	0.025	0.002
Sm	0.018	0.018
Y	0.029	0.002
Gd	0.012	0.008
Fe^{2+}	0.018	0.012
Dy	0.005	0.000
Eu	0.004	0.002
U	0.003	0.003
Sr	0.001	0.000
Si	0.010	0.036
Al	0.007	0.001
S	0.018	0.007
K	0.001	0.000
As	0.001	0.000
Total	2.00	2.00
REE+Y	0.607	0.625

Atoms per formula unit (apfu) calculated to 4 oxygen and 2 cations

gummite (LREE/MREE), and xenotime-(Y): the only identified carrier of MREE/HREE. Analysis of the chemical composition of REE-bearing minerals [except xenotime-(Y)] from the Stara Kamienica schist belt were first performed and partly mentioned previously by Mikulski et al. (2018, 2021), Małek and Mikulski (2019, 2024), Mikulski and Małek (2019), Małek et al. (2019). In addition, allanite-(Ce), REE fluorocarbonates, and plumbogummite were identified for the first time in the Stara Kamienica range as carriers of rare earth elements.

The first chemical composition analyses of xenotime-(Y) from the Stara Kamienica schists were conducted by Bobiński et al. (2004), who identified a zoned structure in these minerals, and consequently, variations in their chemical composition resulting from the substitution of various REE elements (mostly HREE) for yttrium. The xenotime-(Y) composition data described by Bobiński et al. (2004) and later by Michniewicz et al. (2006) correspond well with the results obtained in this study; in both cases, enrichments in Dy, Gd, Er, Yb, and occasionally U were observed as well as differences in chemical composition of the internal structure zones (Fig. 6A and Table 6). Microscopic studies and in situ chemical mapping of xenotime-(Y) in various geological contexts consistently revealed well-developed chemical zoning – including oscillatory and concentric patterns – attributable to the progressive crystallization and fractionation of REE subgroups (LREE, MREE, HREE) during growth. In particular, HREE-enriched rims that contrasted with LREE-rich or Y-rich cores have been documented. In addition, several studies report that zonation may arise during metamorphic and metasomatic evolution, or in hydrothermal settings (e.g., Repina, 2010; Repina and Muftakhov, 2021). Based on the xenotime-(Y) grain shape and its internal structures and chemical composition it can be concluded that this mineral phase was formed in the schists and were then cataclased during later deformation. However, the U content *versus* U/Th ratio diagram for xenotime-(Y) formation environments (McNaughton and Rasmussen, 2018) shows that xenotime-(Y) from the Stara Kamienica schist belt (blue dots) plots within the diagenetic field (Fig. 16). Due to the low Th content in the xenotime-(Y) studied (<170 ppm, with an average of 60 ppm), the U/Th ratio ranges between 10 and 1000, whereas xenotime-(Y) of hydrothermal origin is typically characterized by lower U/Th ratios (0.1–10). Nevertheless, in detrital grains found in metasedimentary rocks – particularly those affected by complex geological overprints, such as the Stara Kamienica schist belt – the primary formation environment is commonly obscure (Rasmussen, 1996; McNaughton and Rasmussen, 2018). Originally detrital xenotime-(Y) from the sedimentary protolith of the schists may have been altered during regional metamorphism. Additionally, a coffinite substitution in xenotime-(Ce) (Fig. 8C) may also point to metamorphic alternation of primary detrital xenotime-(Ce) because of Si-U incorporation during the dissolution–reprecipitation mechanism of regional metamorphism conditions (Hetherington and Harlov, 2008; Švecová et al., 2016; Harlov, 2024). It can be concluded that xenotime-(Y) growth therefore occurred before the regional metamorphism of the rocks – it is of pre-metamorphic origin.

The chemical composition of monazite-(Ce) from the Stara Kamienica schist belt has not been studied previously. According to Michniewicz et al. (2006), monazite in this area occurs both as a detrital and metamorphic mineral. It is a common accessory phase in igneous, metamorphic, and sedimentary rocks, and its composition can serve as an empirical tool for distinguishing between crystallization environments (Liu et al., 2022). Trace element data from monazite-(Ce) samples collected in the Stara Kamienica schist belt were plotted on origin-discrimination diagrams provided by various authors (Fig. 17; Aleinikoff et al., 2012, 2023; Wu et al., 2019; Liu et al., 2022). Most of the data fall within well-defined fields corresponding to specific origins, although a few points deviate from

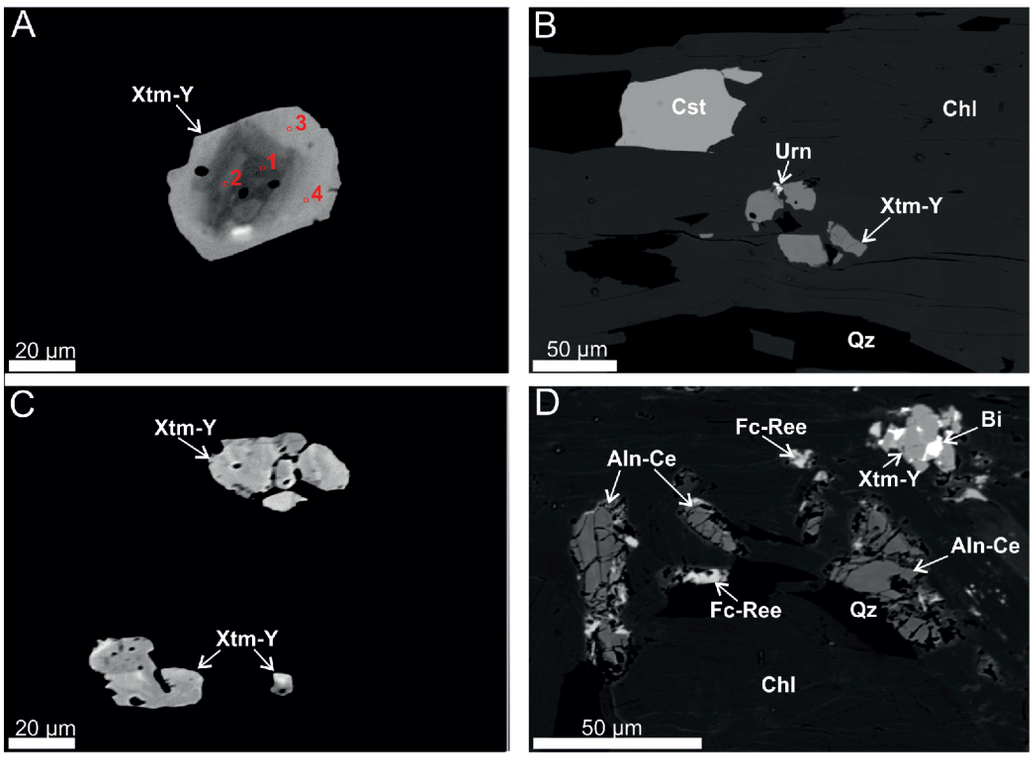

Fig. 6A – hypautomorphic xenotime-(Y) (Xtm-Y) grain with zonal internal structure, red points correspond to analytical WDS points of Table 7; Krobica K-II/3 borehole, BSEI; B – xenotime-(Y) grains with overgrown uraninite (Urn) in chlorite (Chl) lamina in the vicinity of cassiterite (Cst), Krobica K-II/3 borehole, BSEI; C – xenomorphic xenotime-(Y) grains with spotted internal structure; Gierczyn G-I/13 borehole, BSEI; D – xenotime-(Y) growth with native bismuth (Bi) in chlorite-quartz (Qz) lamina, in the vicinity of REE carrier minerals – allanite-(Ce) (Aln-Ce) and REE fluorocarbonates (Fc- Ree), Czerniawa C-X/46 borehole, BSEI

Table 5

Statistics of REE contents in xenotime-(Y) from the Stara Kamienica schists (wt.%, n – statistical group)

Xenotime-(Y) (n = 18)	Nd_2O_3	Gd_2O_3	Eu_2O_3	Sm_2O_3	Dy_2O_3	Er_2O_3	Tb_2O_3	Yb_2O_3	Ho_2O_3	Tm_2O_3	Lu_2O_3
Minimum	0.00	1.03	0.12	0.07	5.29	2.93	0.34	1.73	1.14	0.25	0.48
Maximum	0.63	6.28	0.83	1.48	9.90	4.41	1.34	3.51	1.43	0.45	0.82
Arithmetic mean	0.14	3.20	0.32	0.46	7.17	3.82	0.79	3.11	1.30	0.32	0.67
Median	0.08	2.50	0.19	0.19	7.01	3.89	0.72	3.28	1.32	0.31	0.68
Standard deviation	0.16	1.62	0.24	0.43	1.07	0.38	0.26	0.51	0.08	0.06	0.09

these general trends. In diagrams A and B (Fig. 17), most results (blue dots) indicate an igneous or metamorphic origin, with a few also falling within the hydrothermal field. Data plotted on diagrams C and D suggest a predominantly igneous origin, but also include points within the meta-igneous and metasedimentary fields. These results suggest that monazite-(Ce) grains from the Stara Kamienica schist belt are of mixed provenance. Monazite is well-known for its resistance to weathering, as indicated by its widespread occurrence as a detrital mineral in sands and sandstones, allowing it to record a long and complex geological history (Tuduri et al., 2023). Some of the grains studied may originate from weathered nearby igneous rocks, such as the granitic protoliths of the Izera Metamorphic Unit. Additionally, some monazite-(Ce) grains may have formed during one or more metamorphic or hydrothermal events associated with the region's complex geological evolution. The monazite-(Ce) grains studied from the St. Leopold mine and G-VI/22 borehole are characterized by different ThO_2 and CaO contents. This may be ascribed to hydrothermal alteration of primary monazite as the reaction of a metamorphic fluid phase that delivered Ca and Th to the monazite (Finger et al., 1998; Budzyń et al., 2010). Žáčková et al. (2010) described monazite grains from the Czech part of the Izera-Kowary Unit, which is relevant to the northern part of the massif (Jeřábek et al., 2016), as of two generations: thorium rich (~7–11 wt.% ThO_2); and with lower Th content (<5 wt.% ThO_2) being inclusions in garnets. The laser ablation (LA-ICP-MS) and EPMA dating of high-Th monazites indicates an age of 330 ±10 Myr which is interpreted as representing the high-pressure metamorphism at least in part of the Karkonosze-Izera Complex. Dating of low-Th mona-

Table 6

Mean EPMA analyses of xenotime-(Y) from the Stara Kamienica schists

Sample point	K-II/3
n =	18
Y_2O_3	41.16
P_2O_5	34.40
Dy_2O_3	7.17
Er_2O_3	3.82
Gd_2O_3	3.20
Yb_2O_3	3.11
Ho_2O_3	1.30
FeO	1.23
UO_2	1.00
Tb_2O_3	0.79
Lu_2O_3	0.66
Sm_2O_3	0.46
Tm_2O_3	0.33
Eu_2O_3	0.32
Nd_2O_3	0.14
PbO	0.05
SiO_2	0.36
CaO	0.02
ThO_2	0.01
Total	99.71
Y	0.717
P	0.986
Dy	0.078
Er	0.041
Gd	0.036
Yb	0.032
Ho	0.014
Fe^{3+}	0.035
U	0.015
Tb	0.009
Lu	0.007
Sm	0.005
Tm	0.003
Eu	0.004
Nd	0.002
Pb	0.000
Si	0.012
Ca	0.001
Th	0.000
Total	1.998
REE+Y	0.948

Atoms per formula unit (apfu) calculated to 4 oxygen and 2 cations

zite was burdened with high uncertainty due to the low radiogenic Pb contents and surplus Si + Ca relative to Th+U, which may indicate impurities or alteration. Elevated Ca contents in some monazite-(Ce) grains have been also recorded in this study as possibly representing cheralite substitution (Fig. 5D). EPMA U-Th-total Pb dating of hydrothermal uraninite associated both with ore minerals and REE-bearing minerals from the same samples as data in this work indicates similar ages (301.6 ±7 Myr, 348.6 ±12.5 Myr, and 362 ±8 Myr; Małek and Mikulski, 2024) to those of Zygo et al. (2023) who provided LA-ICP-MS dates of cassiterite from the Gierczyn-Przecznica area of 353 ±14, 360 ±5 and 318 ±6 Myr. These ages may suggest genetic connection between the cassiterite, uraninite and monazite (330 ±10 Myr; Žáčková, 2010), as possible different stages of regional metamorphism together with hydrothermal activity of late-stage Karkonosze granite emplacement and cooling.

Allanite is a member of the epidote group, and its structure can accommodate large quantities of many chemical elements, including REE, mainly depending on the system composition rather than on the P-T conditions. This mineral testifies to the diversity of mineral formation environments, as well as to secondary processes such as metamictization and hydrothermal alteration (Gieré and Sorensen, 2004). Allanite (epidote) group solid solutions are well-known within many igneous, metamorphic and sedimentary rocks, and they can also be an important repository of Th and U (Mellado et al., 2022). Allanite grains can serve as recorders of continuous or discontinuous prograde and retrograde reactions and of the P-T-fluid-redox conditions of metamorphism. The transformation of allanite to monazite during low-to-medium-grade metamorphism is relatively well-known (Engi, 2017). Allanite commonly forms as a result of detrital, magmatic or metamorphic monazite alteration close to the biotite-in reaction. In contrast, allanite, at the transition between the chlorite and biotite zones, is consumed to form monazite during the staurolite-in reaction, at the transition between the garnet and the staurolite-kyanite zones. Thermodynamic modelling of the schists shows that the first metamorphic allanite appears at ~425°C and 4.5 kbar, and transforms to monazite at ~600°C and 7.5 kbar under specific conditions of allanite-monazite-xenotime phase relations during prograde metamorphism (Jantos et al., 2008; Goswami-Banerjee and Robyr, 2015). The paragenesis allanite+apatite takes place during retrograde metamorphism at the expense of monazite via fluid-assisted dissolution-precipitation processes at greenschist facies, commonly related to shear zones (Cenki-Tok et al., 2014; Mellado et al., 2022). In natural systems, under hydrothermal conditions, the replacement of allanite by numerous secondary phases, such as bastnäsite, synchysite, thorite, and monazite, has been previously reported (Gieré and Sorensen, 2004; Berger et al., 2008; Hanson et al., 2012; Uher et al., 2015; Gros et al., 2020; Gmochowska et al., 2024). The allanite-(Ce) grains of the Stara Kamienica schists studied show a variety of occurrence forms and of chemical compositions as their origin can be inferred as metamorphic, hydrothermal or even detrital. A total REE+Th+Mn+Sr vs. Al diagram shown in Figure 3 is contoured with Fe oxidation isolines. In general, igneous allanites have F_{ox} ratios buffered at ~0.4, vein allanites are variably oxidised, and metamorphic allanites are both oxidised and reduced (Petrik at al., 1995). Most of the allanite-(Ce) results from the Stara Kamienica schists shown on the diagram are centred around the 0.4 oxidation isoline, while results from the C-X/46 borehole (Czerniawa-Zdrój area) are clearly more oxidised with simultaneous REE escape, which may indicate the activity of hydrothermal solutions. Thermodynamic modelling of allanite precipitation in schists (~425°C and 4.5 kbar; Goswami-Banerjee and Robyr, 2015) is consistent with the metamorphism determinations of the Stara Kamienica schists made by other authors, e.g. Kozłowski (1974) together with Szałamacha and Szałamacha (1974) constrains metamorphism conditions to ~500–550°C and 6 ±1 kbar based on almandine and hornblenda occurrence in amphibolites within the schists based on facies comparison (after Eskola, 1920) and degrees of metamorphism according to Winkler (1967). Makała (1994) points to a metamorphism temperature of up to 450–616°C with pressures of 2–4 kbar

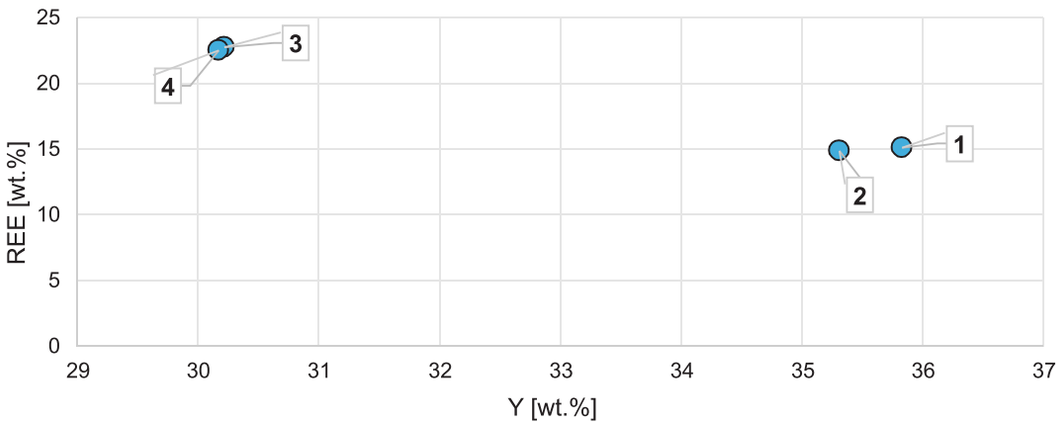

Fig. 7. REE *versus* Y diagram of the chemical composition of zonal xenotime-(Y) from Figure 6A

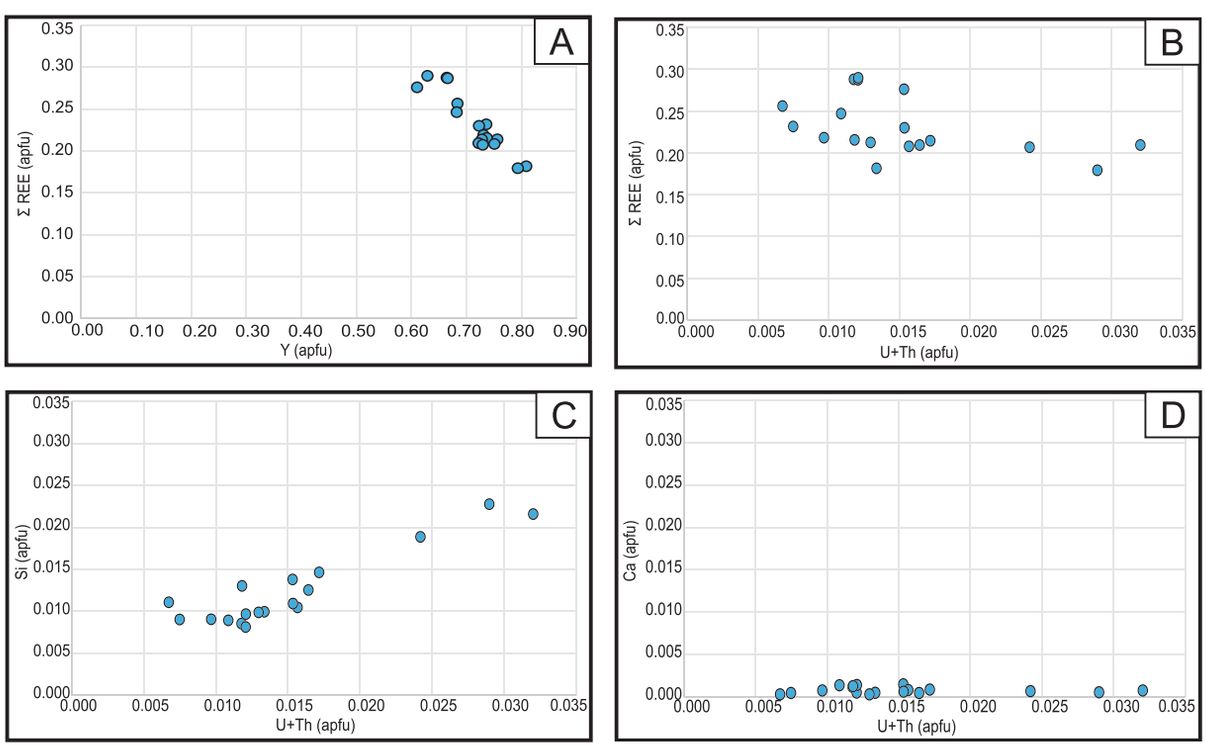

Fig. 8. Xenotime-(Y) mineral chemistry plots

A – Σ REE *versus* Y; **B** – Σ REE versus U+Th; **C** – Si *versus* U+Th, a coffinite [$U(SiO_4)(OH)_4$] substitution; **D** – Ca *versus* U+Th, a cheralite [$CaTh(PO_4)_2$] substitution (after Broska and Petrik, 2008; Švecová et al., 2016)

based on biotite-garnet mineral pair observations. In turn, Marcinowska and Kozłowski (1997) set the metamorphism temperature to 470–600°C with 3–5 kbar pressure through studying fluid inclusions in rock-forming minerals of the Stara Kamienica schists. Michniewicz et al. (2006) determined metamorphism conditions of 470–550°C and 1.5–3.8 kbar based on the margarite stability range and other geological indications such as the absence of kyanite and sillimanite, the existence of parageneses containing muscovite, quartz and staurolite, the contents of spessartine and pyrope particles in the schist garnets and the composition of the chloritoid. The presence of possibly metamorphic allanite-(Ce) with specified precipitation conditions (~425°C and 4.5 kbar) may corroborate the deductions noted of the Stara Kamienica schists metamorphism conditions, but detailed observations focused on more allanite grains and geochemical data are still required.

The occurrence of REE fluorocarbonates and plumbogummite in the Stara Kamienica schists remains insufficiently recognized. The principal REE (Ln) fluorocarbonate minerals from an economic standpoint are bastnäsite [$Ln(CO_3)F$], para-

Table 7

Shortened chemical composition of zonal xenotime-(Y) from Figure 6A – WDS analysis [wt.%]

WDS point#	Y_2O_3	P_2O_5	Nd_2O_3	Eu_2O_3	Sm_2O_3	Gd_2O_3	Tb_2O_3	Dy_2O_3	Ho_2O_3	Er_2O_3	Tm_2O_3	Yb_2O_3	Lu_2O_3
1	45.50	35.15	0.02	0.19	0.07	1.14	0.41	5.89	1.36	4.17	0.25	3.28	0.48
2	44.84	34.58	0.07	0.20	0.09	1.03	0.35	5.29	1.29	4.20	0.39	3.48	0.60
3	38.38	34.12	0.40	0.82	1.06	5.83	1.30	9.61	1.43	2.93	0.30	1.79	0.67
4	38.31	34.44	0.31	0.82	1.03	5.60	1.35	9.90	1.33	2.97	0.26	1.73	0.52

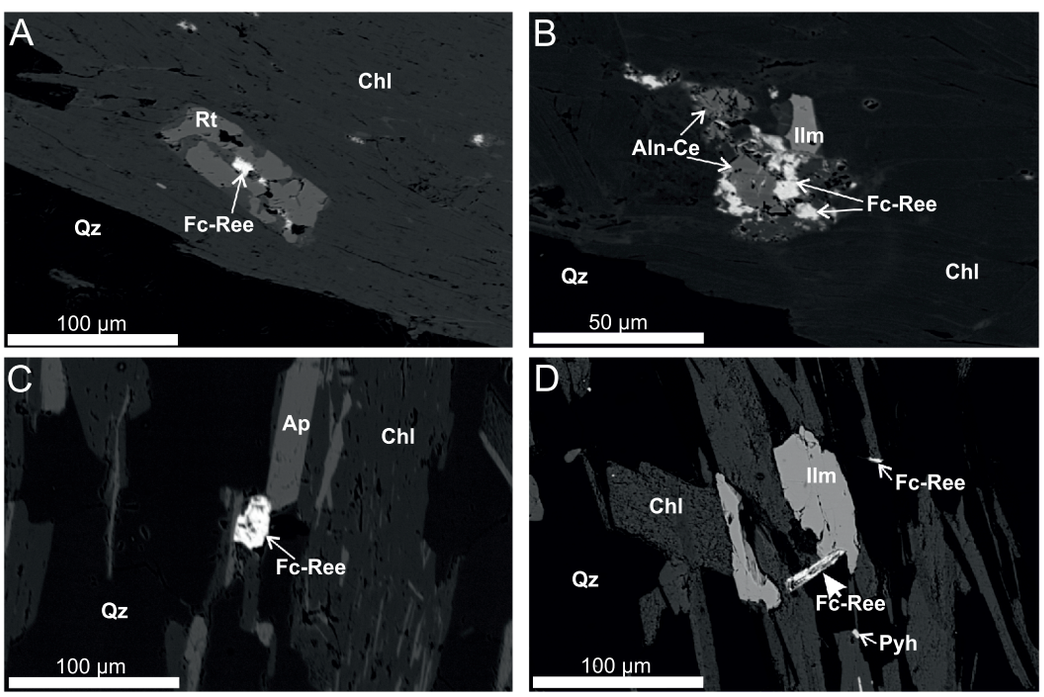

Fig. 9A – intergrowth of REE fluorocarbonate (Fc-Ree) with rutile (Rt) fracture in chlorite (Chl)-quartz (Qz) schist, Czerniawa C-X/46 borehole, BSEI; B – growth of REE fluorocarbonate with allanite-(Ce) (Aln-Ce) and ilmenite (Ilm) in chlorite–quartz schist, Czerniawa C-X/46 borehole, BSEI; C – isolated REE fluorocarbonate grain adjacent to apatite (Ap) in chlorite-quartz schist, Krobica K-II/3 borehole, BSEI; D – REE fluorocarbonates as growths with ilmenite and as an isolated grain adjacent to pyrrhotite (Pyh) in chlorite-quartz schist, Gierczyn G-I/13 borehole, BSEI

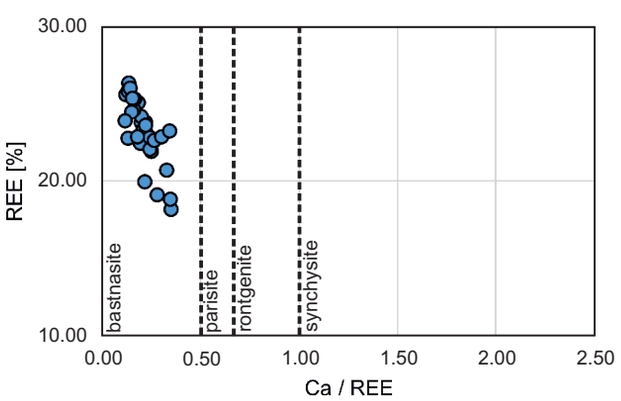

Fig. 10. Most common REE (Ce; %) *versus* Ca/REE ratio classification plot for REE fluorocarbonates (after Meng et al., 2002; Niegisch et al., 2020)

site [$Ln_2Ca(CO_3)_3F_2$] and synchysite [$LnCa(CO_3)_2F$], but this group contains many more mineral phases (Williams-Jones and Wood, 1992). Because of the absence of carbon from the analytical results (due to the carbon coating of the thin sections), the precise identification is uncertain, but plotting EMPA data on classification diagrams points to bastnäsite-(Ce) (Figs. 10 and 11). There are well-known occurrences of REE fluorocarbonates hosted by carbonatites (e.g., Mountain Pass, California; Olson et al.,1954), in sedimentary successions (e.g., Bayan Obo, China; Chao et al., 1989), in some peralkaline granites and syenites (e.g., Thor Lake, Canada; Trueman et at., 1988) as well as in many hydrothermal systems (mostly epithermal) for example in Muso, Columbia (Ottaway et al., 1994) and Schwarzwald, Germany (von Gehlen et al., 1986). REE fluorocarbonates commonly occur in the Stara Kamienica schists and the evidence points to its hydrothermal origin.

Plumbogummite is a member of the mineral group that comprises phosphate representatives of the alunite supergroup. Minerals of this group are commonly found in weathering

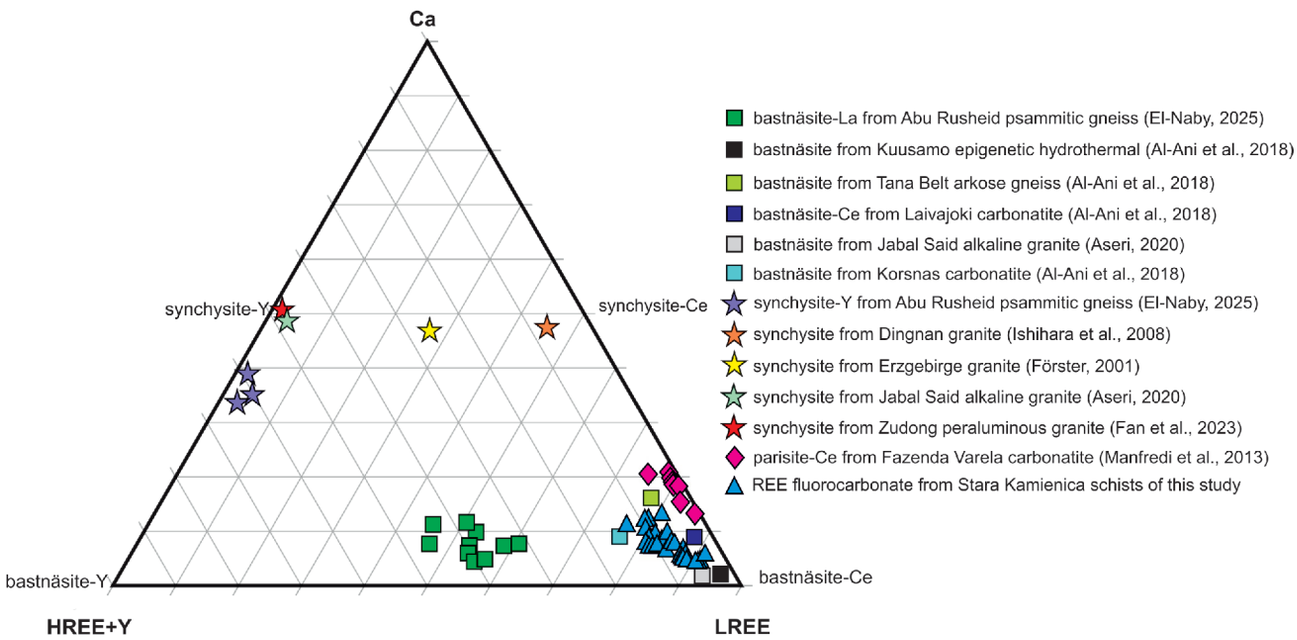

Fig. 11. Ternary plot of REE-fluorocarbonate chemical composition with data from the Stara Kamienica schist belt marked

zones of Pb ore deposits as moderately rare secondary minerals and occur especially within carbonatites and various sedimentary rocks as well as those of hydrothermal origin (Kruszewski and Dec, 2018). Environmental studies indicate that they may crystallize from acidic mine waters thus immobilizing some toxic metals (Bigham and Nordstrom, 2000; Kolitsch and Pring, 2001; Dzikowski et al., 2006). Plumbogummite minerals show elevated amounts of trace elements such as Ni, Tl, Cr, Cu, V, Ag, Zr, and Ti as well as REEs (e.g., Bayliss et al., 2010). Plumbogummite has been found in only one sample from the St. Leopold adit in Krobica. Its presence in this historic mining site is consistent with environmental data indicating that it may crystallize from acidic mine waters. At this stage, the small amount of plumbogummite data precludes more detailed conclusions and further studies are required.

WHOLE-ROCK ANALYSIS

A slight enrichment in Ce (71.7 vs. 68 ppm) and La (40.7 vs. 32 ppm) is observed in the Stara Kamienica schist samples compared to the average concentrations reported for continental crust (Barbalace, 2019). The remaining rare earth elements show a general depletion relative to the continental crust average. As regards total REE content relative to the sampling area, the highest value (329.75 ppm) was obtained for the Krobica region (middle part of the Stara Kamienica schist belt). Slightly lower values were obtained for Przecznica (308.03 ppm), the Gierczyn area (299.18 ppm, middle to eastern part of the Stara Kamienica schist belt). Czerniawa-Zdrój, the westernmost part of the Polish part of the Stara Kamienica belt, is characterized by 255.27 ppm of total REE.

REE concentration patterns for samples from the Stara Kamienica schist belt, normalized to chondrite values (McDonough and Sun, 1995), reveal a marked enrichment in LREE relative to HREE, as well as an overall increase in total REE contents, reaching up to several hundred times chondritic values. Both negative and positive europium (Eu) anomalies are present. In contrast, REE distribution diagrams normalized to European shales (Bau et al., 2018) and to PAAS (McLennan, 1989) indicate a generally flat curve and overall REE depletion relative to these reference compositions, with only a few samples showing minor enrichment. The REE distribution of the Stara Kamienica samples reflects REE proportions similar to that of medium shale (medium continental crust) with no significant REE fractionation. As a sedimentary-volcanic protolith of the shales can be assumed, that detrital material comes from a typical continental source, without strong sorting effects or selective transport of elements. The sample selection was focused on ore mineralization. Even though REE mineralization can be, at least partly, genetically connected with the same mineralisation processes as ore minerals, the distribution of REE-bearing minerals within the Stara Kamienica schists is still unconstrained. The presence of REE concentration zones within the Stara Kamienica schists cannot be excluded as regards further mineral exploration.

Most samples display a distinct positive Eu anomaly. Such REE enrichment or depletion is generally attributed to the preferential partitioning of Eu into plagioclase. Under stable magma crystallization conditions, Eu is largely incorporated into plagioclase, resulting in a relative enrichment of Eu compared to other REEs in this mineral (positive Eu anomaly). The residual magma consequently becomes depleted in Eu. If this Eu-depleted melt is separated from crystallized plagioclase, its chemical composition reflects a negative Eu anomaly. Conversely, if

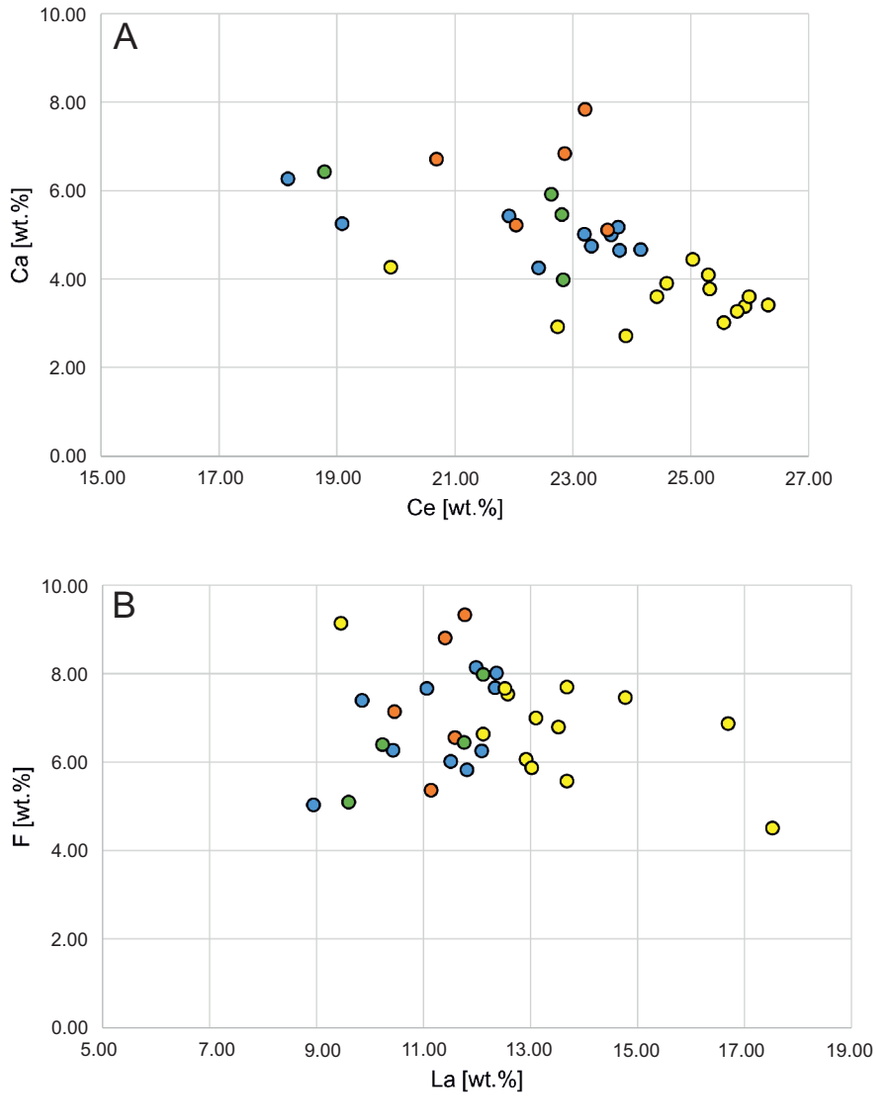

Fig. 12A – Ca *versus* Ce and B – F *versus* La compositional plots of REE fluorocarbonates from the Stara Kamienica schist belt

Blue dots – Czerniawa-Zdrój results (C-X/46 borehole), yellow dots – Krobica results (K-II/3 borehole), green and orange dots – Gierczyn results (G-III/17 and G-I/13 boreholes respectively)

Table 8

Statistics of REE contents in REE fluorocarbonates from the Stara Kamienica schists (wt.%, n – statistical group)

REE fluorocarbonate (n = 32)	La_2O_3	Ce_2O_3	Pr_2O_3	Nd_2O_3	Sm_2O_3	Gd_2O_3	Dy_2O_3	SrO	Y_2O_3
Minimum	10.48	21.29	2.28	8.14	1.41	0.93	0.00	0.06	0.68
Maximum	20.54	30.83	3.60	15.17	2.80	4.67	1.00	0.38	4.66
Arithmetic mean	14.22	27.23	2.98	11.54	1.97	2.22	0.49	0.20	2.77
Median	14.11	27.47	2.99	11.41	1.96	2.02	0.49	0.19	2.63
Standard deviation	2.16	2.44	0.30	1.74	0.30	0.89	0.28	0.07	0.89

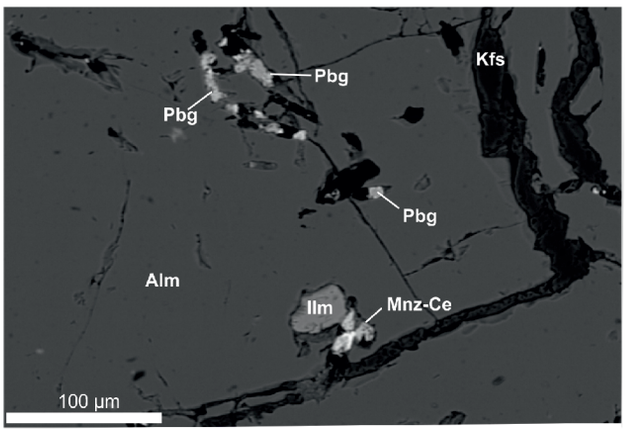

Fig. 13. Xenomorphic plumbogummite (Pbg) grains as fracture fillings in almandine (Alm); ilmenite (Ilm), K-feldspar (Kfs) and monazite-(Ce) (Mnz-Ce) as inclusions in almandine, St. Leopold adit, BSEI

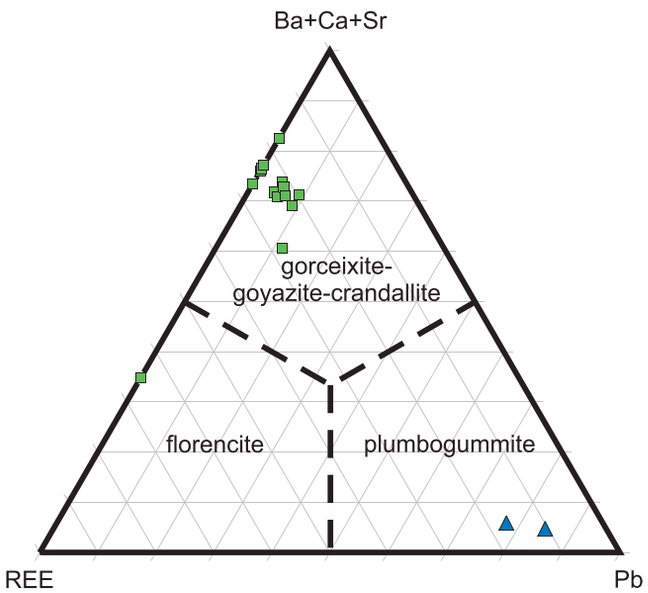

Fig. 14. Compositional ternary plot of plumbogummite group minerals in the alkaline metal-REE-Pb system

Blue triangles – data from this study, green squares – results of Kruszewski and Dec, 2018 (wt.%)

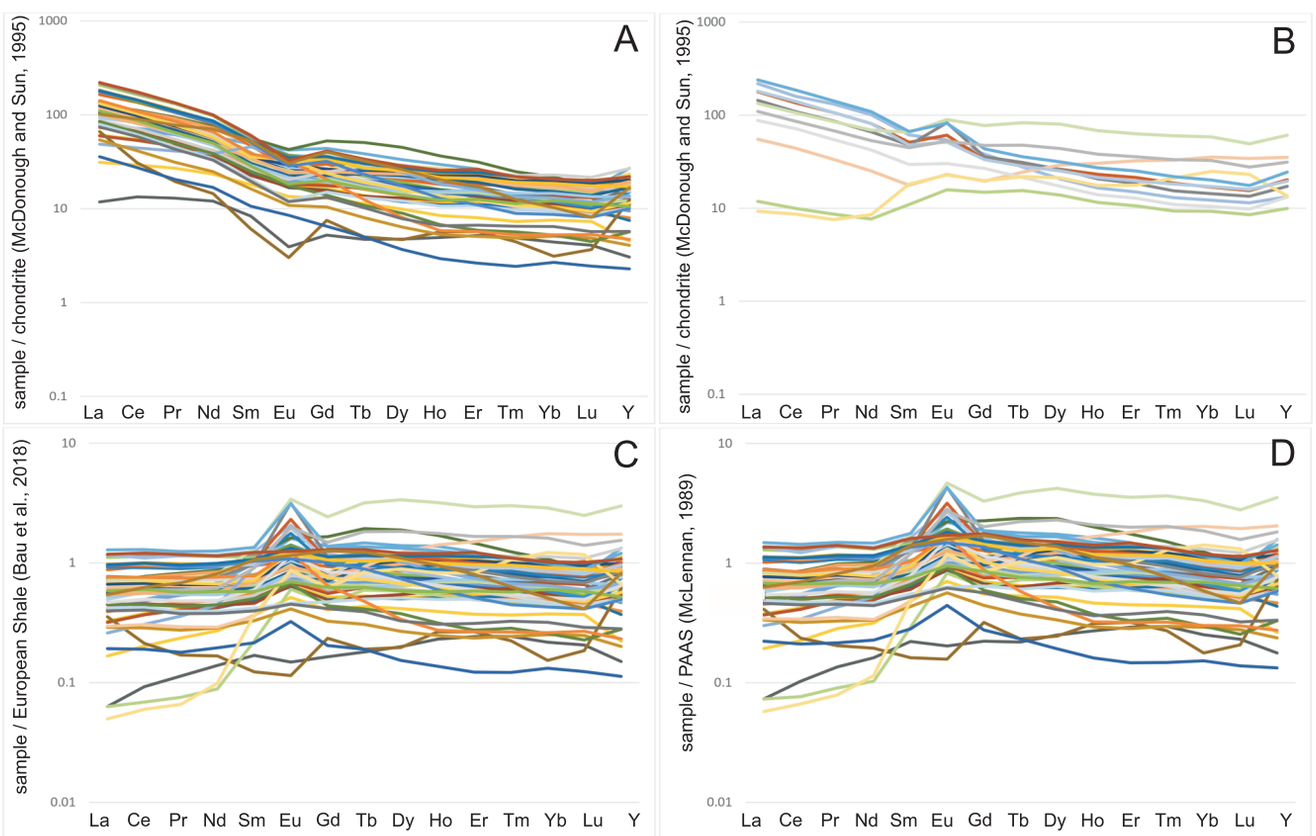

Fig. 15A – REE results normalized to chondrite with a negative europium anomaly; B – REE results normalized to chondrite with a positive europium anomaly; C – REE results normalized to European shales; D – REE results normalized to PAAS

Lines explained in Appendix 1I

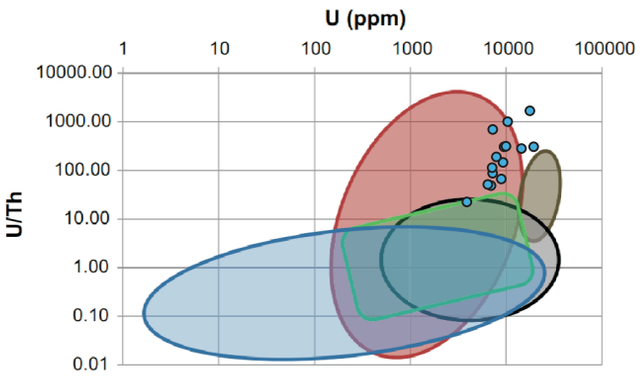

Fig. 16. U vs. U/Th diagram for xenotime showing fields for igneous (black), metamorphic (green), diagenetic (red), hydrothermal and metasomatic (blue) and unconformity-related U-deposits (brown; after McNaughton and Rasmussen, 2018)

magma accumulates crystallized plagioclase, a positive Eu anomaly develops in its composition (Weill and Drake, 1973; Bau, 1991). In the case of the Stara Kamienica schists, as a feldspar-poor metasedimentary rock, the Eu anomaly is not clearly interpretable. The absence of significant feldspar means that the typical process of Eu enrichment via feldspar crystallization is limited. Additionally, positive Eu anomalies may also indicate the local influence of hydrothermal fluids (Bau et al., 2014; Michard and Albarède, 1986).

CONCLUSIONS

Micro-scale observations combined with WDS chemical composition analyses of REE-bearing minerals, along with whole-rock trace element determinations using the ICP-MS method, on samples from the Stara Kamienica schist belt have led to the following conclusions:

– **Multiple REE carriers have been identified:** allanite-(Ce), monazite-(Ce), REE fluorocarbonates, plumbo-

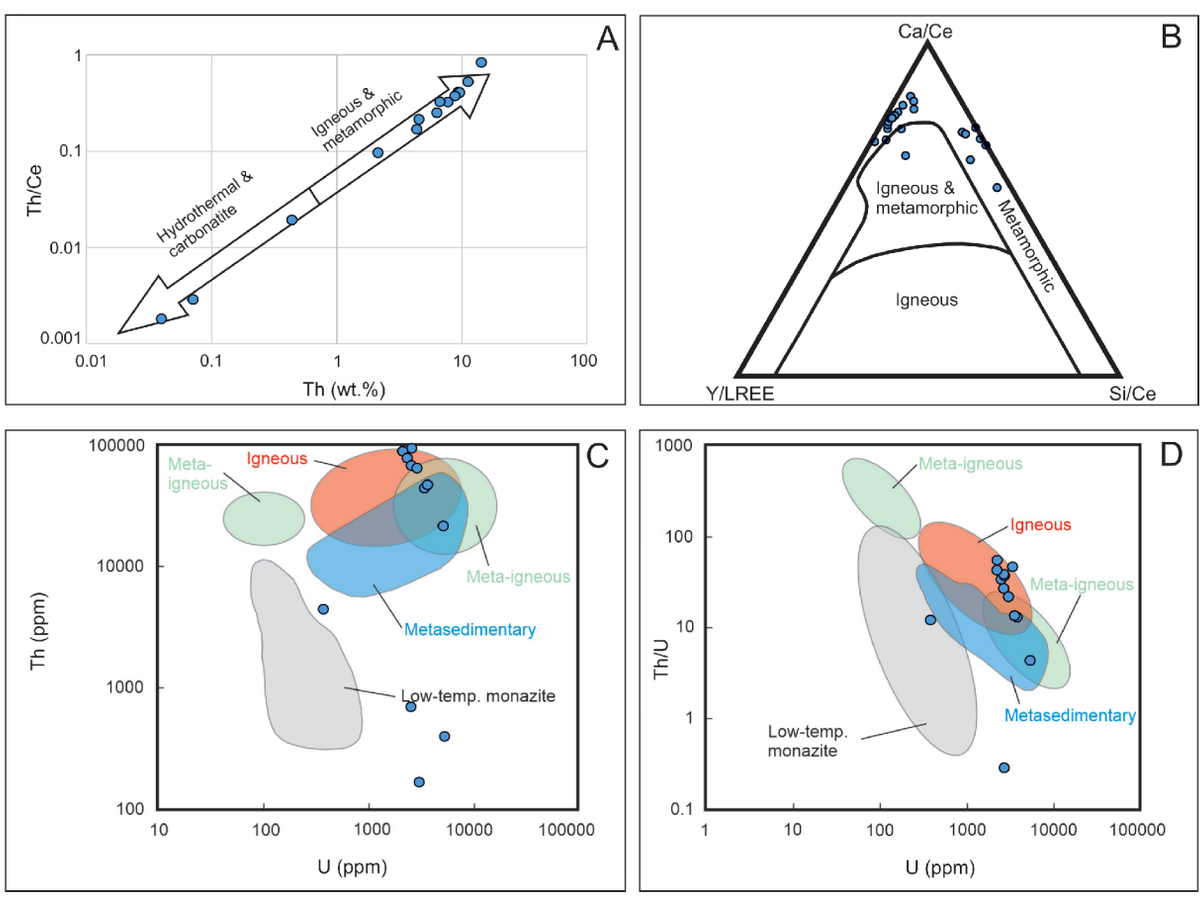

Fig. 17A, B – monazite-(Ce) origin discrimination charts (modified after Wu et al., 2019; Liu et al., 2022); C, D – binary plots of monazite-(Ce) trace element data

Red, green, blue and grey fields from Aleinikoff et al. (2012, 2023)

gummite, and xenotime-(Y) were found to be the main REE-bearing mineral phases in the Stara Kamienica schist belt, with allanite-(Ce), fluorocarbonates and plumbogummite documented for the first time in this area.

– The highest REE content in whole-rock samples was obtained for the Krobica region (middle part of the Stara Kamienica schist belt).

– **Ambiguous formation environment of xenotime-(Y):** both this study and previous research (Bobiński et al., 2004; Michniewicz et al., 2006) reveal pronounced chemical zoning in xenotime-(Y), indicating complex crystallization histories and fractionation of REE subgroups during mineral growth. Xenotime-(Y) grain morphology and internal structures suggest a pre-metamorphic, likely detrital and/or hydrothermal origin, altered during regional metamorphism. However, U/Th ratios plot mostly within the diagenetic field, making the primary formation environment uncertain.

– **Complex provenance of monazite**: monazite-(Ce) grains in the Stara Kamienica schist belt show evidence of both detrital and metamorphic origins, with trace element signatures indicating predominantly igneous and metamorphic sources, and minor hydrothermal contributions.

– **Whole-rock geochemistry:** the Stara Kamienica schist samples are slightly enriched in Ce and La compared to the average continental crust but generally depleted in other REEs. Their REE normalization to chondrite patterns shows LREE enrichment over HREE, and variable Eu anomalies the interpretation of which in feldspar-poor rocks is unclear but can point to hydrothermal activity.

– Numerous REE-carrying minerals were identified, but the spatial distribution of REE concentration within the Stara Kamienica mineralized area is still poorly constrained. REE-bearing minerals are concentrated within mica layers of the schists together with ore minerals. Because of the possible genetic connection of at least part of the REE-bearing minerals with Sn-polymetallic mineralization (regional metamorphism and hydrothermal activity) **the presence of REE-enriched horizons is possible.**

Acknowledgements. This article is part of Rafał Małek's doctoral dissertation titled "Mineralogical-geochemical study and genesis of rare and accompanying elements occurrence within the tin-bearing deposit mineralization of the Stara Kamienica schist belt in the Sudetes" under the supervision of S.Z. Mikulski. The author would like to kindly thank and express gratitude to the editor, J. Szczepański, as well as the reviewers for the time and effort they dedicated to help improve this manuscript.

REFERENCES

Al-Ani, T., Molnár, F., Lintinen, P., Leinonen, S., 2018. Geology and mineralogy of rare earth elements deposits and occurrences in Finland. Minerals, **8**, 356; https://doi.org/10.3390/min80 80356

Aleinikoff, J.N., Grauch, R.I., Mazdab, F.K., Fanning, C.M., Kamo, S., 2012. SHRIMP U-Pb and trace element evidence from an unusual monazite-xenotime gneiss for multiple thermal events in the Hudson Highlands. American Journal of Science, **312:** 723–765; https://doi.org/10.2475/07.2012.02

Aleinikoff, J.N., Scott Southworthb, S., Fanning, C.M., 2023. SHRIMP U-Pb geochronology of Mesoproterozoic basement and overlying Ocoee Supergroup, NC–TN: dating diagenetic xenotime and monazite overgrowths on detrital minerals to determine the age of sedimentary deposition. Canadian Journal of Earth Sciences, **60:** 583–615; https://doi.org/dx.doi.org/10.1139/cjes-2022-0093

Aseri, A.A., 2020. Rare-metal alkaline granite from the Arabian Shield, Saudi Arabia. Ph.D. Thesis, University of Western Ontario, Ontario.

Barbalace, K., 2019. Periodic Table of Elements. EnvironmentalChemistry.com

Bau, M., 1991. Rare-earth element mobility during hydrothermal and metamorphic fluid-rock interaction and the significance of the oxidation state of europium. Chemical Geology, **93:** 219–230; https://doi.org/10.1016/0009-2541(91)90115-8

Bau, M., Schmidt, K., Koschinsky, A., Hein, J., Kuhn, T., Usui, A., 2014. Discriminating between different genetic types of marine ferro-manganese crusts and nodules based on rare earth elements and yttrium. Chemical Geology, **381:** 1–9; https://doi.org/10.1016/j.chemgeo.2014.05.004

Bau, M., Schmidt, K., Pack, A., Bendel, V., Kraemer, D., 2018. The European Shale: an improved data set for normalisation of rare earth element and yttrium concentrations in environmental and biological samples from Europe. Applied Geochemistry, **90:** 142–149; https://doi.org/10.1016/j.apgeochem.2018.01.008

Bayliss, P., Kolitsch, U., Nickel, E.H., Pring, A., 2010. Alunite supergroup: recommended nomenclature. Mineralogical Magazine, **74:** 919–927; https://doi.org/10.1180/minmag.2010.074.5.919

Berendsen, P., Speczik, S., Wiszniewska, J., 1987. Sulphide geochemical studies of the stratiform tin deposits in the Stara Kamienica Chain (SW Poland). Archiwum Mineralogiczne, **42**: 31–42.

Berger, A., Gnos, E., Janots, E., Fernandez, A., Giese, J., 2008. Formation and composition of rhabdophane, bastnäsite and hydrated thorium minerals during alteration: implications for geochronology and low-temperature processes. Chemical Geology, **254:** 238–248; https://doi.org/10.1016/j.chemgeo.2008.03.006

Bigham, J.M., Nordstrom, D.K., 2000. Iron and aluminum hydroxy-sulfates from acid sulfate waters. Reviews in Mineralogy and Geochemistry, **40:** 351–403; https://doi.org/10.2138/rmg.2000.40.7

Bobiński, W., 1991. Wrostki kasyterytu w minerałach skałotwórczych (in Polish). In: Mineralizacja Sn i jej pozycja w ewolucji geologicznej pasma Kamienieckiego (Góry Izerskie – Sudety Zachodnie). Materiały CXXXI Sesji Nauk PIG: 23.

Bobiński, W., Siemiątkowski, J., Starnawska, E., 2004. Xenotime in mica schist with cassiterite mineralization in Stara Kamienica Range (in Polish with English summary). Przegląd Geologiczny, **52:** 61–63.

Borkowska, M., Hameurt, J., Vidal, P., 1980. Origin and age of the Izera gneisses and Rumburk granites in the Western Sudetes. Acta Geologica Polonica, **30:** 122–146.

Broska, I., Petrik, I., 2008. Genesis and stability of accessory phosphates in silicic magmatic rocks: a Western Carpathian case study. Mineralogia, **39:** 53–65; https://doi.org/10.2478/v10002-008-0004-6

Budzyń, B., Hetherington, C.J., Williams, M.L., Jercinovic, M.J., Michalik, M., 2010. Fluid-mineral interactions and constraints on monazite alteration during metamorphism. Mineralogical Magazine, **74:** 659–681; https://doi.org/10.1180/minmag.2010.074.4.659

Burda, J., Klötzli, U., Woskowicz-Ślęzak, B., Li, Q.-L., Liu, Y., 2020. Inherited or not inherited: complexities in dating the atypical 'cold' Chopok granite (Nízke Tatry Mountains, Slovakia). Gondwana Research, **87:** 138–161; https://doi.org/10.1016/j.gr.2020.05.018.

Cenki-Tok, B., Darling, J., Rolland, Y., Dhuime, B., Storey, C.D., 2014. Direct dating of mid-crustal shear zones with synkinematic allanite: new in situ U-Th-Pb geochronological approaches applied to the Mont Blanc massif. Terra Nova, **26**: 29–37; https://doi.org/doi:10.1111/ter.12066

Chao, E.C.T., Minkin, J.A., Back, J.M., Okita, P.M., McKee, E.H., Tosdal, R.M., Tatsumoto, M., Junwen, W., Edwards, C.A., Yingzhen, R., Weijun, S., 1989. The H8 dolomite host rock of the Bayan Obo iron-niobium-rare-earth-element ore deposit of Inner Mongolia, China-Origin, episodic mineralization and implications. USGS Circular, **1035:** 8–10.

COM, 2017. European Commission. Communication from the Commission to the European Parliament, the Council, the European Economic and Social Committee and the Committee of the Regions: On the 2017 List of Critical Raw Materials for the EU; 490 final; European Commission: Brussels, Belgium.

Cook, N.J., Dudek, K., 1994. Mineral chemistry and metamorphism of garnet chlorite–mica schist associated with cassiterite–sulphide mineralization from the Kamienica Range, Izera Mountains, S.W. Poland. Chemie der Erde, **54**: 1–32.

Crow, J.M., 2011. 13 exotic elements we can't live without. The New Scientist, **210**: 36–41.

Deer, W.A., Howie, R.A., Zussman, J., 1986. Rock-forming Minerals, **1B**: Disilicates and ringsilicates (2nd edition). Longman, Harlow, United Kingdom.

Dzikowski, T.J., Groat, L.A., Jambor, J.L., 2006. The symmetry and crystal structure of gorceixite, $BaAl_3[PO_3(O,OH)]_2(OH)_6$, a member of the alunite supergroup. The Canadian Mineralogist, **44:** 951–958. https://doi.org/10.2113/gscanmin.44.4.951

El-Naby, H.H.A., 2025. The genesis of the supergene REE-fluorocarbonate and uranyl mineralization in the Abu Rusheid area of the South Eastern Desert of Egypt. Geosciences Journal, **29:** 49–70; https://doi.org/10.1007/s12303-025-00023-6

Eskola, P., 1920. The mineral facies of rocks. Norsk Geologisk Tidsskrift, **6:** 143–194.

Engi, M., 2017. Petrochronology based on REE-minerals: monazite, allanite, xenotime, apatite. Reviews in Mineralogy and Geochemistry, **83:** 365–418; https://doi.org/10.2138/rmg.2017.83.12

Fan, C., Xu, C., Shi, A., Smith, M.P., Kynicky, J., Wei, C., 2023. Origin of heavy rare earth elements in highly fractionated peraluminous granites. Geochimica et Cosmochimica Acta, **343:** 371–383; https://doi.org/10.1016/j.gca.2022.12.019

Finger, F., Broska, I., Roberts, M., Schermaier, A., 1998. Replacement of primary monazite by apatite-allanite-epidote coronas in an amphibolite facies granite gneiss from the Eastern Alps. American Mineralogist, **83:** 248–258; https://doi.org/10.2138/am-1998-3-408

Foltyn, K., Bertrandsson Erlandsson, V., Kozub-Budzyń, G.A., Melcher, F., Piestrzyński, A., 2020. Indium in polymetallic mineralisation at the Gierczyn mine, Karkonosze-Izera Massif, Poland: results of EPMA and LA-ICP-MS investigations. Geological Quarterly, **64**: 74–85; https://doi.org/10.7306/gq.1516

Förster, H.J., 2001. Synchysite-(Y)–synchysite-(Ce) solid solutions from Markersbach, Erzgebirge, Germany: REE and Th mobility during high-T alteration of highly fractionated aluminous A-type granites. Mineralogy and Petrology, **72:** 259–280; https://doi.org/10.1007/s007100170019

Franke, W., Żelaźniewicz, A., 2000. The eastern termination of the Variscides: terrane correlation and kinematic evolution. Geological Society Special Publications, **179**: 63–86; https://doi.org/10.1144/gsl.sp.2000.179.01.06

Gieré, R., Sorensen, S.S., 2004. Allanite and other: REE-rich epidote-group minerals. Reviews in Mineralogy and Geochemistry, **56**: 431–493; https://doi.org/10.2138/gsrmg.56.1.431

Gmochowska, W., Wirth, R., Słaby, E., Anczkiewicz, R., Krzątała, A., Roddatis, V., Sláma, J., Kozub-Budzyń, G., Bhattacharya, S., Schreiber, A., 2024. Hydrothermal alteration of accessory minerals (allanite and titanite) in the late Archean Closepet granitoid (Dharwar Craton, India): a TEM study. Geochemistry, **84**, 126130; https://doi.org/10.1016/j.chemer.2024.126130.

Goswami-Banerjee, S., Robyr, M., 2015. Pressure and temperature conditions for crystallization of metamorphic allanite and monazite in metapelites: a case study from the Miyar Valley (High Himalayan Crystalline of Zanskar, NW India). Journal of Metamorphic Geology, **33:** 535–556; https://doi.org/10.1111/jmg.12133

Gros, K., Słaby, E., Jokubauskas, P., Slama, J., Kozub-Budzyń, G., 2020. Allanite geochemical response to hydrothermal alteration by alkaline, low-temperature fluids. Minerals, **10**, 392; https://doi.org/10.3390/min10050392

Hanson, S.L., Falster, A.U., Simmons, W.B., Brown, T.A., 2012. Allanite-(Nd) from the Kingman feldspar mine, Mojave pegmatite district, Northwestern Arizona, USA. Canadian Mineralogist, **50:** 815–824. https://doi.org/10.3749/canmin.50.4.815

Harlov, D.E., 2024. Experimental incorporation of U into xenotime at mid to lower crustal pressures and temperatures utilizing alkali-bearing fluids under reducing and oxidizing conditions. Chemical Geology. **662:** 1–10; https://doi.org/10.1016/j.chemgeo.2024.122192

Harlov, D.E., Procházka, V., Förster, H.J., Matějka, D., 2008. Origin of monazite–xenotime–zircon–fluorapatite assemblages in the peraluminous Melechov granite massif, Czech Republic. Mineralogy and Petrology. **94**: 9–26; https://doi.org/10.1007/s00710-008-0003-8

Harańczyk, C., Skiba, M., 1961. Gahnite from tin-bearing zone of Krobica-Gierczyn-Przecznica in Lower Silesia. Bulletin de l'Académie Polonaise des Sciences, Série des Sciences Géologiques et Géographiques, **9:** 149–154.

He, H., Yang, W., 2022. REE mineral resources in China: review and perspective. Geotectonica et Metallogenia, **46:** 829–841; https://doi.org/10.16539/j.ddgzyckx.2022.05.001

Hetherington, C.J., Harlov, D.E., 2008. Metasomatic thorite and uraninite inclusions in xenotime and monazite from granitic pegmatites. Hidra anorthosite massif. southwestern Norway: Mechanics and fluid chemistry. American Mineralogist, **93:** 806–820; https://doi.org/10.2138/am.2008.2635

Ilnicki, S., 2010. Petrogenesis of continental mafic dykes from the Izera Complex, Karkonosze-Izera Block (West Sudetes, SW Poland). International Journal of Earth Sciences, **99:** 745–773; https://doi.org/10.1007/s00531-009-0433-5

Ishihara, S., Hua, R., Hoshino, M., Murakami, H., 2008. REE Abundance and REE minerals in granitic rocks in the Nanling Range, Jiangxi Province, Southern China, and generation of the REE-rich weathered crust deposits. Resource Geology, **58:** 355–372; https://doi.org/10.1111/j.1751-3928.2008.00070.x

Jantos, E., Engi, M., Berger, A., Allaz, J., Schwarz, O., Spandler, C., 2008. Prograde metamorphic sequence of REE minerals in pelitic rocks of the Central Alps: implications for allanite–monazite–xenotime phase relations from 250 to 610°C. Journal of Metamorphic Geology, **26:** 509–526; https://doi.org/10.1111/j.1525-1314.2008.00774.x

Jaskólski, S., 1960. Beitrag zur Kenntnis über die Herkunft der Zinnlagerstätten von Gierczyn (Giehren) im Iser-Gebirge, Niederschlesien. Neues Jahrbuch für Mineralogie Abhandlungen, **94:** 181–190.

Jaskólski, S., 1963. Erwagungen über die Genese Zinnführender Schiefer im Isergebirge (Niederschlesien). Prace Geologiczne, **12:** 33–53.

Jaskólski, S., Mochnacka, K., 1959. Złoże cyny w Gierczynie w Górach Izerskich na Dolnym Śląsku i próba wyjaśnienia jego genezy (in Polish). Archiwum Mineralogiczne, **22:** 17–106.

Jeřábek, P., Konopásek, J., Žáčková, E., 2016. Two-stage exhumation of subducted Saxothuringian continental crust records underplating in the subduction channel and collisional forced folding (Krkonoše-Jizera Mts., Bohemian Massif). Journal of Structural Geology, **89:** 214–229; https://doi.org/10.1016/j.jsg.2016.06.008

Karwowski, Ł., Włodyka, R., 1981. Stannite in the cassiterite-sulphide deposits of the Izera Mts. (Sudetes). Acta Geologica Polonica, **31:** 41–47.

Kolitsch, U., Pring, A., 2001. Crystal chemistry of the crandallite, beudantite and alunite groups: a review and evaluation of the suitability as storage materials for toxic metals. Journal of Mineralogical and Petrological Sciences, **96**: 67–78; https://doi.org/10.2465/jmps.96.67

Konopásek, J., Anczkiewicz, R., Jeřábek, P., Corfu, F., Žáčková, E., 2019. Chronology of the Saxothuringian subduction in the East Sudetes (Bohemian Massif, Czech Republic and Poland). Journal of the Geological Society, **176:** 492–504; https://doi.org/10.1144/jgs2018-173

Korytowski, A., Dörr, W., Żelaźniewicz, A., 1993. U-Pb dating of (meta)granitoids in the NW Sudetes (Poland) and their bearing on tectono-stratigraphic correlation. Terra Nova**, 5:** 331–332.

Kowalski, W., Karwowski, Ł., Śmietańska, I., Do Van Phi, 1978. Ore mineralization of the Stara Kamienica Schist Belt in the Izera Mountains (in Polish with English summary). Prace Naukowe Uniwersytetu Śląskiego, **243**: 7–89.

Kozłowska-Koch, M., 1965. Granitogneisses of the Izera Foothills (in Polish with English summary). Archiwum Mineralogiczne, **25:** 123–260.

Kozłowski, K., 1974. Crystalline schists and leucogranites of the Stara Kamienica-Świeradów-Zdrój Belt (Western Sudetes) (in Polish with English summary). Geologica Sudetica, **9:** 7–98.

Kröner, A., Hegner, E., Hammer, J., Haase, J., Haase, G., Bielicki, K.H., Krauss, M., Eidam, J., 1994. Geochronology and Nd-Sm systematics of Lysatian granitoids: significance for the evolution of the Variscan orogen in east-central Europe. Geologische Rundschau, **83:** 357–376.

Kröner, A., Jaeckel, P., Hegner, E., Opletal, M., 2001. Single zircon ages and whole rock Nd isotopic systematics of early Palaeozoic granitoid gneisses from the Czech and Polish Sudetes (Jizerské hory, Krkonoše and Orlice-Sněžník Complex). International Journal of Earth Sciences, **90:** 304–324; https://doi.org/10.1007/s005310000139

Kruszewski, Ł., Dec, M., 2018. Plumbogummite group minerals in Lower Devonian placoderm sandstones from Podłazie Hill, Holy Cross Mountains, Poland. Geological Quarterly, **62:** 353–360. https://doi.org/10.7306/gq.1410

Kryza, R., Muszynski, A., Vielzeuf, D., 1990. Glaucophane-bearing assemblage overprinted by greenschist-facies metamorphism in the Variscan Kaczawa complex, Sudetes, Poland. Journal of Metamorphic Geology, **8:** 344–355.

Kryza, R., Mazur, S., Pin, C., 1995. Leszczyniec meta-igneous complex in the eastern part of the Karkonosze–Izera Block, Western Sudetes: trace element and Nd isotope study. Neues Jahrbuch für Mineralogie Abhandlungen, **170:** 59–74; https://doi.org/10.1127/njma/170/1995/59

Kryza, R., Zalasiewicz, J., Mazur, S., Aleksandrowski, P., Sergeev, S., Larionov, A., 2007. Precambrian crustal contribution to the Variscan accretionary prism of the Kaczawa Mountains (Sudetes, SW Poland): evidence from SHRIMP dating of detrital zircons. International Journal of Earth Sciences, **96:** 1153–1162; https://doi.org/10.1007/s00531-006-0147-x

Kryza, R., Schaltegger, U., Oberc-Dziedzic, T., Pin, C., Ovtcharova, M., 2014. Geochronology of a composite granitoid pluton: a high-precision ID-TIMS U-Pb zircon study of the Variscan Karkonosze Granite (SW Poland). International Journal of Earth Sciences, **103:** 683–696; https://doi.org/10.1007/s00531-013-0995-0

Kucha, H., Mochnacka, K., 1998. Cassiterite micro inclusions in quartz and phyllosilicates from tin-bearing schists (Gierczyn, the Western Sudetes Mts., Poland) and their genetic significance. Mineralogica Polonica, **29:** 41–56.

Liu, X.H., Li, B., Xu, J.W., He, B., Liao, J., Peng, H.W., Lai, J.Q., 2022. Monazite geochronology and geochemistry constraints on the formation of the giant Zhengchong Li-Rb-Cs deposit in South China. Ore Geology Reviews, **150**, 105147; https://doi.org/10.1016/j.oregeorev.2022.105147

Machowiak, K., Armstrong, R., 2007. SHRIMP U–Pb zircon age from the Karkonosze granite. Mineralogia Polonica Special Papers, **31:** 193–196.

Majka, J., Mazur, S., Kosminska, K., Dudek, K., Klonowska, I., 2016. Pressure-temperature estimates of the blueschists from the Kopina Mt., northern Bohemian Massif, Poland – constraints on subduction of the Saxothuringian continental margin. European Journal of Mineralogy, **28:** 1047–1057; https://doi.org/10.1127/ejm/2016/0028-2601

Makała, A., 1994. Garnet-layer silicates paragenesis of metapelites from Stara Kamienica chain, Western Sudetes. Archiwum Mineralogiczne, **50:** 31–54.

Małek, R., Mikulski, S.Z., 2019. Geochemical-mineralogical research of the rare and associated element concentrations within cassiterite-sulphide mineralization in the Stara Kamienica schist belt in the Western Sudetes – preliminary results (in Polish with English summary). Przegląd Geologiczny, **67**: 179–182; https://doi.org/10.7306/2019.14

Małek, R., Mikulski, S.Z., 2024. EMPA U-Th-total Pb dating of uraninite from the Stara Kamienica schist belt (West Sudetes,SW Poland): new data towards interpreting the genesis of cassiterite-sulphide mineralization. Geological Quarterly, **68**, 36; https://doi.org/10.7306/gq.1764

M**ałek, R., Mikulski, S.Z., Chmielewski, A., 2019**. The geochemical-mineralogical characteristic of cassiterite-sulphide mineralization in the historic Saint John and Saint Leopold shafts in the Stara Kamienica schist belt (Western Sudetes) (in Polish with English summary). Przegląd Geologiczny, **67**: 910–920; https://doi.org/10.7306/2019.50

Manfredi, T.R., Bastos Neto, A.C., Pereira, V.P., Barbanson, L., Schuck, C., 2013. The parisite-(Ce) mineralization associated with the Fazenda Varela carbonatite (Correia Pinto, SC). Pesquisas em Geociencias, **40,** 295; https://doi.org/10.22456/1807-9806.77831

Marcinowska, A., Kozłowski, A., 1997. Inkluzje fluidów metamorficznych w metapelitach obszaru izerskiego (in Polish). Prace Specjalne PTM, **9:** 131–133.

Mazur, S., Aleksandrowski, P., 2001. The Teplá(?)/Saxothuringiansuture in the Karkonosze-Izera massif, Western Sudetes, Central European Variscides. International Journal of Earth Sciences, **90:** 341–360; https://doi.org/10.1007/s005310000146

McDonough, W.F., Sun, S., 1995. The composition of the Earth. Chemical Geology, **120:** 223–253; https://doi.org/10.1016/0009-2541(94)00140-4

McLennan, S.M., 1989. Rare earth elements in sedimentary rocks: influence of provenance and sedimentary processes. Reviews in Mineralogy, **21:** 169–200.

McNaughton, N.J., Rasmussen, B., 2018. Geochemical characterisation of xenotime formation environments using U-Th. Chemical Geology, **484:** 109–119; https://doi.org/dx.doi.org/10.1016/j.chemgeo.2017.08.016

Meng, D., Wu, X., Hab, Y., Meng, X., 2002. Polytypism and microstructures of the mixed-layer member B_2S, $CaCe_3(CO_3)_4F_3$ in the bastnaes-ite-(Ce)–synchysite-(Ce) series. Earth and Planetary Science Letters, **203:** 817–828; https://doi.org/10.1016/S0012-821X(02)00947-0

Mellado, E., Corbella, M., Kylander-Clark, A., 2022. Allanite in Variscan post-collisional lamprophyre dykes from Les Guilleries (NE Iberia) as a part of Rare Earth Elements Recycling in collisional orogens. Minerals, **12**, 954; https://doi.org/10.3390/min12080954

Michard, A., Albarède, F., 1986. The REE content of some hydrothermal fluids. Chemical Geology; **55**: 51–60; https://doi.org/10.1016/0009-2541(86)90127-0

Michniewicz, M., 1988. Cynonośne strefy rudne w Górach Izerskich między Czerniawą Zdrojem a Krobicą (in Polish). In: Metodyka rozpoznawania i dokumentowania złóż kopalin stałych. Rozpoznawanie i dokumentowanie złóż cyny. Materiały Seminarium: 5–20. Bierutowice. 10.06.1988. Wydaw. AGH, Kraków.

Michniewicz, M., Bobiński, W., Siemiątkowski, J., 2006. Tin mineralization in the middle part of the Stara Kamienica Schist Belt (Western Sudetes) (in Polish with English summary). Prace Państwowego Instytutu Geologicznego, **186.**

Mikulski, S.Z., Małek, R., 2019. Indium and other critical elements enrichment in cassiterite-sulphide Mineralization from the stratiform tin deposits in the West Sudetes (SW Poland). 15th SGA Biennial Meeting, 27–30 August 2019, Glasgow, Scotland, 4: 1818–1821.

Mikulski, S.Z., Kozłowski, A., Speczik, S., 2007. Fluid inclusion study of gold-bearing quartz-sulphide veins and cassiterite from the Czarnów As deposit ore (SW Poland). Proceedings of the Ninth Biennial SGA Meeting, Dublin 2007: 805–808.

Mikulski, S.Z., Oszczepalski, S., Sadłowska, K., Chmielewski, A., Małek, R., 2018. The occurrence of associated and critical elements in the selected documented Zn-Pb, Cu-Ag, Fe-Ti-V, Mo-Cu-W, Sn, Au-As and Ni deposits in Poland (in Polish with English summary). Biuletyn Państwowego Instytutu Geologicznego, **472**: 21–52; https://doi.org/10.5604/01.3001.0012.7113

Mikulski, S.Z., Williams, I.S., Stein, H.J., Wierchowiec, J., 2020. Zircon U-Pb dating of magmatism and mineralizing hydrothermal activity in the Variscan Karkonosze Massif and its eastern metamorphic cover (SW Poland). Minerals, **10**, 787; https://doi.org/10.3390/min10090787

Mikulski, S.Z., Małek, R., Chmielewski, A., Sadłowska, K., Brański, P., Oszczepalski, S., Markowiak, M., 2021. Ocena potencjału złożowego REE w Polsce. Zadanie 4.2; Opracowanie końcowe z realizacji zadania w ramach "Wsparcia działań Głównego Geologa Kraju w zakresie prowadzenia Polityki Surowcowej Państwa" (in Polish). CAG PIG, nr arch. 1958/2021, Warszawa.

Niegisch, M., Kamradt, A., Borg, B., 2020. The upper zone of the Storkwitz Carbonatite – geochemical and mineralogical characterization of the REE-mineralisation in the upper zone of the Storkwitz Carbonatite Complex from drill core SES-1/2012. Landesamt für Umwelt, Landwirtschaft und Geologie, Freiberg, Sachsen, Germany.

Oberc, J., 1961. An outline of the geology ot the Karkonosze-Izera block (Studies on geology of the Sudetic Mountains). Zeszyty Naukowe Uniwersytetu Wrocławskiego, Nauka o Ziemi, 5, ser. B, **8:** 139–170.

Oberc, J., 1972. Sudety i obszary przyległe (in Polish). In: Budowa geologiczna Polski, 4, cz. 2. Wydaw. Geol., Warszawa.

Oberc-Dziedzic, T., 1975. Gneiss enclaves in the Rumburk granite of the eastern part of the Izera Block (in Polish). Acta Universitatis Wratislaviensis, **247:** 165–210.

Oberc-Dziedzic, T., 1988. The development of gneisses and granites of the eastern part of the Izera crystalline in the light of texture studies (in Polish). Acta Universitatis Wratislaviensis, **997**; Prace Geologiczno-Mieneralogiczne, **13**: 1–184.

Oliver, G.J.H., Corfu, F., Krogh, T.E., 1993. U-Pb ages from SW Poland: Evidence for Caledonian suture zone between Baltica and Gondwana. Journal of the Geological Society, **150**: 355–369; https://doi.org/10.1144/gsjgs.150.2.0355

Olson, J.C., Shawe, D.R., Pray, L.C., Sharp, W.N., 1954. Rare-earth mineral deposits of the Mountain Pass district, San Bernadino County, California. Geological Survey Professional Paper, **241:** 75.

Ottaway, T., Wicks, F., Bryndzia, L., Kyser, T.K., Spooner, E.T.C., 1994. Formation of the Muzo hydrothermal emerald deposit in Colombia. Nature, **369:** 552–554; https://doi.org/10.1038/369552a0

Petrik, I., Broska, I., Lipka, J., Siman, P., 1995. Granitoid allanite-(Ce) substitution relations, redox conditions and REE distributions (on an example of I-type granitoids, Western Carpathians, Slovakia). Geologia Carpathica, **46:** 79–94.

Piestrzyński, A., Mochnacka, K., Mayer, W., Kucha, H., 1992. Native gold (electrum), Fe-Co-Ni arsenides and sulphoarsenides in the mica schists from Przecznica, the Kamienica Range, SW Poland. Mineralogica Polonica, **23**: 27–43.

Rasmussen, B., 1996. Early-diagenetic REE-phosphate minerals (florencite, gorceixite, crandallite, and xenotime) in marine sandstones; a major sink for oceanic phosphorus. American Journal of Science, **296:** 601–632; https://doi.org/10.2475/ajs.296.6.601

Repina, S.A., 2010. Zoning and Sectoriality of the Florencite and Xenotime Group Minerals from Quartz Veins, the Subpolar Urals. Geology of Ore Deposits, **52**: 821–836; https://doi.org/10.1134/S1075701510080143

Repina, S.A., Muftakhov, V.A., 2021. The Nature of Oscillatory Zoning and Mechanism of Crystal Growth in a Paragenic Intergrowth of Florencite and Xenotime. Geology of Ore Deposits, **63:** 749–771. https://doi.org/10.1134/S1075701521080079

Siemiątkowski, J., 1986. Poglądy na genezę złóż cyny łupkowego Pasma Kamienieckiego (in Polish). Kwartalnik Geologiczny, **30** (1): 126.

Siemiątkowski, J., 1988. Struktury i tekstury mineralizacji kasyterytowo-siarczkowej zachodniej części pasma kamienieckiego w Górach Izerskich (in Polish). Kwartalnik Geologiczny, **32:** 220–221.

Siemiątkowski, J., 1989. Tekstury warstewkowe kasyterytów z łupków łyszczykowych okolic Czerniawy Zdroju w Górach Izerskich (in Polish). Przegląd Geologiczny, **37**: 430–432.

Smulikowski, W., 1972. Petrographic and structural problems of the northern cover of the Karkonosze granite (in Polish with English summary). Geologica Sudetica, **6:** 97–188.

Smulikowski, W., 1995. Evidence of glaucophane-schist facies metamorphism in the East Karkonosze complex, West Sudetes, Poland. Geologische Rundschau, **84:** 720–737; https://doi.org/10.1007/BF00240563

Speczik, S., Wiszniewska, J., 1984. Some comments about stratiform tin deposits in the Stara Kamienica Chain (southwestern Poland). Mineralium Deposita, **19**: 171–175; https://doi.org/10.1007/BF00199781

Švecová, E., Čopjaková, R., Losos, Z., Škoda, R., Nasdala, L., Cícha, J., 2016. Multi-stage evolution of xenotime-(Y) from Písek pegmatites, Czech Republic: An electron probe micro-analysis and Raman spectroscopy study. Mineralogy and Petrology, **110**: 747–765; https://doi.org/10.1007/s00710-016-0442-6

Szałamacha, M., 1967. About tin mineralization in the eastern part of the Kamieniec range in the Izera Mountains (in Polish with English summary). Przegląd Geologiczny, **15:** 281–284.

Szałamacha, M., 1976. On the origin of cassiterite mineralization in the metamorphic schists of the Karkonosze-Góry Izerskie (Mts.) Block, the Sudetes. In: The Current Metallogenic Problems of Central Europe (ed. J. Fedak): 343–349. Wydaw. Geol., Warszawa.

Szałamacha, M., Szałamacha, J., 1974. Geological and petrographic characteristic of schists mineralized with cassiterite on the basis of materials from the quarry at (in Polish with English summary). Biuletyn Państwowego Instytutu Geologicznego, **279:** 59–89.

Trueman, D.L., Pedersen, J.C., De Jorre, D.T., Smith, D.G.W., 1988. The Thor Lake rare-metal deposits, Northwest Territories. Canadian Institute of Mining, Metallurgy, and Petroleum (Spec. Vol.), **39:** 280–290.

Tuduri, J., Pourret, O., Gloaguen, E., Lach, P., Janots, E., Colin, S., Gouin, J., Chevillard, M., Bailly, L., 2023. Formation of authigenic grey monazite: a palaeo-thermal anomaly marker in very-low grade metamorphic rocks?. Ore Geology Reviews, **160**, 105583; https://doi.org/10.1016/j.oregeorev.2023.105583

Uher, P., Ondrejka, M., Bacík, P., Broska, I., Konecný, P., 2015. Britholite, monazite, REE carbonates, and calcite: products of hydrothermal alteration of allanite and apatite in A-type granite from Stupne, Western Carpathians, Slovakia. Lithos, **236–237**: 212–225; https://doi.org/10.1016/j.lithos.2015.09.005

von Gehlenk, K., Grauert, B., Nielsen, H., 1986. REE minerals in southern Schwarzwald veins and isotope studies on gypsum from central Schwarzwald, FR Germany. Neues Jahrbuch für Mineralogie, Monatshefte, (9): 393–399.

Warr, L.N., 2021. IMA–CNMNC approved mineral symbols. Mineralogical Magazine, **85:** 291–320; https://doi.org/10.1180/mgm.2021.43

Weill, D.F., Drake, M.J., 1973. Europium anomaly in plagioclase feldspar: experimental results and semiquantitative model. Science, **180**: 1059–1060; https://doi.org/10.1126/science.180.4090.1059

Williams-Jones, A., Wood, S.A., 1992. A preliminary petrogenetic grid for REE fluorocarbonates and associated minerals. Geochemica et Cosmochemica Acta, **56:** 725–738; https://doi.org/10.1016/0016-7037(92)90093-X

Winchester, J.A., Floyd, P.A., Chocyk, M., Horbowy, K., Kozdrój, W., 1995. Geochemistry and tectonic environment of Ordovician meta-igneous rocks in the Rudawy Janowickie Complex, SW Poland. Journal of the Geological Society, **152:** 105–115; https://doi.org/10.1144/gsjgs.152.1.010

Winchester, J.A., Patočka, F., Kachlík, V., Melzer, M., Nawakowski, C., Crowley, Q.G., Floyd, P.A., 2003. Geochemical discrimination of metasedimentary sequences in the Karkonose-Jizera Terrane (West Sudetes, Bohemian Massif): paleotectonic and stratigraphic constraints. Geologica Carpathica, **54**: 267–280.

Winkler, H.G.F., 1967. Die Genese der Metamorphen Gesteinei. Springer, Berlin.

Wiszniewska, J., 1983. Origin of tin mineralization of the Izera schists in Kamienieckie Range (Sudetes). Archiwum Mineralogiczne, **38**: 45–55.

Wiszniewska, J., 1984. The genesis of ore-mineralization of the Izera schists in the Kamienieckie Range (Sudetes) (in Polish with English summary). Archiwum Mineralogiczne, **40**: 115–187.

Wu, L.G., Li, X.H., Ling, X.X., Yang, Y.H., Li, C.F., Li, Y.L., Wu, L.G., Li, X.H., Ling, X.X., Yang, Y.H., Li, C.F., Li, Y.L., Mao, Q., Li, Q.L., Putlitz, B., 2019. Further characterization of the RW-1 monazite: a new working reference material for oxygen and neodymium isotopic microanalysis. Minerals, **9**, 583; https://doi.org/10.3390/min9100583

Żaba, J., 1985. Progressive regional metamorphism of the Izera Block, Western Sudetes (Poland). Acta Universitatis Carolinae Geologica, **1**: 63–88.

Žáčková, E., Konopásek, J., Jeřábek, P., Finger, F., Košler, J., 2010. Early Carboniferous blueschist facies metamorphism in metapelites of the West Sudetes (Northern Saxothuringian Domain, Bohemian Massif). Journal of Metamorphic Geology, **28:** 361–379; https://doi.org/10.1111/j.1525-1314.2010.00869.x

Žáčková, E., Konopásek, J., Košler, J., Jeřábek, P., 2012. Detrital zircon populations in quartzites of the Krkonoše-Jizera Massif: implications for pre-collisional history of the Saxothuringian Domain in the Bohemian Massif. Geological Magazine, **149:** 443–458; https://doi.org/10.1017/S0016756811000744

Zhai, M.G., Wu, F.Y., Hu, R.Z., Jiang, S.Y., Li, W.C., Wang, R.C., Wang, D.H., Qi, T., Qin, K.Z., Wen, H.J., 2019. Critical metal mineral resources: current research status and scientific issues. Bulletin of National Natural Science Foundation of China, **33:** 106–1118; https://doi.org/10.16262/j.cnki.1000-8217.2019.02.002

Zygo, W., Foltyn, K., Thomasen, T.B., Heredia, B.D., Piestrzyński, A., 2023. Preliminary results of U-Pb dating and trace element analysis of cassiterites from the Western Sudetes, SW Poland. Proceedings of the 17th SGA Biennial Meeting, 28 August – 1 September 2023, **1**: 331–335.

APPENDIX 1

A – Full allanite-(Ce) WDS results. [wt.%; b.d.l. – below detection limit]

WDS point	Sample point	SiO_2	Al_2O_3	CaO	Fe_2O_3	Ce_2O_3	La_2O_3	Nd_2O_3	Gd_2O_3	Pr_2O_3	Y_2O_3	Sm_2O_3	TiO_2	ThO_2	SrO	Na_2O	MgO	K_2O	SO_3	MnO	Dy_2O_3	Total
1	C-X/46	33.89	21.59	15.85	11.62	6.53	2.64	2.83	0.98	0.84	0.78	0.55	0.14	b.d.l.	0.27	0.02	0.06	b.d.l.	b.d.l.	0.14	0.12	98.84
2	C-X/46	34.06	20.89	17.36	12.12	5.06	2.50	2.09	0.76	0.55	0.52	0.33	0.61	b.d.l.	0.27	0.02	0.06	0.02	b.d.l.	b.d.l.	b.d.l.	97.36
3	C-X/46	33.51	21.44	16.39	12.07	6.37	2.90	2.49	0.79	0.68	0.46	0.45	b.d.l.	b.d.l.	0.15	b.d.l.	0.04	b.d.l.	b.d.l.	0.14	b.d.l.	98.06
4	C-X/46	33.90	21.90	14.53	13.07	6.77	2.94	2.65	0.94	0.89	0.27	0.31	0.19	b.d.l.	0.15	0.02	0.35	b.d.l.	0.05	0.12	b.d.l.	99.09
5	C-X/46	34.58	21.36	18.00	12.38	4.46	3.12	1.41	0.55	0.42	0.48	b.d.l.	0.27	b.d.l.	0.42	b.d.l.	0.07	b.d.l.	b.d.l.	0.11	0.09	98.02
6	C-X/46	31.88	21.09	14.86	13.53	6.20	2.88	2.30	0.83	0.64	0.57	0.34	0.30	0.07	0.16	0.02	0.48	b.d.l.	0.09	0.15	b.d.l.	96.44
7	C-X/46	33.38	21.65	16.35	11.88	6.53	3.21	2.34	0.93	0.64	0.37	0.37	0.11	b.d.l.	0.20	b.d.l.	0.04	b.d.l.	b.d.l.	0.14	b.d.l.	98.16
8	C-X/46	33.25	21.65	16.52	11.59	5.67	2.68	2.40	0.78	0.73	0.89	0.46	b.d.l.	b.d.l.	0.24	b.d.l.	0.06	b.d.l.	b.d.l.	0.13	0.13	97.29
9	C-X/46	32.88	21.49	14.77	11.59	7.38	3.93	2.61	0.99	0.84	0.47	0.43	0.15	b.d.l.	0.21	b.d.l.	0.07	b.d.l.	b.d.l.	0.19	b.d.l.	98.05
10	C-X/46	32.79	20.99	13.54	11.56	9.73	4.32	3.11	1.18	0.94	0.29	0.34	0.28	b.d.l.	0.15	0.04	0.10	0.03	b.d.l.	0.14	b.d.l.	99.58
11	C-X/46	32.89	20.84	15.03	11.70	7.83	3.69	3.19	1.20	0.83	0.29	0.45	0.22	b.d.l.	0.17	b.d.l.	0.07	b.d.l.	b.d.l.	b.d.l.	0.18	98.68
12	C-X/46	32.86	20.15	15.80	11.53	6.95	3.10	2.85	0.87	0.82	0.33	b.d.l.	1.08	b.d.l.	0.13	b.d.l.	0.06	b.d.l.	b.d.l.	b.d.l.	b.d.l.	96.72
13	G-I/13	31.75	19.35	11.46	11.88	10.73	4.75	4.53	1.34	1.20	0.33	0.88	0.11	0.22	0.26	0.08	0.09	0.04	b.d.l.	0.40	b.d.l.	99.44
14	G-I/13	31.57	19.39	10.99	11.75	9.67	4.66	4.01	1.27	1.05	0.33	0.54	0.38	0.39	0.24	0.14	0.26	0.10	b.d.l.	0.36	b.d.l.	97.14
15	G-I/13	31.48	18.72	11.07	11.55	10.00	4.63	3.69	1.25	0.99	0.41	0.34	0.87	0.57	0.14	0.12	0.11	0.17	0.05	0.34	b.d.l.	96.59
16	G-I/13	32.27	20.48	12.23	11.07	9.19	4.86	3.55	1.24	0.90	0.50	0.60	b.d.l..	0.12	0.36	0.08	0.14	0.06	b.d.l.	0.42	b.d.l.	98.18
17	G-I/13	31.94	19.44	11.68	12.28	9.49	5.25	4.43	1.32	1.03	0.29	0.65	0.15	b.d.l.	0.21	0.04	0.11	b.d.l.	b.d.l.	0.38	b.d.l.	98.81
18	G-I/13	32.07	19.92	11.60	12.00	10.42	4.67	4.24	1.29	0.95	0.28	0.63	b.d.l.	b.d.l.	0.19	0.10	0.14	0.02	b.d.l.	0.49	b.d.l.	99.18
19	G-I/13	33.15	20.94	11.77	11.63	8.60	4.31	4.39	1.18	1.04	0.41	0.62	0.12	0.10	0.23	0.05	0.18	0.43	0.17	0.42	b.d.l.	99.73
20	G-I/13	32.14	20.08	11.96	11.23	9.69	4.54	4.09	1.38	1.17	0.34	0.65	b.d.l.	b.d.l.	0.32	0.08	0.08	0.03	b.d.l.	0.43	b.d.l.	98.36
21	G-I/13	31.83	19.58	11.40	11.77	10.25	4.76	4.48	1.33	1.17	0.34	0.67	0.22	b.d.l.	0.24	0.07	0.08	0.04	b.d.l.	0.43	b.d.l.	98.74
22	G-I/13	32.03	20.47	11.64	14.36	7.40	3.44	2.81	0.58	0.90	0.90	0.60	b.d.l.	0.10	0.22	0.05	1.26	0.09	0.05	0.33	0.23	97.55
23	G-I/13	31.79	19.91	11.90	12.62	9.65	4.51	2.46	b.d.l..	0.78	0.43	0.28	0.14	0.11	0.22	0.06	0.50	0.06	b.d.l.	0.33	0.10	95.86
24	G-I/13	31.66	19.31	11.16	12.99	11.06	5.47	4.56	1.52	1.24	0.24	0.69	b.d.l.	0.11	0.22	0.08	0.10	0.02	b.d.l.	0.41	b.d.l.	100.92
25	K-II/3	32.75	21.24	13.57	10.12	8.76	4.88	3.25	0.34	0.88	0.76	0.41	0.49	b.d.l.	0.13	0.03	0.05	b.d.l.	b.d.l.	0.21	0.12	98.02
26	K-II/3	32.51	20.25	12.68	11.08	9.57	4.83	3.35	0.30	0.97	0.74	0.38	0.69	b.d.l.	b.d.l.	0.03	0.08	b.d.l.	b.d.l.	0.20	b.d.l.	97.84

27	K-II/3	32.14	20.16	12.37	11.48	9.50	4.24	4.11	0.30	1.10	1.02	0.50	0.15	0.13	0.09	0.04	0.04	b.d.l.	b.d.l.	0.28	0.11	97.77
28	K-II/3	32.24	20.39	12.28	10.93	8.83	4.46	3.98	0.49	1.01	1.25	0.67	0.13	b.d.l.	0.12	0.05	0.04	0.02	b.d.l.	0.40	0.11	97.42
29	K-II/3	32.46	20.74	12.75	11.21	8.89	4.38	3.72	0.39	1.08	1.18	0.61	0.18	0.07	0.13	0.04	0.05	b.d.l.	b.d.l.	0.27	0.13	98.30
30	K-II/3	32.00	21.33	13.47	11.35	9.13	5.27	3.37	0.28	0.89	0.41	0.44	b.d.l.	b.d.l.	0.18	0.02	0.02	b.d.l.	b.d.l.	0.14	b.d.l.	98.50
31	K-II/3	31.88	20.39	12.59	11.30	10.03	4.95	3.58	0.28	1.01	0.67	0.55	0.21	0.07	b.d.l.	0.05	0.03	b.d.l.	b.d.l.	0.17	b.d.l.	97.80
32	K-II/3	32.66	20.73	13.25	11.18	8.40	4.22	3.58	0.37	0.98	1.07	0.58	b.d.l.	b.d.l.	0.11	0.02	0.03	0.04	b.d.l.	0.29	b.d.l.	97.72
33	G-III/17	32.79	20.39	12.18	11.79	9.76	4.50	3.99	1.31	1.16	0.50	0.77	0.27	0.27	0.33	0.06	0.12	0.03	0.37	0.31	b.d.l.	100.90
34	G-III/17	28.19	15.92	9.48	22.24	8.39	4.47	3.78	1.49	0.93	0.98	0.65	0.47	0.75	b.d.l.	0.10	0.06	0.03	0.59	0.09	0.17	98.87
35	G-III/17	24.42	14.59	7.60	31.71	6.27	3.18	3.09	1.05	0.59	0.87	0.51	0.20	1.16	0.10	0.12	0.03	0.04	2.18	0.09	0.20	98.01
36	G-III/17	31.90	20.43	12.20	11.12	9.53	5.13	3.31	1.27	0.91	0.46	0.46	b.d.l.	0.24	0.24	0.06	0.15	b.d.l.	b.d.l.	0.30	0.18	97.98
37	G-III/17	31.64	20.56	12.28	11.48	9.34	5.20	3.46	1.29	1.17	0.45	0.40	0.11	0.23	0.38	0.10	0.10	b.d.l.	0.05	0.30	0.13	98.71
38	G-III/17	31.10	17.80	9.79	13.52	12.46	6.34	5.03	1.60	1.28	b.d.l.	1.00	0.14	b.d.l.	b.d.l.	0.03	b.d.l.	0.02	0.06	0.13	b.d.l.	100.35
39	G-III/17	30.07	19.24	11.80	12.27	9.68	4.60	4.14	1.38	1.02	0.23	0.61	b.d.l.	b.d.l.	0.12	0.03	0.05	b.d.l.	0.10	0.27	b.d.l.	95.65
40	G-III/17	29.25	18.94	11.99	11.79	9.93	4.67	4.19	1.38	0.92	0.24	0.73	b.d.l.	b.d.l.	b.d.l.	0.03	0.05	b.d.l.	1.55	0.14	b.d.l.	95.89
avr. det. lim.		**0.06**	**0.04**	**0.03**	**0.07**	**0.19**	**0.21**	**0.29**	**0.16**	**0.26**	**0.09**	**0.27**	**0.11**	**0.07**	**0.08**	**0.02**	**0.01**	**0.02**	**0.05**	**0.08**	**0.09**	**-**

	SiO_2	Al_2O_3	CaO	Fe_2O_3	Ce_2O_3	La_2O_3	Nd_2O_3	Gd_2O_3	Pr_2O_3	Y_2O_3	Sm_2O_3	TiO_2	ThO_2	SrO	Na_2O	MgO	K_2O	SO_3	MnO	Dy_2O_3	Total
minimum	24.42	14.59	7.60	10.12	4.46	2.50	1.41	b.d.l.	0.42	b.d.l.	0.17	b.d.l.	b.d.l.	b.d.l.	b.d.l.	b.d.l.	b.d.l.	b.d.l.	b.d.l.	b.d.l.	95.65
maximum	34.58	21.90	18.00	31.71	12.46	6.34	5.03	1.60	1.28	1.25	1.00	1.08	1.16	0.42	0.14	1.26	0.43	2.18	0.49	0.23	100.92
arithmetic mean	32.04	20.14	12.95	12.61	8.60	4.23	3.44	0.95	0.93	0.53	0.52	0.23	0.13	0.19	0.05	0.14	0.04	0.14	0.24	0.06	98.16
median	32.14	20.41	12.28	11.73	9.16	4.49	3.50	1.02	0.94	0.45	0.53	0.14	0.04	0.18	0.04	0.07	0.01	0.02	0.24	0.04	98.05
standard deviation	1.70	1.44	2.19	3.55	1.75	0.90	0.81	0.43	0.19	0.29	0.17	0.23	0.23	0.09	0.04	0.21	0.07	0.41	0.13	0.07	1.21

B – Atoms per formula unit (apfu) calculations in allanite-(Ce). [the formulae were calculated to 12.5 oxygen and 8 cations]

WDS point	1	2	3	4	5	6	7	8	9	10	11	12	13	14	15	16	17	18	19	20	21	22	23	24	25	26	27	28	29	30	31	32	33	34	35	36	37	38	39	40
Sample point	C-X/46	C-X/46	C-X/46	C-X/46	C-X/46	C-X/46	C-X/46	C-X/46	C-X/46	C-X/46	C-X/46	C-X/46	G-I/13	G-I/13	G-I/13	G-I/13	G-I/13	G-I/13	G-I/13	G-I/13	G-I/13	G-I/13	G-I/13	G-I/13	K-II/3	K-II/3	K-II/3	K-II/3	K-II/3	K-II/3	K-II/3	K-II/3	G-III/17	G-III/17	G-III/17	G-III/17	G-III/17	G-III/17	G-III/17	G-III/17
Si	3.53	3.53	3.50	3.48	3.54	3.37	3.48	3.49	3.48	3.48	3.49	3.50	3.47	3.49	3.51	3.51	3.48	3.48	3.53	3.51	3.48	3.38	3.47	3.42	3.53	3.52	3.50	3.52	3.50	3.44	3.48	3.52	3.50	3.02	2.57	3.49	3.44	3.43	3.39	3.36
Ti	0.01	0.05	0.01	0.01	0.02	0.02	0.01	0.01	0.01	0.02	0.02	0.09	0.01	0.03	0.07	0.01	0.01	0.01	0.01	0.01	0.02	0.01	0.01	0.01	0.04	0.06	0.01	0.01	0.01	0.01	0.02	0.01	0.02	0.04	0.02	0.01	0.01	0.01	0.00	0.00
Al	1.99	1.92	1.98	1.99	1.93	1.97	2.00	2.01	2.01	1.97	1.95	1.90	1.87	1.90	1.85	1.97	1.87	1.91	1.97	1.94	1.89	1.91	1.92	1.84	2.02	1.94	1.94	1.97	1.98	2.03	1.96	1.97	1.92	1.51	1.36	1.98	1.98	1.74	1.92	1.92
Fe^{2+}	0.68	0.71	0.71	0.76	0.72	0.81	0.70	0.69	0.69	0.69	0.70	0.69	0.73	0.73	0.73	0.68	0.75	0.73	0.70	0.69	0.73	0.86	0.78	0.79	0.62	0.68	0.71	0.67	0.68	0.69	0.69	0.68	0.71	1.35	1.88	0.69	0.71	0.84	0.78	0.76
Fe^{3+}	0.45	0.47	0.47	0.51	0.48	0.53	0.46	0.45	0.45	0.45	0.46	0.45	0.46	0.46	0.45	0.43	0.48	0.47	0.46	0.44	0.46	0.56	0.49	0.51	0.40	0.43	0.45	0.43	0.44	0.44	0.44	0.44	0.46	0.87	1.24	0.44	0.45	0.53	0.48	0.46
Mg	0.00	0.00	0.00	0.03	0.01	0.04	0.00	0.00	0.01	0.01	0.01	0.01	0.01	0.02	0.01	0.01	0.01	0.01	0.01	0.01	0.01	0.10	0.04	0.01	0.00	0.01	0.00	0.00	0.00	0.00	0.00	0.00	0.01	0.01	0.00	0.01	0.01	0.00	0.00	0.00
Ca	0.88	0.96	0.92	0.80	0.99	0.84	0.91	0.93	0.84	0.77	0.85	0.90	0.67	0.65	0.66	0.71	0.68	0.67	0.67	0.70	0.67	0.66	0.69	0.65	0.78	0.74	0.72	0.72	0.74	0.78	0.73	0.76	0.70	0.54	0.43	0.71	0.72	0.58	0.71	0.74
La	0.08	0.07	0.08	0.08	0.09	0.08	0.09	0.08	0.12	0.13	0.11	0.09	0.14	0.14	0.14	0.15	0.16	0.14	0.13	0.14	0.14	0.10	0.14	0.16	0.15	0.14	0.13	0.13	0.13	0.16	0.15	0.13	0.13	0.13	0.09	0.16	0.16	0.19	0.14	0.15
Ce	0.19	0.14	0.18	0.19	0.13	0.18	0.19	0.16	0.21	0.28	0.23	0.20	0.32	0.29	0.31	0.27	0.28	0.31	0.25	0.29	0.31	0.21	0.29	0.33	0.26	0.28	0.28	0.26	0.26	0.27	0.30	0.25	0.29	0.25	0.18	0.29	0.28	0.38	0.30	0.31
Pr	0.02	0.02	0.02	0.02	0.01	0.02	0.02	0.02	0.02	0.03	0.02	0.02	0.04	0.03	0.03	0.03	0.03	0.03	0.03	0.03	0.04	0.03	0.02	0.04	0.03	0.03	0.03	0.03	0.03	0.03	0.03	0.03	0.03	0.03	0.02	0.03	0.03	0.04	0.03	0.03
Nd	0.08	0.06	0.07	0.07	0.04	0.07	0.07	0.07	0.07	0.09	0.09	0.08	0.13	0.12	0.11	0.10	0.13	0.12	0.13	0.12	0.13	0.08	0.07	0.13	0.09	0.10	0.12	0.12	0.11	0.10	0.10	0.10	0.11	0.11	0.09	0.10	0.10	0.15	0.12	0.13
Sm	0.01	0.01	0.01	0.01	0.01	0.01	0.01	0.01	0.01	0.01	0.01	0.00	0.02	0.02	0.01	0.02	0.02	0.02	0.02	0.02	0.02	0.02	0.01	0.02	0.01	0.01	0.01	0.02	0.02	0.01	0.02	0.02	0.02	0.02	0.01	0.01	0.01	0.03	0.02	0.02
Gd	0.03	0.02	0.02	0.02	0.01	0.02	0.02	0.02	0.03	0.03	0.03	0.02	0.04	0.03	0.03	0.03	0.04	0.03	0.03	0.04	0.04	0.02	0.00	0.04	0.01	0.01	0.01	0.01	0.01	0.01	0.01	0.01	0.03	0.04	0.03	0.03	0.03	0.04	0.04	0.04
Th	0.00	0.00	0.00	0.00	0.00	0.00	0.00	0.00	0.00	0.00	0.00	0.00	0.01	0.01	0.01	0.00	0.00	0.00	0.00	0.00	0.00	0.00	0.00	0.00	0.00	0.00	0.00	0.00	0.00	0.00	0.00	0.00	0.01	0.02	0.03	0.01	0.01	0.00	0.00	0.00
Mn	0.01	0.00	0.01	0.01	0.00	0.01	0.01	0.01	0.01	0.01	0.00	0.00	0.02	0.02	0.02	0.02	0.02	0.02	0.02	0.02	0.02	0.01	0.02	0.02	0.01	0.01	0.01	0.02	0.01	0.01	0.01	0.01	0.01	0.00	0.00	0.01	0.01	0.01	0.01	0.01
Sr	0.01	0.01	0.00	0.00	0.01	0.01	0.01	0.01	0.01	0.00	0.01	0.00	0.01	0.01	0.00	0.01	0.01	0.01	0.01	0.01	0.01	0.01	0.01	0.01	0.00	0.00	0.00	0.00	0.00	0.01	0.00	0.00	0.01	0.00	0.00	0.01	0.01	0.00	0.00	0.00
Y	0.03	0.02	0.02	0.01	0.02	0.02	0.02	0.04	0.02	0.01	0.01	0.01	0.01	0.01	0.02	0.02	0.01	0.01	0.02	0.01	0.01	0.04	0.02	0.01	0.03	0.03	0.04	0.05	0.05	0.02	0.03	0.05	0.02	0.04	0.04	0.02	0.02	0.00	0.01	0.01
Total	8.00	8.00	8.00	8.01	8.01	7.99	8.00	8.00	7.99	7.99	7.99	7.99	7.98	7.97	7.97	7.98	7.98	7.98	7.99	7.98	7.98	7.99	7.97	7.98	7.99	7.98	7.98	7.98	7.98	7.99	7.98	7.98	7.99	7.97	7.99	7.98	7.98	7.97	7.96	7.95
REE+Th	0.41	0.32	0.39	0.41	0.28	0.38	0.40	0.36	0.47	0.57	0.49	0.43	0.70	0.65	0.65	0.60	0.66	0.66	0.59	0.64	0.67	0.46	0.53	0.72	0.55	0.58	0.59	0.58	0.56	0.57	0.61	0.53	0.63	0.59	0.45	0.62	0.62	0.83	0.66	0.68

C – Full monazite-(Ce) WDS results. [wt.%; b.d.l. – below detection limit]

WDS point	Sample point	Ce_2O_3	P_2O_5	La_2O_3	Nd_2O_3	ThO_2	Pr_2O_3	CaO	PbO_2	Sm_2O_3	Y_2O_3	Gd_2O_3	Fe_2O_3	Dy_2O_3	Eu_2O_3	UO_2	SrO	SiO_2	Al_2O_3	SO_3	K_2O	As_2O_3	Total
1	St. Leopold mine	28.03	29.69	13.09	10.93	b.d.l.	3.08	3.74	0.84	2.10	2.81	1.62	0.71	0.80	0.49	0.13	0.13	0.07	0.05	0.16	0.07	b.d.l.	98.55
2	St. Leopold mine	27.13	30.14	12.78	10.88	b.d.l.	2.77	4.11	3.85	1.97	2.09	1.39	0.67	0.63	0.47	0.18	0.12	0.09	0.24	0.53	0.04	0.09	100.17
3	St. Leopold mine	29.18	30.08	13.53	11.76	b.d.l.	3.13	3.58	0.48	1.88	2.37	1.39	0.51	0.75	0.60	0.14	0.10	0.27	0.09	0.23	0.09	b.d.l.	100.19
4	St. Leopold mine	28.80	29.36	12.49	11.58	0.08	2.99	3.67	2.25	2.06	1.66	1.24	0.45	0.51	0.35	0.29	0.08	0.18	0.10	0.31	0.02	0.04	98.53

5	St. Leopold mine	25.96	30.40	10.12	11.76	2.43	2.92	3.80	b.d.l.	2.35	2.14	1.40	0.81	0.72	0.55	0.57	0.08	0.13	0.04	0.14	0.08	b.d.l.	96.41
6	St. Leopold mine	20.44	28.96	8.59	8.26	16.36	2.10	5.18	b.d.l.	1.43	1.40	0.94	1.11	0.41	0.27	0.36	0.15	0.48	0.14	0.14	0.11	b.d.l.	96.85
7	St. Leopold mine	27.67	30.54	12.71	10.57	b.d.l.	2.53	4.09	2.72	1.70	2.12	1.48	0.59	0.56	0.34	0.34	0.11	0.12	0.14	0.29	0.05	0.12	98.84
8	St. Leopold mine	27.98	30.01	13.94	10.95	b.d.l.	2.59	3.89	2.13	1.66	1.92	1.24	0.47	0.51	0.36	0.26	0.10	0.16	0.08	0.26	0.03	b.d.l.	98.55
9	St. Leopold mine	28.38	30.14	13.64	11.58	b.d.l.	2.76	3.67	1.00	1.74	2.14	1.41	0.66	0.63	0.30	0.14	0.08	0.18	0.07	0.20	0.06	b.d.l.	98.77
10	St. Leopold mine	28.35	30.54	14.06	10.68	b.d.l.	2.66	4.23	2.11	1.66	1.79	1.22	1.00	0.44	0.38	0.16	0.10	0.20	0.08	0.33	0.12	b.d.l.	100.12
11	St. Leopold mine	28.01	31.23	14.30	10.42	b.d.l.	2.90	4.38	1.01	1.60	2.07	1.43	1.13	0.52	0.34	0.23	0.11	0.12	0.02	0.11	0.07	b.d.l.	99.99
12	St. Leopold mine	28.58	28.99	10.90	11.53	b.d.l.	2.96	4.09	2.98	2.09	1.22	1.14	1.68	0.50	0.42	0.81	0.09	0.49	0.28	0.61	0.07	0.07	99.50
13	St. Leopold mine	25.36	30.46	11.19	9.36	5.22	2.43	3.95	5.01	1.66	1.37	1.00	0.88	0.50	0.34	0.40	0.17	0.21	0.29	0.82	0.11	0.19	100.91
14	St. Leopold mine	25.79	28.67	11.16	9.80	b.d.l.	2.75	3.55	6.60	1.76	1.70	1.05	1.76	0.59	0.33	0.60	0.14	0.43	0.57	0.94	0.06	0.34	98.66
15	St. Leopold mine	24.02	30.10	10.55	8.75	7.63	2.32	4.22	4.99	1.42	1.10	0.84	0.46	0.37	0.32	0.29	0.16	0.27	0.33	0.84	0.19	0.13	99.31
16	St. Leopold mine	26.82	28.00	12.19	10.11	0.50	2.54	3.57	5.48	1.76	2.20	1.18	0.42	0.70	0.41	0.04	0.13	0.91	0.68	0.94	0.20	0.17	98.97
17	G-VI/22	25.32	26.31	12.75	9.94	12.88	2.56	1.52	0.26	1.86	0.18	0.87	1.45	0.11	0.32	0.24	b.d.l.	1.63	0.03	0.98	b.d.l.	b.d.l.	99.28
18	G-VI/22	26.45	27.61	13.40	10.32	10.54	2.71	1.50	0.19	1.89	0.28	1.02	0.54	0.11	0.26	0.28	b.d.l.	1.02	b.d.l.	0.03	0.02	b.d.l.	98.22
19	G-VI/22	27.25	28.29	14.11	10.14	10.70	2.80	1.51	0.15	1.84	b.d.l.	0.53	0.18	b.d.l.	0.27	0.29	0.05	1.01	b.d.l.	0.04	0.04	b.d.l.	99.22
20	G-VI/22	28.22	28.82	14.66	10.91	8.83	2.83	1.35	0.13	1.65	b.d.l.	0.72	0.20	b.d.l.	b.d.l.	0.26	b.d.l.	0.70	0.03	b.d.l.	0.04	b.d.l.	99.47
21	G-VI/22	27.29	28.59	14.48	10.23	10.10	2.80	1.49	0.16	1.67	b.d.l.	0.64	0.29	b.d.l.	0.22	0.24	0.07	0.90	0.05	b.d.l.	0.03	b.d.l.	99.33
22	G-VI/22	29.43	29.43	15.49	10.43	7.16	2.90	1.19	0.08	1.56	0.12	0.78	0.36	b.d.l.	b.d.l.	0.33	b.d.l.	0.59	b.d.l.	b.d.l.	0.04	0.03	100.10
23	G-VI/22	30.56	29.97	16.31	10.60	5.00	2.97	0.91	0.09	1.71	0.10	0.80	0.57	b.d.l.	b.d.l.	0.38	0.05	0.42	0.05	b.d.l.	0.06	b.d.l.	100.75
avr. det. lim.		**0.17**	**0.02**	**0.16**	**0.24**	**0.07**	**0.21**	**0.02**	**0.05**	**0.22**	**0.05**	**0.18**	**0.06**	**0.11**	**0.21**	**0.04**	**0.05**	**0.02**	**0.02**	**0.03**	**0.02**	**0.02**	**-**

	Ce_2O_3	P_2O_5	La_2O_3	Nd_2O_3	ThO_2	Pr_2O_3	CaO	PbO_2	Sm_2O_3	Y_2O_3	Gd_2O_3	Fe_2O_3	Dy_2O_3	Eu_2O_3	UO_2	SrO	SiO_2	Al_2O_3	SO_3	K_2O	As_2O_3	**Total**
minimum	20.44	26.31	8.59	8.26	0.00	2.10	0.91	b.d.l.	1.42	b.d.l.	0.53	0.18	b.d.l.	b.d.l.	0.04	b.d.l.	0.07	b.d.l.	b.d.l.	b.d.l.	b.d.l.	96.41
maximum	30.56	31.23	16.31	11.76	16.36	3.13	5.18	6.60	2.35	2.81	1.62	1.76	0.80	0.60	0.81	0.17	1.63	0.68	0.98	0.20	0.34	100.91
arithmetic mean	27.17	29.41	12.89	10.50	4.24	2.74	3.18	1.85	1.78	1.34	1.10	0.74	0.41	0.34	0.30	0.09	0.46	0.15	0.35	0.07	0.05	99.16
median	27.67	29.69	13.09	10.57	0.50	2.77	3.67	1.00	1.74	1.66	1.14	0.59	0.50	0.34	0.28	0.10	0.27	0.08	0.23	0.06	0.00	99.28
standard deviation	2.06	1.12	1.79	0.88	5.08	0.24	1.26	2.01	0.22	0.90	0.29	0.43	0.26	0.12	0.17	0.04	0.39	0.17	0.33	0.05	0.09	1.06

D – Atoms per formula unit (apfu) calculations in monazite-(Ce). [the formulae were calculated to 4 oxygen and 2 cations]

WDS point	1	2	3	4	5	6	7	8	9	10	11	12	13	14	15	16	17	18	19	20	21	22	23
Sample point	St. Leopold mine	St. Leopold mine	St. Leopold mine	St. Leopold mine	St. Leopold mine	St. Leopold mine	St. Leopold mine	St. Leopold mine	St. Leopold mine	St. Leopold mine	St. Leopold mine	St. Leopold mine	St. Leopold mine	St. Leopold mine	St. Leopold mine	St. Leopold mine	G-VI/22	G-VI/23	G-VI/24	G-VI/25	G-VI/26	G-VI/27	G-VI/28
Ce	0.30	0.28	0.31	0.31	0.28	0.22	0.29	0.30	0.30	0.29	0.29	0.30	0.26	0.27	0.25	0.28	0.28	0.30	0.30	0.31	0.30	0.32	0.33
P	1.22	1.21	1.21	1.21	1.25	1.21	1.23	1.22	1.22	1.22	1.24	1.17	1.21	1.16	1.21	1.14	1.12	1.19	1.20	1.22	1.21	1.23	1.24
La	0.14	0.13	0.14	0.13	0.11	0.09	0.13	0.15	0.14	0.15	0.15	0.12	0.12	0.12	0.11	0.13	0.14	0.15	0.16	0.16	0.16	0.17	0.18
Nd	0.11	0.11	0.12	0.12	0.12	0.09	0.11	0.11	0.12	0.11	0.10	0.12	0.09	0.10	0.09	0.10	0.11	0.11	0.11	0.12	0.11	0.11	0.11
Th	0.00	0.00	0.00	0.00	0.02	0.15	0.00	0.00	0.00	0.00	0.00	0.00	0.04	0.00	0.07	0.00	0.12	0.10	0.10	0.08	0.09	0.06	0.04
Pr	0.02	0.02	0.02	0.02	0.02	0.02	0.02	0.02	0.02	0.02	0.02	0.02	0.02	0.02	0.02	0.02	0.02	0.02	0.02	0.02	0.02	0.02	0.02
Ca	0.08	0.08	0.07	0.08	0.08	0.11	0.08	0.08	0.08	0.09	0.09	0.08	0.08	0.07	0.09	0.07	0.03	0.03	0.03	0.03	0.03	0.03	0.02
Pb	0.01	0.04	0.00	0.02	0.00	0.00	0.03	0.02	0.01	0.02	0.01	0.03	0.05	0.06	0.05	0.05	0.00	0.00	0.00	0.00	0.00	0.00	0.00
Sm	0.02	0.02	0.02	0.02	0.02	0.01	0.02	0.02	0.02	0.02	0.02	0.02	0.02	0.02	0.01	0.02	0.02	0.02	0.02	0.02	0.02	0.02	0.02
Y	0.04	0.03	0.04	0.03	0.03	0.02	0.03	0.03	0.03	0.03	0.03	0.02	0.02	0.03	0.02	0.03	0.00	0.00	0.00	0.00	0.00	0.00	0.00
Gd	0.02	0.01	0.01	0.01	0.01	0.01	0.01	0.01	0.01	0.01	0.01	0.01	0.01	0.01	0.01	0.01	0.01	0.01	0.01	0.01	0.01	0.01	0.01
Fe^{3+}	0.02	0.01	0.01	0.01	0.02	0.02	0.01	0.01	0.01	0.02	0.02	0.04	0.02	0.04	0.01	0.01	0.03	0.01	0.00	0.00	0.01	0.01	0.01
Dy	0.01	0.01	0.01	0.00	0.01	0.00	0.01	0.00	0.01	0.00	0.00	0.00	0.00	0.01	0.00	0.01	0.00	0.00	0.00	0.00	0.00	0.00	0.00
Eu	0.00	0.00	0.01	0.00	0.01	0.00	0.00	0.00	0.00	0.00	0.00	0.00	0.00	0.00	0.00	0.00	0.00	0.00	0.00	0.00	0.00	0.00	0.00
U	0.00	0.00	0.00	0.00	0.00	0.00	0.00	0.00	0.00	0.00	0.00	0.01	0.00	0.01	0.00	0.00	0.00	0.00	0.00	0.00	0.00	0.00	0.00
Sr	0.00	0.00	0.00	0.00	0.00	0.00	0.00	0.00	0.00	0.00	0.00	0.00	0.00	0.00	0.00	0.00	0.00	0.00	0.00	0.00	0.00	0.00	0.00
Si	0.00	0.00	0.01	0.01	0.00	0.02	0.00	0.01	0.01	0.01	0.00	0.02	0.01	0.02	0.01	0.04	0.07	0.04	0.04	0.03	0.04	0.02	0.02
Al	0.00	0.01	0.00	0.00	0.00	0.00	0.00	0.00	0.00	0.00	0.00	0.01	0.01	0.02	0.01	0.02	0.00	0.00	0.00	0.00	0.00	0.00	0.00
S	0.01	0.02	0.01	0.01	0.01	0.01	0.01	0.01	0.01	0.01	0.00	0.03	0.03	0.04	0.04	0.04	0.04	0.00	0.00	0.00	0.00	0.00	0.00
K	0.00	0.00	0.00	0.00	0.00	0.00	0.00	0.00	0.00	0.00	0.00	0.00	0.00	0.00	0.00	0.00	0.00	0.00	0.00	0.00	0.00	0.00	0.00
As	0.00	0.00	0.00	0.00	0.00	0.00	0.00	0.00	0.00	0.00	0.00	0.00	0.00	0.01	0.00	0.00	0.00	0.00	0.00	0.00	0.00	0.00	0.00
Total	2.00	2.00	2.00	2.00	2.00	2.00	2.00	2.00	2.00	2.00	2.00	2.00	2.00	2.00	2.00	2.00	2.00	2.00	2.00	2.00	2.00	2.00	2.00
REE+Y	0.67	0.62	0.67	0.65	0.61	0.47	0.62	0.64	0.65	0.63	0.63	0.61	0.54	0.57	0.51	0.61	0.58	0.62	0.61	0.63	0.62	0.65	0.66

E – Full xenotime-(Y) WDS results. [wt.%; b.d.l. – below detection limit]

WDS point	Sample point	Y_2O_3	P_2O_5	Dy_2O_3	Er_2O_3	Gd_2O_3	Yb_2O_3	Ho_2O_3	FeO	Fe_2O_3	UO_2	Tb_2O_3	Lu_2O_3	Sm_2O_3	Tm_2O_3	Eu_2O_3	Nd_2O_3	PbO	SiO_2	CaO	ThO_2	Total
1	K-II/3	45.51	35.15	5.89	4.18	1.14	3.28	1.36	0.70	0.78	0.91	0.41	0.48	b.d.l.	0.25	0.18	b.d.l.	0.04	0.30	b.d.l.	b.d.l.	99.97
2	K-II/3	44.84	34.59	5.29	4.20	1.03	3.49	1.30	0.78	0.87	1.95	0.34	0.60	0.09	0.39	0.20	b.d.l.	0.09	0.68	0.02	b.d.l.	100.07
3	K-II/3	38.37	34.12	9.60	2.93	5.83	1.78	1.43	1.15	1.28	0.76	1.29	0.67	1.06	0.30	0.83	0.37	0.03	0.25	0.03	0.02	100.99
4	K-II/3	38.32	34.44	9.90	2.98	5.60	1.73	1.32	1.00	1.11	0.79	1.34	0.52	1.03	0.26	0.82	0.63	0.05	0.24	b.d.l.	0.01	101.14
5	K-II/3	36.43	33.31	7.57	3.44	5.30	2.89	1.26	1.23	1.37	0.96	1.02	0.70	1.11	0.27	0.54	0.24	0.05	0.39	0.04	0.01	96.97
6	K-II/3	36.82	34.02	7.79	3.43	6.28	2.96	1.24	1.30	1.45	0.78	1.10	0.58	1.48	0.26	0.63	0.26	0.04	0.28	0.04	0.01	99.50
7	K-II/3	41.71	35.05	7.52	4.03	2.88	3.51	1.38	1.07	1.19	0.50	0.81	0.71	0.27	0.30	0.26	b.d.l.	0.02	0.27	b.d.l.	b.d.l.	100.51
8	K-II/3	39.25	34.69	7.05	3.87	5.07	3.09	1.31	1.43	1.58	0.43	0.94	0.71	0.70	0.32	0.34	b.d.l.	0.02	0.33	b.d.l.	0.02	99.90
9	K-II/3	41.41	34.30	6.74	3.96	2.27	3.29	1.16	1.19	1.32	2.12	0.67	0.76	0.18	0.27	0.15	b.d.l.	0.10	0.64	0.02	0.01	99.38
10	K-II/3	41.66	34.99	7.04	3.89	2.60	3.20	1.35	1.41	1.57	0.65	0.72	0.79	0.20	0.32	0.18	b.d.l.	0.02	0.27	0.02	b.d.l.	99.59
11	K-II/3	41.94	34.86	7.07	3.88	2.40	3.46	1.33	1.22	1.36	0.79	0.72	0.71	0.15	0.29	0.16	b.d.l.	0.04	0.39	0.03	b.d.l.	99.59
12	K-II/3	42.68	35.02	6.70	4.13	1.89	3.49	1.33	0.99	1.10	1.05	0.64	0.66	0.14	0.39	0.13	b.d.l.	0.05	0.31	0.02	b.d.l.	99.83
13	K-II/3	41.83	34.59	6.97	3.85	2.37	3.37	1.18	1.27	1.41	1.14	0.74	0.73	0.16	0.31	0.17	b.d.l.	0.05	0.43	0.02	b.d.l.	99.50
14	K-II/3	39.51	34.21	6.59	4.41	3.55	3.22	1.38	1.72	1.91	0.70	0.64	0.59	0.84	0.45	0.57	0.31	0.03	0.26	0.04	0.01	99.26
15	K-II/3	43.14	34.34	6.81	3.88	2.33	3.29	1.39	1.56	1.73	0.86	0.71	0.64	0.16	0.41	0.16	b.d.l.	0.04	0.29	b.d.l.	b.d.l.	100.27
16	K-II/3	43.11	34.01	6.73	4.01	2.01	3.47	1.30	1.35	1.50	1.09	0.61	0.63	0.14	0.35	0.12	b.d.l.	0.06	0.37	b.d.l.	b.d.l.	99.58
17	K-II/3	42.33	33.63	6.61	3.95	1.99	3.43	1.14	1.46	1.63	1.59	0.61	0.70	0.16	0.32	0.13	b.d.l.	0.06	0.55	0.02	0.01	98.92
18	K-II/3	41.76	33.91	7.25	3.76	3.14	3.11	1.28	1.31	1.46	1.01	0.84	0.82	0.26	0.37	0.20	b.d.l.	0.04	0.32	0.02	0.01	99.73
avr. det. lim.		**0.06**	**0.02**	**0.12**	**0.11**	**0.09**	**0.12**	**0.23**	**0.06**	**0.06**	**0.02**	**0.09**	**0.28**	**0.08**	**0.13**	**0.07**	**0.15**	**0.01**	**0.03**	**0.02**	**0.01**	-

	Y_2O_3	P_2O_5	Dy_2O_3	Er_2O_3	Gd_2O_3	Yb_2O_3	Ho_2O_3	FeO	Fe_2O_3	UO_2	Tb_2O_3	Lu_2O_3	Sm_2O_3	Tm_2O_3	Eu_2O_3	Nd_2O_3	PbO	SiO_2	CaO	ThO_2	Total
minimum	36.43	33.31	5.29	2.93	1.03	1.73	1.14	0.70	0.78	0.43	0.34	0.48	b.d.l.	0.25	0.12	b.d.l.	0.02	0.24	b.d.l.	b.d.l.	96.97
maximum	45.51	35.15	9.90	4.41	6.28	3.51	1.43	1.72	1.91	2.12	1.34	0.82	1.48	0.45	0.83	0.63	0.10	0.68	0.04	0.02	101.14
arithmetic mean	41.15	34.40	7.17	3.82	3.20	3.11	1.30	1.23	1.37	1.00	0.79	0.67	0.46	0.32	0.32	0.14	0.05	0.37	0.02	0.01	99.70
median	41.74	34.39	7.01	3.89	2.50	3.28	1.32	1.25	1.39	0.88	0.72	0.68	0.19	0.31	0.19	0.08	0.04	0.32	0.02	0.01	99.66
standard deviation	2.46	0.50	1.07	0.38	1.62	0.51	0.08	0.25	0.28	0.44	0.26	0.09	0.43	0.06	0.24	0.16	0.02	0.13	0.01	0.01	0.87

F – Atoms per formula unit (apfu) calculations in xenotime-(Y). [the formulae were calculated to 4 oxygen and 2 cations]

WDS point	1	2	3	4	5	6	7	8	9	10	11	12	13	14	15	16	17	18
Sample Point	K-II/3	K-II/3	K-II/3	K-II/3	K-II/3	K-II/3	K-II/3	K-II/3	K-II/3	K-II/3	K-II/3	K-II/3	K-II/3	K-II/3	K-II/3	K-II/3	K-II/3	K-II/3
Y	0.81	0.79	0.66	0.67	0.61	0.63	0.73	0.68	0.72	0.73	0.74	0.75	0.73	0.68	0.76	0.75	0.73	0.72
P	0.99	0.98	0.98	0.99	0.99	0.99	0.99	0.99	0.98	1.00	0.99	0.99	0.99	0.99	0.98	0.98	0.97	0.98
Dy	0.06	0.06	0.11	0.11	0.09	0.09	0.08	0.08	0.07	0.08	0.08	0.07	0.08	0.07	0.07	0.07	0.07	0.08
Er	0.04	0.04	0.03	0.03	0.04	0.04	0.04	0.04	0.04	0.04	0.04	0.04	0.04	0.05	0.04	0.04	0.04	0.04
Gd	0.01	0.01	0.07	0.06	0.06	0.07	0.03	0.06	0.03	0.03	0.03	0.02	0.03	0.04	0.03	0.02	0.02	0.04
Yb	0.03	0.04	0.02	0.02	0.03	0.03	0.04	0.03	0.03	0.03	0.04	0.04	0.03	0.03	0.03	0.04	0.04	0.03
Ho	0.01	0.01	0.02	0.01	0.01	0.01	0.01	0.01	0.01	0.01	0.01	0.01	0.01	0.01	0.01	0.01	0.01	0.01
Fe^{3+}	0.02	0.02	0.03	0.03	0.04	0.04	0.03	0.04	0.03	0.04	0.03	0.03	0.04	0.05	0.04	0.04	0.04	0.04
U	0.01	0.03	0.01	0.01	0.02	0.01	0.01	0.01	0.03	0.01	0.01	0.02	0.02	0.01	0.01	0.02	0.02	0.02
Tb	0.00	0.00	0.01	0.01	0.01	0.01	0.01	0.01	0.01	0.01	0.01	0.01	0.01	0.01	0.01	0.01	0.01	0.01
Lu	0.00	0.01	0.01	0.01	0.01	0.01	0.01	0.01	0.01	0.01	0.01	0.01	0.01	0.01	0.01	0.01	0.01	0.01
Sm	0.00	0.00	0.01	0.01	0.01	0.02	0.00	0.01	0.00	0.00	0.00	0.00	0.00	0.01	0.00	0.00	0.00	0.00
Tm	0.00	0.00	0.00	0.00	0.00	0.00	0.00	0.00	0.00	0.00	0.00	0.00	0.00	0.00	0.00	0.00	0.00	0.00
Eu	0.00	0.00	0.01	0.01	0.01	0.01	0.00	0.00	0.00	0.00	0.00	0.00	0.00	0.01	0.00	0.00	0.00	0.00
Nd	0.00	0.00	0.00	0.01	0.00	0.00	0.00	0.00	0.00	0.00	0.00	0.00	0.00	0.00	0.00	0.00	0.00	0.00
Pb	0.00	0.00	0.00	0.00	0.00	0.00	0.00	0.00	0.00	0.00	0.00	0.00	0.00	0.00	0.00	0.00	0.00	0.00
Si	0.01	0.02	0.01	0.01	0.01	0.01	0.01	0.01	0.02	0.01	0.01	0.01	0.01	0.01	0.01	0.01	0.02	0.01
Ca	0.00	0.00	0.00	0.00	0.00	0.00	0.00	0.00	0.00	0.00	0.00	0.00	0.00	0.00	0.00	0.00	0.00	0.00
Th	0.00	0.00	0.00	0.00	0.00	0.00	0.00	0.00	0.00	0.00	0.00	0.00	0.00	0.00	0.00	0.00	0.00	0.00
Total	2.02	2.02	1.99	1.99	1.95	1.97	2.01	1.99	2.00	2.00	2.00	2.01	2.00	1.99	2.01	2.00	2.00	2.00
REE	0.18	0.18	0.29	0.29	0.28	0.29	0.23	0.26	0.21	0.22	0.22	0.21	0.21	0.25	0.21	0.21	0.21	0.23

G – Full REE fluorocarbonates WDS results. [wt.%; b.d.l. – below detection limit]

WDS point	Sample point	Ce_2O_3	La_2O_3	CaO	F	Nd_2O_3	Pr_2O_3	Y_2O_3	ThO_2	Gd_2O_3	Sm_2O_3	FeO	Fe_2O_3	SiO_2	Al_2O_3	Dy_2O_3	SO_3	P_2O_5	K_2O	SrO	Na_2O	MgO	Total
1	C-X/46	27.70	14.47	7.00	7.68	10.89	2.94	3.10	-	2.23	1.97	0.87	0.97	0.29	0.38	0.76	1.30	0.20	0.06	0.31	0.10	b.d.l.	82.35
2	C-X/46	27.84	14.50	7.23	8.00	10.61	3.00	3.09	-	1.91	1.97	1.10	1.22	0.49	0.31	0.75	1.31	0.18	0.08	0.35	0.11	b.d.l.	82.91
3	C-X/46	26.27	12.97	5.95	7.65	9.36	2.66	2.39	-	1.48	1.63	3.62	4.02	1.86	1.66	0.47	2.06	0.16	0.21	0.38	0.19	0.13	81.29
4	C-X/46	27.88	14.17	6.49	6.24	11.51	3.19	2.53	-	4.67	2.01	1.05	1.17	1.09	0.11	0.48	1.32	0.13	b.d.l.	0.20	b.d.l.	b.d.l.	83.14

5	C-X/46	25.67	12.24	7.58	6.26	9.61	2.69	2.28	-	1.62	1.87	4.04	4.49	2.08	1.96	0.50	1.10	0.12	0.08	0.23	b.d.l.	0.49	80.44
6	C-X/46	21.29	10.48	8.76	5.03	8.14	2.28	1.99	-	0.93	1.41	5.68	6.31	6.66	4.69	0.45	0.89	0.15	0.07	0.22	b.d.l.	0.92	80.24
7	C-X/46	28.30	13.50	6.53	6.01	11.24	2.98	3.03	-	4.45	1.98	0.50	0.56	0.41	b.d.l.	0.54	1.35	0.10	b.d.l.	0.28	b.d.l.	b.d.l.	81.35
8	C-X/46	27.17	14.05	7.02	8.13	10.03	3.00	3.65	-	1.93	1.83	1.28	1.42	0.56	0.35	0.82	0.96	0.14	0.04	0.26	b.d.l.	0.08	81.36
9	C-X/46	27.31	13.84	6.64	5.82	10.10	2.93	4.13	-	1.73	1.94	1.81	2.01	0.79	0.59	0.78	1.23	0.14	0.04	0.26	b.d.l.	0.06	80.23
10	C-X/46	22.37	11.55	7.35	7.39	8.45	2.50	2.99	-	1.64	1.67	5.96	6.63	5.94	3.81	0.64	1.18	0.14	0.04	0.29	0.11	0.47	84.53
11	G-I/13	25.82	13.06	7.31	5.36	10.14	2.79	4.66	3.92	1.59	1.65	b.d.l.	b.d.l.	2.76	0.93	0.61	0.39	0.11	0.06	0.24	0.34	b.d.l.	81.96
12	G-I/13	27.63	13.59	7.15	6.55	10.56	2.85	3.93	5.03	1.38	1.66	0.14	0.15	10.85	3.95	0.64	0.74	0.14	0.10	0.23	1.09	b.d.l.	98.30
13	G-I/13	29.32	15.14	6.22	6.06	13.50	3.36	2.13	2.29	2.01	2.19	0.53	0.59	0.11	0.08	0.21	0.58	b.d.l.	0.08	0.17	b.d.l.	b.d.l.	84.26
14	G-I/13	28.80	16.04	5.46	5.57	12.56	3.28	2.26	3.21	2.13	2.04	0.21	0.23	0.16	0.08	0.26	0.51	0.12	0.15	0.20	b.d.l.	b.d.l.	83.22
15	K-II/3	26.64	19.57	4.08	6.87	13.04	2.80	1.05	1.31	1.82	1.93	0.36	0.40	0.33	0.15	b.d.l.	0.37	b.d.l.	0.14	0.19	b.d.l.	b.d.l.	80.83
16	K-II/3	30.83	15.85	4.76	6.78	14.06	3.27	2.06	1.71	2.33	2.50	0.47	0.52	0.35	b.d.l.	b.d.l.	0.45	b.d.l.	0.09	0.23	b.d.l.	b.d.l.	86.04
17	K-II/3	30.36	15.37	4.74	6.99	13.75	3.37	2.53	2.37	2.28	2.39	0.31	0.35	0.22	b.d.l.	0.29	0.60	0.12	0.09	0.16	b.d.l.	b.d.l.	86.17
18	K-II/3	29.94	17.32	4.21	7.45	14.00	3.30	1.59	1.87	1.88	2.20	0.50	0.55	0.31	0.12	b.d.l.	0.57	b.d.l.	0.10	0.16	b.d.l.	b.d.l.	85.64
19	K-II/3	28.62	14.20	5.03	6.62	13.48	3.16	2.73	1.85	2.14	2.33	0.29	0.32	0.67	0.09	b.d.l.	0.57	0.10	0.08	0.19	b.d.l.	b.d.l.	82.59
20	K-II/3	28.00	14.75	3.79	7.53	12.24	3.16	1.67	2.07	1.56	1.91	0.50	0.56	5.17	2.95	b.d.l.	0.55	0.06	0.21	0.15	b.d.l.	0.11	86.69
21	K-II/3	29.63	20.54	5.72	4.51	15.17	3.29	0.68	0.17	1.49	1.74	0.26	0.29	1.93	0.08	b.d.l.	0.06	b.d.l.	0.08	b.d.l.	b.d.l.	b.d.l.	85.66
22	K-II/3	23.33	11.09	5.96	9.13	9.90	2.54	2.32	3.20	4.06	1.65	2.76	3.07	2.03	0.94	0.39	0.49	0.13	0.30	0.19	0.05	0.15	80.85
23	K-II/3	30.21	15.26	4.56	5.87	13.64	3.33	2.35	1.08	2.15	2.31	0.22	0.24	0.39	0.16	0.24	0.93	b.d.l.	0.11	0.16	b.d.l.	b.d.l.	83.08
24	K-II/3	30.45	14.69	5.03	7.66	13.10	3.60	2.45	1.94	2.27	2.37	0.22	0.24	0.12	0.08	0.33	1.49	0.10	0.16	0.16	b.d.l.	b.d.l.	86.39
25	K-II/3	29.66	16.04	5.28	7.68	12.29	3.30	2.39	1.50	2.03	2.03	0.28	0.31	0.25	0.12	0.35	1.50	b.d.l.	0.15	0.18	b.d.l.	b.d.l.	85.21
26	K-II/3	26.73	12.00	7.62	6.38	11.54	3.10	3.35	-	2.89	2.80	0.85	0.95	0.36	0.11	1.00	0.91	0.21	b.d.l.	b.d.l.	b.d.l.	b.d.l.	80.00
27	G-III/17	26.76	13.78	5.57	6.44	10.79	2.80	3.25	2.38	1.88	1.70	1.16	1.29	2.59	1.57	0.73	1.18	0.08	0.19	0.15	0.16	0.03	83.60
28	G-III/17	26.51	14.20	8.28	7.97	11.30	2.82	3.58	3.28	2.04	1.89	1.42	1.57	2.33	1.77	0.79	0.26	0.08	0.08	0.13	b.d.l.	0.06	89.02
29	G-III/17	22.01	11.25	8.99	5.10	9.50	2.61	3.34	2.04	1.70	1.46	1.87	2.07	7.19	4.94	0.64	0.38	b.d.l.	0.15	0.20	0.14	0.05	84.33
30	G-I/13	24.23	12.27	9.39	7.13	10.46	2.65	3.66	2.79	4.32	1.96	0.96	1.06	1.16	0.70	0.74	0.40	0.06	0.13	0.16	b.d.l.	b.d.l.	83.43
31	G-I/13	26.78	13.80	9.56	9.32	12.50	3.00	4.18	2.89	2.41	2.16	1.45	1.61	0.93	0.44	0.94	0.26	0.06	0.12	0.17	b.d.l.	0.03	91.22
32	G-I/13	27.18	13.37	10.97	8.79	11.88	2.85	3.30	3.17	2.17	2.00	0.98	1.09	1.78	0.82	0.88	0.45	b.d.l.	0.12	0.15	0.07	0.11	91.26
avr. det. lim.		**0.23**	**0.24**	**0.03**	**0.09**	**0.38**	**0.28**	**0.11**	**0.07**	**0.11**	**0.29**	**0.12**	**0.14**	**0.07**	**0.06**	**0.19**	**0.06**	**0.06**	**0.03**	**0.11**	**0.04**	**0.03**	-

	Ce_2O_3	La_2O_3	CaO	F	Nd_2O_3	Pr_2O_3	Y_2O_3	ThO_2	Gd_2O_3	Sm_2O_3	FeO	Fe_2O_3	SiO_2	Al_2O_3	Dy_2O_3	SO_3	P_2O_5	K_2O	SrO	Na_2O	MgO	TiO_2	Total
minimum	21.29	10.48	3.79	4.51	8.14	2.28	0.68	0.17	0.93	1.41	0.03	0.03	0.11	0.03	0.00	0.06	0.02	0.02	0.06	0.00	0.00	0.00	71.79
maximum	30.83	20.54	10.97	9.32	15.17	3.60	4.66	5.03	4.67	2.80	5.96	6.63	10.85	4.94	1.00	2.06	0.21	0.30	0.38	1.09	0.92	0.27	86.65
arithmetic mean	27.23	14.22	6.57	6.87	11.54	2.98	2.77	2.38	2.22	1.97	1.30	1.45	1.94	1.06	0.49	0.82	0.10	0.10	0.20	0.08	0.08	0.06	77.16
median	27.47	14.11	6.51	6.82	11.41	2.99	2.63	2.29	2.02	1.96	0.86	0.96	0.86	0.37	0.49	0.67	0.10	0.09	0.19	0.01	0.00	0.04	77.09
standard deviation	2.44	2.16	1.72	1.16	1.74	0.30	0.89	1.04	0.89	0.30	1.50	1.67	2.50	1.43	0.28	0.46	0.05	0.06	0.07	0.20	0.19	0.07	3.17

H – Full plumbogummite WDS results. [wt.%; b.d.l. – below detection limit]

WDS point	Sample point	PbO	Al_2O_3	P_2O_5	FeO	Fe_2O_3	SiO_2	Ce_2O_3	CaO	La_2O_3	Nd_2O_3	ThO_2	SO_3	Y_2O_3	SrO	Dy_2O_3	K_2O	Pr_2O_3	Total
1	St. Johannes mine	32.36	26.00	22.02	3.66	4.06	5.18	1.85	2.15	1.02	0.72	0.41	0.44	0.13	0.17	0.12	0.05	b.d.l.	96.75
2	St. Johannes mine	29.39	25.83	19.99	3.27	3.63	7.85	3.01	2.70	1.67	1.16	0.24	0.58	0.14	0.16	b.d.l.	0.07	0.26	96.76
avr. det. lim.		-	**0.05**	**0.02**	**0.02**	**0.05**	**0.02**	**0.13**	**0.02**	**0.14**	**0.20**	**0.07**	**0.03**	**0.04**	**0.04**	**0.10**	**0.02**	**0.19**	-
	minimum	29.39	25.83	19.99	3.27	3.63	5.18	1.85	2.15	1.02	0.72	0.24	0.44	0.13	0.16	0.08	0.05	0.07	96.75
	maximum	32.36	26.00	22.02	3.66	4.06	7.85	3.01	2.70	1.67	1.16	0.41	0.58	0.14	0.17	0.12	0.07	0.26	96.76
	arithmetic mean	30.87	25.92	21.00	3.46	3.85	6.51	2.43	2.43	1.34	0.94	0.32	0.51	0.14	0.16	0.10	0.06	0.17	96.75

I – ICP-MS results of the whole-rock samples

Area	Sample	Depth	ICP-MS (ppm)																Total REE	Fig.14 lines
			Sc	Y	La	Ce	Pr	Nd	Eu	Sm	Gd	Tb	Dy	Ho	Er	Tm	Yb	Lu		
Gierczyn	G-I/13/01	146.80-146.89	17.90	42.40	18.50	43.90	6.00	26.90	2.37	7.23	8.73	1.39	8.18	1.61	4.24	0.50	2.84	0.39	193.08	
	G-I/13/02	154.07-154.15	9.00	12.60	17.30	38.80	4.90	19.20	1.10	4.15	3.74	0.58	3.40	0.63	1.81	0.25	1.58	0.22	119.26	
	G-I/13/03	154.15-154.25	10.10	16.70	25.80	52.20	6.20	23.60	1.09	4.65	3.99	0.60	3.52	0.67	1.88	0.26	1.64	0.24	153.14	
	G-I/13/04	154.25-154.50	10.10	11.80	14.40	33.40	4.40	17.20	0.95	3.75	3.26	0.50	3.01	0.61	1.86	0.26	1.74	0.25	107.49	
	G-I/13/05	154.50-154.71	9.90	21.00	25.50	54.70	6.60	24.80	1.36	5.05	4.79	0.73	4.41	0.86	2.44	0.35	2.26	0.33	165.08	
	G-I/13/06	154.85-154.90	10.40	23.70	33.00	66.70	7.90	29.40	1.44	5.85	5.29	0.80	4.70	0.88	2.37	0.31	1.90	0.26	194.90	
	G-I/13/07	155.64-155.74	10.00	11.80	14.10	32.70	4.30	16.70	0.94	3.54	3.13	0.48	2.93	0.60	1.77	0.26	1.73	0.24	105.22	
	G-I/13/08	158.75-158.88	9.70	16.10	14.10	32.70	4.30	16.80	1.02	3.69	3.51	0.59	3.80	0.79	2.30	0.34	2.22	0.32	112.28	

	G-I/13/09	158.88-159.00	15.90	25.50	43.30	86.90	10.10	37.50	1.81	7.25	6.31	0.94	5.52	1.02	2.72	0.35	2.11	0.29	247.52	
	G-I/13/10	166.00-166.09	11.30	20.20	25.60	54.60	6.60	25.30	1.45	5.17	4.80	0.72	4.40	0.85	2.36	0.32	1.86	0.25	165.78	
	G-I/13/11	166.35-166.50	9.20	18.10	25.00	54.00	6.80	26.20	1.51	5.28	4.74	0.72	4.40	0.86	2.36	0.31	1.78	0.23	161.49	
	G-I/13/12	168.25-168.42	12.40	36.60	31.10	68.30	8.70	34.30	2.40	8.33	10.52	1.83	11.04	1.99	5.01	0.61	3.50	0.43	237.06	
	G-I/13/13	175.35-175.41	19.90	30.50	52.50	105.80	12.30	45.10	2.09	8.27	7.03	1.03	6.31	1.22	3.42	0.46	2.87	0.38	299.18	
	G-I/13/14	175.48-175.61	17.20	33.20	30.60	67.00	8.50	33.10	1.76	7.07	6.71	1.03	6.45	1.31	3.69	0.48	2.82	0.35	221.27	
	G-I/13/15	183.16-183.33	16.60	31.60	42.40	85.00	10.10	37.10	1.75	7.08	6.30	1.02	6.52	1.29	3.49	0.44	2.62	0.35	253.66	
	G-I/13/16	183.43-183.52	6.00	7.10	7.40	17.90	2.50	10.70	0.76	2.68	2.57	0.41	2.43	0.46	1.28	0.18	1.22	0.18	63.77	
	G-I/13/17	191.70-191.83	10.50	14.80	18.30	42.20	5.70	22.40	1.11	4.85	4.34	0.65	4.00	0.80	2.24	0.30	1.97	0.28	134.44	
	G-I/13/18	204.65-204.76	18.40	28.80	49.30	100.50	12.10	44.50	1.88	8.17	7.02	1.03	5.92	1.15	3.20	0.43	2.68	0.37	285.45	
	G-I/13/19	207.55-207.69	17.40	23.50	41.40	85.50	10.20	37.90	1.99	7.19	6.39	0.93	5.27	0.99	2.64	0.34	1.89	0.25	243.78	
	G-III/17	397.70-397.77	5.10	8.90	20.10	39.70	4.60	17.70	0.99	3.68	2.77	0.39	2.21	0.37	0.94	0.14	0.84	0.11	108.54	
	G-VI/22	255.40-255.48	6.00	15.80	18.70	37.50	4.20	15.50	0.68	3.07	2.99	0.47	2.99	0.58	1.71	0.24	1.50	0.21	112.14	
	G-VI/29/1	52.00-52.07	8.30	55.40	13.10	27.10	3.10	11.50	1.30	2.62	3.89	0.88	7.17	1.66	5.16	0.81	5.72	0.84	148.55	
	G-VI/29/2	52.10-52.14	7.20	20.60	20.70	44.00	5.10	19.30	1.70	4.38	5.34	0.77	4.24	0.76	2.05	0.27	1.68	0.24	138.33	
	G-VI/29/3	52.50-52.55	50.00	21.30	2.20	5.30	0.70	3.90	1.28	2.70	3.95	0.79	5.21	0.96	2.83	0.52	4.00	0.57	106.21	
	G-VI/29/4	52.80-52.87	9.90	49.20	26.00	52.70	6.30	24.30	2.96	6.60	9.40	1.72	10.75	2.07	5.70	0.82	5.26	0.68	214.36	
Krobica	K-II/3/01	203.95-204.05	15.20	25.10	38.80	83.00	9.80	36.60	1.54	6.91	5.91	0.86	5.01	0.99	2.90	0.43	3.11	0.50	236.66	
	K-II/3/02	245.70-245.74	18.30	29.60	51.50	104.10	12.40	45.90	1.91	8.56	7.25	1.05	6.11	1.20	3.24	0.41	2.41	0.34	294.28	
	K-II/3/03	270.90-270.97	16.10	31.80	43.10	88.60	10.40	38.80	2.06	7.37	6.66	1.03	6.33	1.27	3.66	0.49	3.11	0.43	261.21	
	K-II/3/04	275.60-275.69	10.90	19.70	32.00	61.50	7.10	26.00	1.83	5.33	4.75	0.73	4.30	0.81	2.17	0.29	1.73	0.24	179.38	
	K-II/3/05	314.60-314.66	14.10	28.00	42.00	84.30	9.90	37.10	2.08	7.55	6.59	0.98	5.67	1.11	3.13	0.45	2.78	0.39	246.13	
	K-II/3/06	315.70-315.80	10.10	24.00	21.90	50.60	6.40	25.30	1.55	5.54	5.30	0.83	5.28	1.13	3.33	0.47	2.93	0.41	165.07	
	K-II/3/07	251.2	3.80	21.50	11.50	27.20	3.80	17.70	1.83	6.75	7.14	1.13	5.96	1.00	2.54	0.33	2.10	0.29	114.57	
	K-II/3/08	250.6	5.90	15.60	2.80	6.10	0.80	3.50	0.89	1.62	2.95	0.56	3.41	0.63	1.69	0.23	1.49	0.21	48.38	
	K-III/6/01	326.20-326.25	15.80	30.70	42.70	85.80	9.90	37.20	2.89	7.06	6.61	1.02	6.20	1.17	3.14	0.45	2.75	0.39	253.78	
	K-III/6/02	327.30-327.33	12.70	95.60	31.60	65.20	7.90	31.60	5.05	9.68	15.36	3.00	19.76	3.73	10.11	1.48	9.37	1.21	323.35	
	K-III/6/03	327.60-327.64	15.60	38.40	56.80	114.20	13.20	49.70	4.62	9.84	8.64	1.29	7.76	1.48	4.03	0.54	3.22	0.43	329.75	
	Orłowice quarry	-	17.70	42.00	20.50	43.70	5.10	19.00	1.15	3.91	4.86	1.04	7.16	1.42	3.97	0.56	3.69	0.53	176.29	
	St. Leopold/7	-	14.60	28.30	27.40	55.70	6.80	25.50	1.69	5.21	4.92	0.86	5.55	1.14	3.17	0.44	2.73	0.39	184.40	

	St. Leopold/7B	-	11.50	17.60	30.00	61.60	7.60	28.40	1.71	5.59	4.81	0.73	3.97	0.75	1.97	0.26	1.53	0.21	178.23	
	St. Leopold/10	-	15.30	37.00	25.00	51.90	6.00	22.10	1.28	4.38	5.27	1.07	7.12	1.46	3.95	0.53	3.18	0.44	185.98	
	St. Leopold/17	-	13.40	20.80	51.90	97.50	12.20	46.00	3.05	9.10	7.57	1.00	5.06	0.90	2.39	0.32	1.96	0.28	273.43	
	St. Leopold/28	-	12.60	19.10	23.20	51.40	6.10	23.80	1.43	4.71	4.17	0.61	3.72	0.81	2.37	0.33	2.04	0.28	156.67	
	St. Leopold/44A	-	14.40	26.20	24.80	54.20	6.40	23.50	1.26	4.48	4.49	0.85	5.51	1.11	3.04	0.40	2.46	0.34	173.44	
	St. Leopold/44B	-	9.00	17.20	19.80	40.30	4.70	17.50	0.96	3.35	3.06	0.49	3.19	0.68	2.08	0.30	1.78	0.23	124.62	
	St. Johaness/19	-	<0.5	4.80	2.80	8.20	1.20	5.50	0.22	1.23	1.04	0.17	1.17	0.27	0.83	0.12	0.71	0.10	28.36	
	St. Johaness/20	-	<0.5	19.40	15.70	18.80	1.80	6.60	0.17	0.90	1.49	0.18	1.15	0.31	0.91	0.11	0.50	0.09	68.11	
	St. Johaness/34	-	12.60	31.80	29.40	59.70	7.00	26.00	1.63	5.26	5.27	0.89	5.94	1.22	3.56	0.49	3.17	0.46	194.39	
	St. Johaness/35	-	<0.5	1.40	1.20	1.90	<0.5	0.80	<0.05	0.16	0.18	<0.05	0.15	<0.05	0.09	<0.05	0.06	<0.05	5.94	Not on the graphs
	St. Johaness/49	-	10.90	21.00	23.30	49.50	5.80	21.50	1.21	4.30	3.82	0.59	3.85	0.83	2.52	0.36	2.35	0.33	152.16	
	St. Johaness/54	-	9.60	30.50	23.90	49.50	6.00	22.60	1.38	5.07	4.97	0.86	5.73	1.17	3.37	0.46	2.87	0.38	168.36	
Czerniawa-Zdrój	C-IV/16	211.10-211.14	13.50	26.50	40.70	80.70	9.50	36.30	2.61	7.48	6.07	0.90	5.29	1.04	2.92	0.42	2.56	0.37	236.86	
	C-VI/26/1	249.40-249.45	13.10	31.80	42.10	83.30	9.90	37.10	3.42	7.56	6.61	1.04	6.44	1.26	3.43	0.46	2.71	0.38	250.61	
	C-VI/26/2	249.50-249.58	11.00	27.00	34.10	66.90	8.00	30.20	4.66	7.06	7.08	1.12	6.38	1.13	2.95	0.38	2.31	0.33	210.60	
	C-IX/41/1	201.80-201.82	9.10	6.40	12.80	25.40	2.90	11.30	0.61	2.41	2.07	0.29	1.57	0.29	0.81	0.12	0.82	0.12	77.01	
	C-IX/41/2	202.20-202.25	6.40	3.60	8.50	16.80	1.90	7.70	0.48	1.57	1.29	0.18	0.90	0.16	0.42	0.06	0.43	0.06	50.45	
	C-XI/51	51.70-51.77	11.20	7.40	33.60	67.00	7.90	30.10	1.81	5.70	4.09	0.45	1.98	0.32	0.91	0.13	0.85	0.13	173.57	
	C-X/46/1	223.50-223.60	8.80	18.10	31.30	63.00	7.20	26.30	1.87	5.25	4.74	0.69	3.93	0.73	2.00	0.27	1.69	0.23	176.10	
	C-X/46/2	223.50-223.60	18.00	27.10	43.10	86.80	10.10	38.60	1.80	7.52	6.70	0.98	6.20	1.17	3.32	0.47	2.98	0.43	255.27	
Przecznica	P-I/4/1	401.26-401.33	11.50	16.60	26.00	53.20	6.00	22.80	1.03	4.20	3.96	0.59	3.42	0.67	2.00	0.28	1.96	0.28	154.49	
	P-I/4/2	401.13-401.21	6.60	9.00	17.60	35.80	4.00	15.00	0.67	2.90	2.63	0.37	1.92	0.36	1.07	0.16	1.04	0.14	99.26	
	P-III/15/1	373.65-373.75	16.20	15.70	41.80	88.00	9.90	37.60	1.60	7.56	6.37	0.84	4.32	0.70	1.76	0.22	1.40	0.20	234.17	
	P-III/15/2	272.07-272.18	18.30	34.60	42.80	87.80	10.20	39.30	1.96	7.81	7.11	1.09	6.70	1.34	3.88	0.54	3.29	0.48	267.20	
	P-III/15/3	313.22-313.31	19.40	34.40	52.10	107.30	12.40	45.20	1.84	8.95	8.19	1.22	7.05	1.40	4.20	0.54	3.35	0.49	308.03	
	P-III/15/4	310.14-310.23	44.20	26.20	24.10	55.40	7.20	32.10	1.71	7.79	7.96	1.16	6.43	1.11	2.76	0.31	1.66	0.20	220.29	

APPENDIX 2

Analytical conditions of EPMA measurements

Element	Signal	WDS crystal	Standard	Peak and background time (s)
Si	Kα	TAP	Wollastonite	20 / 10
Hf	Mα	TAP	47-ZrO_2 Zirconia	20 / 10
Al	Kα	TAP	Orthoclase	20 / 10
Y	Lα	LPET	Xenotime	20 / 10
Sr	Lα	LPET	$SrTiO_3$	20 / 10
Lu	Lβ	LLIF	Lu-glass	20 / 10
Tm	Lβ	LLIF	Tm-glass	20 / 10
Ho	Lβ	LLIF	$HoPO_4$	20 / 10
Yb	Lα	LLIF	$YbPO_4$	20 / 10
Er	Lα	LLIF	$ErPO_4$	20 / 10
Dy	Lα	LLIF	$DyPO_4$	20 / 10
Fe	Kα	LLIF	34-Olivine	20 / 10
Tb	Lα	LLIF	Tb_Glass	20 / 10
Gd	Lα	LLIF	$GdPO_4$	20 / 10
Eu	Lα	LLIF	$EuPO_4$	20 / 10
Sm	Lα	LLIF	$SmPO_4$	20 / 10
As	Lβ	TAP	Arsenopyrite	20 / 10
Nd	Lβ	LLIF	$NdPO_4$	20 / 10
P	Kα	LPET	Apatite	20 / 10
Zr	Lα	LPET	$ZrSiO_4$	20 / 10
S	Kα	LPET	$BaSO_4$	20 / 10
K	Kα	LPET	Orthoclase	20 / 10
Ca	Kα	LPET	Wollastonite	20 / 10
Th	Mα	LPET	Th_Glass	20 / 10
U	Mβ	LPET	U_Glass	20 / 10
Pb	Mβ	LPET	Crocoite	20 / 10

Used standard composition:

- Wollastonite = O: 41.17%, Na: 0.01%, Mg: 0.01%, Si: 23.99%, Ca: 34.17%, Ti: 0.01%, Mn: 0.49%, Fe: 0.15%
- 47-ZrO_2 Zirconia = O: 24.91%, Y: 14.37%, Zr: 59.17%, Hf: 1.51%
- Orthoclase = O: 46.28%, Na: 1.01%, Al: 9.82%, Si: 30.43%, K: 12.19%, Ca: 0.01%, Ti: 0.01%, Mn: 0.01%, Fe: 0.02%, Sr: 0.04%, Ba: 0.13%
- Xenotime = O: 31.7%, Si: 0.04%, P: 15.28%, Y: 33.62%, Nd: 0.14%, Sm: 0.67%, Eu: 0.43%, Gd: 3.8%, Tb: 0.83%, Dy: 6.4%, Er: 3.42%, Yb: 3.42%, Th: 0.14%
- $SrTiO_3$ = Sr: 47.74%, Ti: 26.10%, O: 26.16%
- 23_Lu-glass = O: 42.42%, Al: 6.75%, Si: 25.5%, Ca: 14.78%, Lu: 10.55%
- 21_Tm-glass = O: 42.55%, Al: 6.75%, Si: 25.5%, Ca: 14.78%, Tm: 10.42%
- $HoPO_4$ = Ho: 63.46%, P: 11.91%, O: 24.62%
- $YbPO_4$ = Yb: 64.56%, P: 11.56%, O: 23.88%
- $ErPO_4$ = Er: 63.78%, P: 11.81%, O: 24.41%
- $DyPO_4$ = Dy : 63.11%, P : 12.03%, O: 24.86%
- 34-Olivine = O: 43.89%, Mg: 30.42%, Si: 19.44%, Mn: 0.08%, Fe: 5.87%, Ni: 0.3%
- 17_Tb_Glass = O: 42.85%, Al: 6.75%, Si: 25.5%, Ca: 14.78%, Tb: 10.12%
- $GdPO_4$ = Gd: 62.35%, P: 12.28%, O: 25.37%
- $EuPO_4$ = Eu: 61.54%, P: 12.54%, O: 25.92%
- $SmPO_4$ = Sm: 61.29%, P: 12.62%, O: 26.08%

- Arsenopyrite FeAsS = Fe: 34.44%, As: 44.83%, S: 20.73%
- $NdPO_4$ = Nd: 60.30%, P: 12.95%, O: 26.75%
- 04-Apatite = O: 38.07%, F: 3.77%, P: 18.42%, Ca: 39.74%
- $ZrSiO_4$ (2) = O: 34.75%, Si: 15.24%, Zr: 49.1%, Hf: 0.91%
- $BaSO_4$ = O: 27.42%, S: 13.74%, Ba: 58.84%
- 2_Orthoclase = O: 46.31%, Na: 1.01%, Al: 9.82%, Si: 30.45%, K: 12.2%, Ca: 0.01%, Mn: 0.01%, Fe: 0.02%, Sr: 0.04%, Ba: 0.13%
- 25_Th_Glass_2 = Al: 7.38%, Si: 27.19%, Ca: 15.72%, Th: 5.17%, O: 44.53%
- 26_U_Glass_2 = O: 45.00%, Al: 7.44%, Si: 27.59%, Ca: 16.11%, U: 3.86%
- 28_Crocoite = O: 19.8%, Cr: 16.09%, Pb: 64.11%